Spring 1-1-2017

Direct Numerical Simulation of Complex Turbulence

Alan Sean-Ker Hsieh
University of Colorado at Boulder, alhs6577@colorado.edu

Direct numerical simulation of complex turbulence

by

Alan Hsieh

B.S., University of Southern California, 2011

M.S., University of Colorado-Boulder, 2014

A thesis submitted to the

Faculty of the Graduate School of the

University of Colorado in partial fulfillment

of the requirements for the degree of

Doctor of Philosophy

Ann and H.J. Smead Department of Aerospace Engineering Sciences

2017

This thesis entitled:
Direct numerical simulation of complex turbulence
written by Alan Hsieh
has been approved for the Ann and H.J. Smead Department of Aerospace Engineering Sciences

Sedat Biringen

Professor Mahmoud I. Hussein

Professor John Evans

Professor Alireza Doostan

Professor Harihar Rajaram

Date _____

The final copy of this thesis has been examined by the signatories, and we find that both the content and the form meet acceptable presentation standards of scholarly work in the above mentioned discipline.

Hsieh, Alan (Ph.D, Ann and H.J. Smead Aerospace Engineering Sciences)

Direct numerical simulation of complex turbulence

Thesis directed by Professor Sedat Biringen

Direct numerical simulations (DNS) of spanwise-rotating turbulent channel flow were conducted. The data base obtained from these DNS simulations were used to investigate the turbulence generation cycle for simple and complex turbulence. For turbulent channel flow, three theoretical models concerning the formation and evolution of sublayer streaks, three-dimensional hairpin vortices and propagating plane waves were validated using visualizations from the present DNS data. The principal orthogonal decomposition (POD) method was used to verify the existence of the propagating plane waves; a new extension of the POD method was derived to demonstrate these plane waves in a spatial channel model. The analyses of coherent structures was extended to complex turbulence and used to determine the proper computational box size for a minimal flow unit (MFU) at $Ro_b \leq 0.5$. Proper realization of Taylor-Gortler vortices in the highly turbulent pressure region was demonstrated to be necessary for acceptably accurate MFU turbulence statistics, which required a minimum spanwise domain length $L_z = \pi$. A dependence of MFU accuracy on Reynolds number was also discovered and MFU models required a larger domain to accurately approximate higher-Reynolds number flows.

In addition, the results obtained from the DNS simulations were utilized to evaluate several turbulence closure models for momentum and thermal transport in rotating turbulent channel flow. Four nonlinear eddy viscosity turbulence models were tested and among these, Explicit Algebraic Reynolds Stress Models (EARSM) obtained the Reynolds stress distributions in best agreement with DNS data for rotational flows. The modeled pressure-strain functions of EARSM were shown to have strong influence on the Reynolds stress distributions near the wall. Turbulent heat flux distributions obtained from two explicit algebraic heat flux models consistently displayed increasing disagreement with DNS data with increasing rotation rate. Results were also

obtained regarding flow control of fully-developed spatially-evolving turbulent channel flow using phononic subsurface structures. Fluid-structure interaction (FSI) simulations were conducted by attaching phononic structures to the bottom wall of a turbulent channel flow field and reduction of turbulent kinetic energy was observed for different phononic designs.

Acknowledgements

I would like to first thank my advisor, Professor Sedat Biringen for his support of my graduate studies in the years I have worked with him. His knowledge and experience in fluid mechanics was vital to my research and without his support and guidance, this work would not have been completed. I would also like to thank the great people I have met while in this program both on the academic and social side. Thank you all for making this journey a productive and enjoyable one.

Contents

Chapter

Tables

Table

Figures

Figure

Chapter 1

Introduction and Motivation

1.1 Turbulence Production in Complex Turbulent Flows

The scientific field of turbulence has posed long-standing challenges to researchers due to the inherent chaotic and irregular motions which define turbulent flows. Since turbulent flows, not laminar flows, are predominantly found in nature and with the prevalence of rotation-dependent machinery in engineering, a physical understanding of turbulent flow in these systems is a necessity for engineering and scientific analyses. The present work examines simple channel turbulence as well as complex turbulence, specifically spanwise-rotating turbulent channel flow. In this thesis, simple turbulence is defined as a turbulent flow field with only one mean flow gradient; complex turbulence is defined as a turbulent flow field with more than one mean flow gradient. Detailed focus is placed on the roles and interactions of the coherent structures in the turbulence generation cycle.

The fundamental structures involved in the turbulence sustenance cycle for turbulent channel flow have been well-documented in experimental (Kim, Kline, and Reynolds, 1971) and DNS studies (Kim, Moin, and Moser, 1987). Near the channel walls, interactions between streamwise vortices and streamwise elongated sublayer streaks result in ejections of the latter structures from the near-wall region. The streaks break down into smaller instabilities which are swept back towards the wall and reform into vortices and streaks. This cylical process is referred to as the bursting cycle and the mechanism through which turbulence is sustained (Kim and Spalart, 1987). Despite the lack of a constitutive theoretical model for governing the overall structure of the tur-

bulence sustenance cycle, theoretical models have been proposed for selected components of the cycle. Using direct numerical simulation (DNS), it is instructive to assess the validity of the theoretical model predictions. The present work examines the fundamental structures of turbulence with comparison to the theoretical models proposed by Landahl (1990), Lengani and Simoni (2015) and Sirovich et al. (1991) for the formation and evolution of such structures with the DNS data base.

The models proposed by Landahl (1990) and Lengani and Simoni (2015) concern the formation of sublayer streaks and three-dimensional hairpin vortices, respectively; both coherent structures are well-known among turbulence researchers and have been the focus of previous flow control efforts to suppress these structures (Kang and Choi, 2008, Lockerby et al., 2005). The present work provides novel support for both theoretical models using visualizations from the present DNS data to compare with the model predictions. The theoretical model proposed by Sirovich et al. (1991) demonstrated the existence of propagating plane waves and the important contributions of these waves to turbulence production. The model specifically delineated two types of energetic modes in turbulent flows: propagating and non-propagating (kinematically degenerate) modes. The non-propagating modes possessed streamwise homogeneity and correspond to the sublayer streaks and vortices discussed in the first two theoretical models (Handler et al., 1993). The experimental studies by Wallace et al. (1977) and Blackwelder and Kaplan (1976), which analyzed the wall structure of turbulent flows, demonstrated the consistent lack of separation between these structures in the streamwise direction hence lending their energy to the zeroeth streamwise mode ($k_1 = 0$).

Propagating modes, despite possessing significantly less energy content than non-propagating modes, were demonstrated by Sirovich et al. (1991) to be necessary for turbulence production using a periodic channel model. The flow control studies by Murakami et al. (1992) and Handler et al. (1993) additionally affirmed the proposal by demonstrating that the phase randomization of a small subset of propagating modes, primarily within the energy-containing scales, reduced turbulent kinetic energy and drag by significant amounts. There were also concerns by Sirovich et al.

(1990) about the possibility of insufficient mesh resolution in the periodic channel model which would result in misplacement of the considerable energy in the slightly-off streamwise modes and incorrect data regarding the energy content of the propagating waves. The present work aims to substantiate the conclusions of Sirovich et al. (1991) for the periodic channel model and additionally affirm the existence of these propagating waves in a spatial channel model for application to future parametric studies for flow control (Kucala, 2015). Analysis of the propagating plane waves required the method of principal orthogonal decomposition (POD) which was uniquely tuned for application to the spatial model.

When turbulent channel flow is subject to rotation in the spanwise direction, asymmetry is observed across the channel distinguished by reduced turbulence levels near one wall and elevated turbulence levels near the opposite wall; these regions are known as the suction and pressure sides, respectively (Grundestam, Wallin, and Johansson, 2008). In addition, rotation-induced body forces (Coriolis, centrifugal) generate a secondary cross flow and consequently a particular type of complex turbulent flow regime is developed with more than one mean flow gradient. The analyses of such complexities on the structure and parameterization of turbulence have relevance to engineering applications such as gas turbine blade and rotating turbomachinery design especially with regards to surface heat transfer and skin friction within the internal cooling passages (Acharya, Sethuraman, and Nikotopoulos, 2012). The effects of rotation on channel turbulence are comprehensively investigated including general turbulence statistics, higher-order statistics, energy budgets and coherent structures. For spanwise-rotating turbulent channel flow, the streaky and vortical structures associated with the turbulence sustenance cycle (Kim et al., 1987, Landahl, 1990) persist in the pressure region and the generation of additional turbulence structures was observed in the rotational turbulence studies of Kristofferson and Andersson (1993) and Grundestam et al. (2008). In order to determine the dimensions of a minimal flow unit, it is imperative to examine the contributions of these rotation-induced structures to turbulence. Quadrant analysis is also used to elucidate a shift in phase relationship between streamwise and wall-normal fluctuating velocity in the suction region.

The analysis of coherent structures for rotational turbulence is also applied to the design of a minimal flow unit (MFU) model at $Ro_b \leq 0.5$. The concept of the minimal flow unit (MFU) model is based on the determination of the smallest computational box size that will produce acceptably accurate turbulence statistics at minimal computational cost. In the study by Jimenez and Moin (1991), a proposed MFU model produced low-order turbulence statistics in good agreement with experimental data in the near-wall region for non-rotating turbulent channel flow. As the dependence of turbulence production on the interactions of various turbulence structures has been well documented in literature (Landahl, 1990, Schoppa and Hussein, 2002), MFU design distinguishes a basic set of structures necessary to sustain turbulence and constructs a shorter domain based on this array of structures. A model's success is determined by its ability to accurately predict essential turbulence statistical quantities at a significantly reduced computational cost compared to full direct numerical simulation (DNS) on a well-resolved computational domain. The MFU models analyzed in the present work reduced the grid number of the full simulations between one and two orders of magnitude, corresponding to an equivalent decrease in computational cost. Such MFU models are necessary for computational fluid dynamics research requiring large amounts of simulations such as parametric studies for flow control (Hussein, Biringen, Bilal, and Kucala, 2015, Kucala and Biringen, 2014). In the present work, we utilize our DNS database for turbulent channel flow, subject to varying rotation and Reynolds numbers, to assess the accuracy of the MFU model for predicting low and high-order moments of turbulent fluctuations.

1.2 Turbulence Modeling

Computational modeling of all types of turbulent flows has been essential to the field of engineering since the advent of the computer, allowing for engineering analysis to extend beyond theory and physical experimentation. As computers have increased in complexity and computational power in the recent decades, new computational methods for turbulence modeling have arisen. Direct numerical simulation (DNS) is a computational simulation in which the three-dimensional, time-dependent Navier-Stokes and energy equations are numerically solved along

with the full range of spatial and temporal scales of turbulence, resulting in the most accurate computational solutions. However, direct numerical simulations are frequently cost-prohibitive due to the high computational cost of resolving all scales, especially in cases of complex geometry and flow configurations.

Another form of computational modeling is Reynolds-Averaged Navier-Stokes (RANS) based modeling in which there is no numerical solution of the Navier-Stokes equations such as in DNS. Instead an alternative form of the Navier-Stokes equations known the Reynolds stress equation is derived and partial differential equations of various flow quantities within this equation are solved for (Reynolds, 1976). While RANS-based models are less accurate than DNS, these models also require far less computational power and therefore RANS models, as well as the corresponding turbulent heat flux models for heat transfer, are highly desirable if they can accurately parameterize turbulent and thermal transport. However, the strong influence of rotational forces on the Reynolds stress and turbulent heat flux transport equations impose significant challenges for model development especially at high rotation numbers. In the present work, the DNS data base is employed to assess four RANS models proposed by (a) Reif et al. (1999), (b) Speziale and Gatski (1993), (c) Girimaji (1996) and (d) Grundestam et al. (2005). Two algebraic heat flux models proposed by (e) Younis et al. (2012) and (f) Abe and Suga (2000), are also evaluated. In addition, the pressure-strain functions proposed in Speziale and Gatski (1993) and Girimaji (1996) are investigated for their influence on the modeled Reynolds stress distributions and the pressure-temperature-gradient functions proposed by Younis et al. (2012) and Abe and Suga (2000) are similarly examined.

Two closure models used for predicting high-order moments as a function of lower-order terms are evaluated. Higher-order closure is very relevant to computational modeling as the budget terms of the Reynolds stress and turbulent heat flux equations, such as the pressure-strain and pressure-temperature-gradient correlation terms, are higher-order moments. RANS and turbulent heat flux models require approximation of these terms using lower-order moments and consequently effective general higher-order closures may be applied to improve these models

(Girimaji, 1996). Both higher-order models rely on the empirical coefficients that have been selected to fit experimental observations; new optimal coefficients are recommended for highest compatibility with the DNS results and are evaluated with respect to the empirical coefficients.

1.3 Control of Turbulent Flows

The purpose of coherent structures analyses in turbulent channel flow is for extension towards flow control of turbulence. Drag and energy reduction in turbulent flows remains an important problem. The potential benefits of efficient flow control systems range from saving billions of dollars in fuel costs for land, air and sea vehicles to achieving more economically and environmentally competitive industrial processes involving fluid flows (Gad-el Hak and Tsai, 2006). Flow control in regards to jet turbines has also been a subject of great interest in recent years. Turbulence is an impediment to effective turbine design due to its flow regime consisting of chaotic property changes and instabilities, leading to undesirable results such as higher drag and energy losses (Rizzetta and Visbal, 2006). Flow control focuses on the reduction of these instabilities using active (non-zero energy cost) or passive (zero energy cost) methods.

The present work considers the passive flow control method of compliant surfaces which have long been used to reduce skin friction in the turbulent boundary layer (Bushnell et al., 1977, Kramer, 1957), specifically subsurface phononic crystals. Phononic crystals are materials arranged in an optimal banded lattice structure such that they exhibit desired band gaps, whereby elastic waves are prohibited from propagation within certain frequency ranges (Hussein, Hamza, Hulbert, and Saitou, 2007). Investigations into the application of these periodic systems for control of fluid flows have demonstrated the effectiveness of phononic subsurfaces in significantly reducing the kinetic energy contributions from turbulent instabilities (Hussein et al., 2015). For fully-developed spatially-evolving turbulent channel flow, the large range of frequencies in fully-developed turbulence presents difficult challenges for phononic subsurface design. But by correct material selection and layering, the dispersion characteristics of the periodic material may be tuned such that, when the channel walls are replaced by this material, the high-energy carrying

frequencies present in the turbulent flow field may be reduced. The goal of these flow control efforts is to optimize the reduction of turbulent kinetic energy through the suppression of the coherent structures which govern the near-wall turbulence sustenance cycle such as the propagating plane waves proposed by Sirovich et al. (1991).

1.4 Thesis Outline

This paper is organized as follows: the second section will cover the governing equations, numerical methods and parameters used in the direct numerical simulations. A detailed verification of the present DNS data base is also provided. The third section will first provide an overview of turbulence dynamics in a plane channel with respect to the validation of three theoretical models for the turbulence generation cycle. This will be followed by an in-depth analysis of the rotational effects on turbulence including the design of a minimal flow unit for spanwise-rotating turbulent channel flow and demonstration of a phase shift in the re-laminarized suction region. The fourth section will consider four RANS-based turbulence models and two turbulent heat flux models with comparison to the DNS results for the modeled Reynolds stress and turbulent heat flux distributions. The accuracy of the modeled pressure-strain and pressure-temperature-gradient functions in the RANS and turbulent heat flux models, respectively, are assessed for correlation to overall model accuracy. Also, two generalized higher-order closures are examined and optimal coefficients are suggested. In the fifth section, an overview of flow control using phononic subsurface structures and the implementation of these structures within the computational model is provided. Results for flow control of turbulence regarding the reduction of turbulent kinetic energy using phononic structures are also shown.

Chapter 2

Governing Equations and Numerical Methods

2.1 Governing Equations

The time-dependent, three-dimensional incompressible Navier-Stokes and energy equations were numerically integrated in a channel flow using a fractional step method (Waggy et al., 2013, 2014). With all spatial coordinates non-dimensionalized by the channel half-height δ and velocities by the laminar centerline velocity u_c, the Navier-Stokes and energy equations read (in conservative form)

$$\frac{\partial u_i}{\partial x_i} = 0 \tag{2.1}$$

$$\frac{\partial u_i}{\partial t} + \frac{\partial u_i u_j}{\partial x_j} = -\frac{\partial p}{\partial x_i} + \frac{1}{Re_c}\frac{\partial^2 u_i}{\partial x_j \partial x_j} - Ro_c \varepsilon_{ijk}\frac{\Omega_j}{\Omega}u_k \tag{2.2}$$

$$\frac{\partial \theta}{\partial t} + \frac{\partial (\theta u_j)}{\partial x_j} = \frac{1}{Re_c\, Pr}\frac{\partial^2 \theta}{\partial x_i \partial x_j} \tag{2.3}$$

where $Re_c = u_c\delta/\nu$, $Pr = \nu/\kappa$, ν is the kinematic viscosity, κ is the thermal diffusivity and the vector $\mathbf{u} = \langle u, v, w \rangle$ is composed of three velocity components in the x (streamwise), y (wall-normal) and z (spanwise) directions, respectively. The rotation number (or Rossby number) is defined as $Ro_c = 2\Omega\delta/u_c$ where Ω is the spanwise angular rotation vector. p is the non-dimensional effective pressure ($p = p_0 - (1/8)Ro_c^2 r^2$) which combines the static pressure (p_0) and centrifugal force, r represents the nondimensional distance away from the axis of rotation. Also, t is non-dimensional time and θ is non-dimensional temperature ($\theta = [T - T_L]/[T_U - T_L]$) with T_U and T_L representing dimensional temperatures on the upper and lower walls, respectively. Equation 2.2 is uncoupled

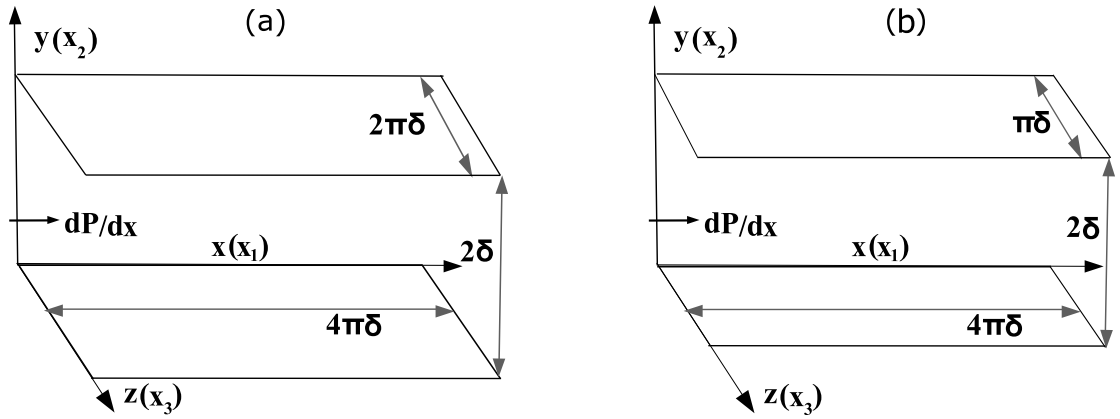

Figure 2.1: Geometry of DNS computational domain for the a) periodic model; b) spatial model

from equation 2.3 and buoyancy effects are neglected. The Prandtl number (Pr) was kept constant at 0.71.

Turbulent channel flow simulations were conducted using both a periodic and spatial model; the flow geometries of the present DNS for the periodic and spatial simulations are shown in figures 3.29(a) and 3.29(b), respectively. No-slip conditions are imposed on the rigid channel walls ($y = 0,2$). An isothermal boundary condition on the dimensionless temperature θ ($\theta_U = 0.5$ and $\theta_L = -0.5$) was imposed at the upper and lower walls. Temperature coupling was initiated once the turbulence field had reached a quasi steady-state solution and a linear distribution for the temperature field was assumed as an initial condition in the wall-normal direction. For the periodic channel in figure 3.29(a), the velocity flow fields are assumed to be statistically homogeneous in the streamwise (x) and spanwise (z) directions allowing periodic boundary conditions in those directions. For the spatial channel in figure 3.29(b), the velocity flow field possesses a periodic boundary condition in only the spanwise direction. No assumptions are made in the streamwise direction hence inflow and outflow boundary conditions are applied. The method developed by Chung and Sung (1997) is used in which crossflow planes from an auxiliary periodic channel flow simulation are used as inflow boundary conditions for the spatial model. The planes are sampled over a sufficient duration and frequency such that both small and large time scales are adequately represented. A spatial channel model is desirable due to a heightened degree of realism over the

periodic model and is used in the present work for verification of the periodic channel results and application for flow control.

2.2 Numerical Methods

All of the numerical methods and schemes presented in this work were performed using a Navier-Stokes solver developed by Waggy (2012) for the simulation of the turbulent Ekman layer. This code was further modified for plane channel flow (Kucala and Biringen, 2014) and periodic channel flow; rotational effects were added and implemented smoothly in the present work. The time integration scheme used is the semi-implicit Adams-Bashforth/Crank-Nicolson (ABCN) method, which makes the numerical procedure second order accurate in time (Waggy et al., 2013). The Crank-Nicholson method uses an implicit scheme for the diffusion terms in equation 2.2, which is written as

$$\frac{\hat{u}_i - u_i^n}{\Delta t} \approx \frac{1}{2\mathrm{Re}}\frac{\partial^2 \hat{u}_i}{\partial x_3^2} + \frac{1}{2\mathrm{Re}}\frac{\partial^2 u_i^n}{\partial x_3^2} + \mathcal{O}\left(\Delta t^2\right) \tag{2.4}$$

where the predicted velocity $\hat{u}_i$ is solved implicitly using the linear system of equations shown in equation 2.5.

$$\left(1 - \frac{\Delta t}{2\mathrm{Re}}\frac{\partial^2}{\partial x_3^2}\right)\hat{u}_i \approx u_i^n + \frac{\Delta t}{2}M_i^n \tag{2.5}$$

with

$$M_i^n = \frac{1}{\mathrm{Re}}\frac{\partial^2 u_i^n}{\partial x_3^2} \tag{2.6}$$

The remaining terms in equation 2.2 are solved using the explicit Adams-Bashforth scheme as shown in equation 2.7,

$$\frac{\hat{u}_i - u_i^n}{\Delta t} \approx \frac{3}{2}L_i^n - \frac{1}{2}L_i^{n-1} + \mathcal{O}\left(\Delta t^2\right) \tag{2.7}$$

where

$$L_i^n = -\frac{\partial u_i^n u_j^n}{\partial x_j} - \frac{1}{\mathrm{Ro}}u_j^n \varepsilon_{ji3} - \frac{\partial P}{\partial x_i} + \frac{1}{\mathrm{Re}}\left(\frac{\partial^2 u_i^n}{\partial x_1^2} + \frac{\partial^2 u_i^n}{\partial x_2^2}\right) \tag{2.8}$$

Combining both expressions from the Adams-Bashforth and Crank-Nicholson schemes yields the expression for the predicted velocity in equation 2.9.

$$\left(1 - \frac{\Delta t}{2\mathrm{Re}}\frac{\partial^2}{\partial x_3^2}\right)\hat{u}_i = u_i^n + \Delta t\left(\frac{1}{2}M_i^n + \frac{3}{2}L_i^n - \frac{1}{2}L_i^{n-1}\right) \tag{2.9}$$

Once the predicted velocity $\hat{u}_i$ is computed, the velocity at the next time step $(n+1)$ is found by applying a corrector step as shown in equation 2.10, with ϕ representing the pseudo-pressure.

$$u_i^{n+1} = \hat{u}_i - \Delta t\frac{\partial \phi}{\partial x_i} \tag{2.10}$$

The pseudo-pressure is computed by taking the divergence of equation 2.10 and enforcing equation 2.1 (continuity) at the next time step, yielding the expression shown in equation 2.11.

$$-\Delta t\frac{\partial^2 \phi}{\partial x_i \partial x_i} = \frac{\partial \hat{u}_i}{\partial x_i} \tag{2.11}$$

The spatial derivatives are computed using a finite-difference approximation in all coordinate directions with fourth order central differences by means of high-order Lagrangian polynomials. The streamwise (u) and spanwise (w) velocity components are discretized on a "centered" vertical mesh, while the wall-normal (v) velocity component is discretized on a "staggered" vertical mesh to enhance coupling between the vertical velocity and the pressure (Waggy et al., 2013).

In order to dissipate excess energy that remains unsolved by the grid when applying finite difference methods, an artificial viscosity in physical space must be implemented to ensure numerical smoothing and account for dealiasing. In this numerical integration scheme, this is applied by adding a high-order dissipation term to the finite difference equations as shown in equation 2.12.

$$L_i^n = \cdots + \beta \Delta x_j^4 \frac{\partial^4 u_i^n}{\partial x_j^4} \tag{2.12}$$

To prevent reflections at the outflow boundary for the spatial channel model, a buffer domain technique is employed to set the convective terms in the streamwise perturbation equations to zero using a coefficient function, allowing perturbations to be convected by the base flow out of the computational domain (Kucala, 2015, Kucala and Biringen, 2014). In general, the length of the buffer domain is about 20 to 30 percent of the physical domain.

2.3 Simulation Case Descriptions

The full listing of simulations and their corresponding grid resolutions are found in the case descriptions (table 3.3). Using the periodic model, four simulation cases *A*-*D* were conducted for Rossby numbers $Ro_b = 0$, 0.2, 0.5 and 0.9 to view the effects of rotational forces for a wide range of rotation rates. An additional higher-Reynolds number simulation case *E* was conducted using the periodic model for $Ro_b = 0.2$ to examine rotational effects in higher-Reynolds number flows; simulation case *S* was conducted using the spatial model for non-rotating turbulent channel flow. For simulation cases *A*-*D*, the Reynolds number based on the laminar centerline velocity $Re_c = 8000$ was kept constant which resulted in a friction Reynolds number $Re_\tau = 200$ for the no-rotation case ($Ro_b = 0$). The low Reynolds number was chosen such that reasonable comparisons could be made with previous DNS studies of rotating turbulent channel flow with similar Reynolds numbers (Grundestam et al., 2008, Kristofferson and Andersson, 1993). For simulation case *E*, the Reynolds number based on the laminar centerline velocity was kept constant at $Re_c = 27000$ which resulted in a friction Reynolds number $Re_\tau = 406$. The asymmetric velocity distributions due to the rotational effects decreased the value of Re_τ which was calculated as an average between the two walls. Simulations were performed at constant mass flux which resulted in a bulk Reynolds number $Re_b = u_b\delta/\nu$, where u_b is the mean bulk velocity defined as

$$u_b = \frac{1}{2\delta}\int_0^{2\delta} \overline{u} dy \tag{2.13}$$

where $\overline{u}$ denotes a plane-averaged quantity. The domain lengths for the periodic simulations were selected as $L_x = 4\pi\delta$, $L_y = 2\delta$ and $L_z = 2\pi\delta$ such that two-point spatial autocorrelations in the streamwise and spanwise directions converged to zero at the largest separations. The domain lengths for the spatial simulation were selected as $L_x = 4\pi\delta$, $L_y = 2\delta$ and $L_z = \pi\delta$.

All solutions for the elliptic pressure equation, and the spatially elliptic momentum equations are obtained using iterative methods available on the Portable, Extensible Toolkit for Scientific Computation (PETSc) library at the Texas Advanced Computating Center (TACC). As PETSc routines are designed for solving massive systems of equations, implementation of the PETSc li-

Table 2.1: Case descriptions and initial conditions.

Case	Re_τ	Ro_b	$nx \times ny \times nz$
A	200	0	$256 \times 129 \times 256$
B	197	0.2	$256 \times 129 \times 256$
C	192	0.5	$256 \times 129 \times 256$
D	183	0.9	$256 \times 383 \times 256$
E	406	0.2	$512 \times 513 \times 512$
S	200	0	$200 \times 97 \times 128$

braries enabled the simulation code to run optimally using as few processors as possible. As linear solvers are necessary to compute the pseudo-pressure and predicted velocity, all solutions were obtained using Krylov subspace methods found within the routines of the PETSc library. To validate the accuracy of the code, numerical solutions were compared with the hydrodynamic linear stability theory for plane channel (Poiseuille) flow. By measuring the growth rate and phase speed of a primary two-dimensional disturbance from the computation and comparing these values to the eigenvalues of the Orr-Sommerfeld equation, the accuracy of the code was assessed. Excellent agreement between the theoretical predictions and DNS results was observed (less than 1% deviation in amplitude) which gives confidence to the viability of the code for solving the unsteady incompressible Navier-Stokes equations. More information on the code scheme and verification may be found in the appendix and Waggy et al. (2011, 2013, 2014, 2015). Quantities denoted by subscripts of m, c, and τ correspond to scaling using the mean bulk velocity, mean channel centerline velocity, and global friction velocity, respectively. The original data base for the non-rotating case A was initialized from an non-converged data field of non-rotating turbulent channel flow given to this work's author by colleague Alec Kucala.

Mesh independence was established by designating two high-resolution cases with grid numbers $nx \times 2ny \times nz$ for case A ($Ro_b = 0$) and $2nx \times ny \times 2nz$ for case D ($Ro_b = 0.9$). For both cases, the distributions of mean velocity, Reynolds stresses and turbulent kinetic energy budgets compared very favorably to those of the original simulations, demonstrating the selected meshes of the present DNS cases were mesh invariant. The grid spacing is also comparable to other DNS

studies of spanwise-rotating turbulent channel flow (Grundestam et al., 2008, Kristofferson and Andersson, 1993).

Superscript "+" refers to nondimensionalization by the friction velocity, $u_\tau = \sqrt{\nu \partial \overline{u}/\partial y|_{\text{wall}}}$ or friction temperature, $T_\tau = (\kappa/u_\tau)\partial\theta/\partial y|_{\text{wall}}$. The global friction velocity for the rotational cases is denoted as $u_\tau = \sqrt{u_{\tau s}^2/2 + u_{\tau p}^2/2}$ where $u_{\tau s}$ and $u_{\tau p}$ are the local friction velocities at the suction and pressure walls, respectively; an equivalent calculation of the global friction temperature was used for the thermal statistics. Unless otherwise specified, all coordinate directions are nondimensionalized by δ. For all cases, the governing equations were integrated until both the friction Reynolds number Re_τ and friction temperature converged availing a sufficiently long time window ($t^+ = tu_\tau^2/\nu \geq 1000$) to calculate statistics.

2.4 Code Verification

In fully resolved turbulent flow, energy spectra should demonstrate an energy density roll-off of several decades with increasing wavenumber and negligible aliasing at high wavenumbers (Kim et al., 1987). Sample power spectra (E) for case A and case S are shown in figures 2.2(a) and (b), respectively. In figure 2.2(a), the streamwise energy spectra for case A demonstrate energy drop-off with no aliasing at high wavenumbers, characteristic of low-Reynolds number turbulence with discernable inertial and dissipative energy scales (Kim et al., 1987). In figure 2.2(b), the energy spectra for case S is provided for the nondimensional frequency f and also displays proper realization of the energetic scales.

In figure 2.3(a), the mean velocity distributions across the channel for cases P and S are shown to be identical and properly represent the profile of a turbulent flow field. In figure 2.3(b), both mean velocity distributions are also demonstrated to correspond well with the law of the wall: $\overline{u}^+ = y^+$ in the viscous sublayer ($y^+ < 5$) and $\overline{u}^+ = 2.5\, ln(y^+) + 5.8$ in the log-law region ($y^+ > 30$).

In figure 2.4, the normalized root-mean-square (r.m.s.) fluctuating velocities for both simulation cases are compared with the experimental hot-film data in Kreplin and Eckelmann (1979) and

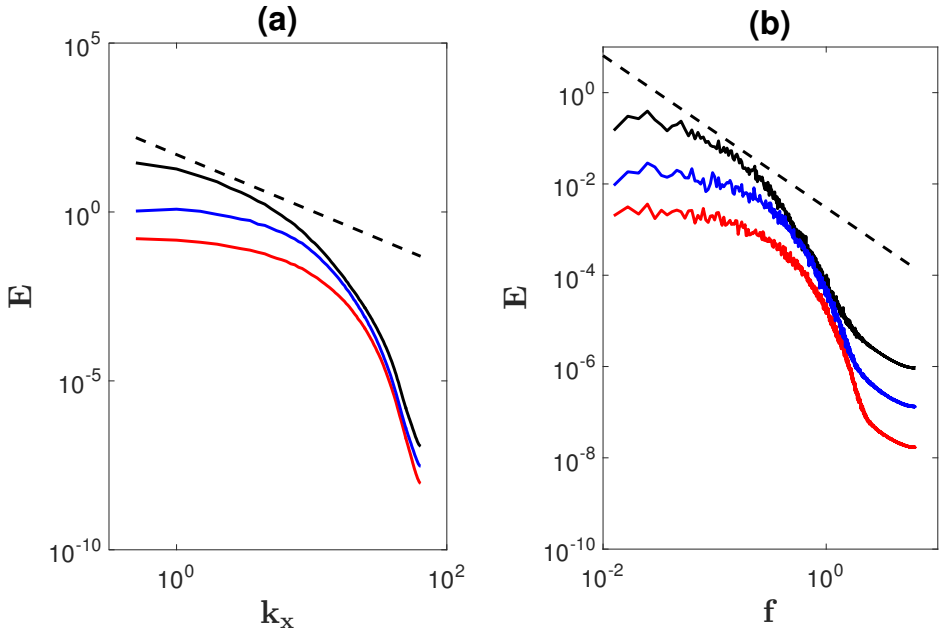

Figure 2.2: One-dimensional energy spectra. (a) Case A; (b) Case S. Black: E_{uu}; red: E_{vv}; blue: E_{ww}; dashed: Kolmogorov $-5/3$ spectrum.

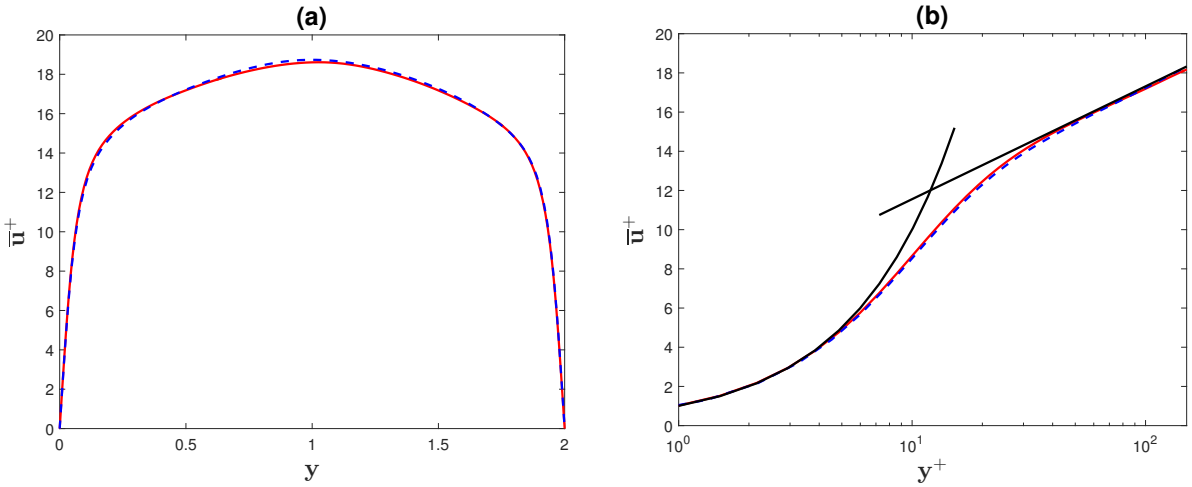

Figure 2.3: Mean velocity profiles for cases A and S. (a) Channel distribution. (b) Law of the wall. Red: case A; blue: case S; black: law of the wall: $\overline{u}^+ = y^+$ at $y^+ < 5$ and $\overline{u}^+ = 2.5\, ln(y^+) + 5.8$ at $y^+ > 30$.

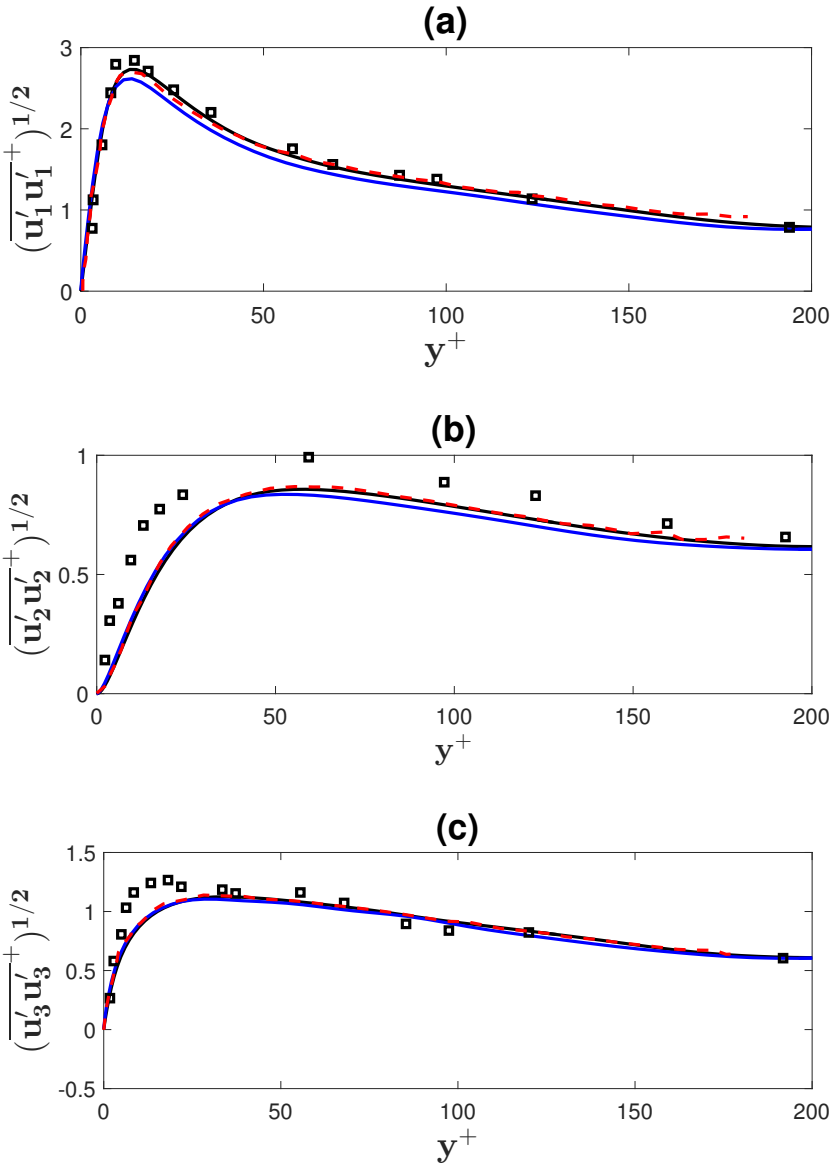

Figure 2.4: Verification of normalized root-mean-square velocity fluctuations for cases *A* and *S*. (a) u'_{rms}; (b) v'_{rms}; (c) w'_{rms}. Black: case *A*; blue: case *S*; red: Kasagi and Nishino (1991); square: Kreplin and Eckelmann (1979).

particle-tracking velocimetry data (PTV) in Kasagi and Nishino (1991). Both experiments were performed at a friction Reynolds number $Re_\tau \approx 205$. The reason for the discrepancy between the experimental data for v'_{rms} and w'_{rms} was explained by Kim et al. (1987) to be the result of suspect measurements from wall proximity. The present DNS results especially for case A are shown to compare very favorably to the PTV data for all r.m.s. velocities.

Chapter 3

Simple and Complex Turbulent Flows

3.1 Simple Turbulence: Turbulent Channel Flow

3.1.1 Theoretical Models of Coherent Structures

In this section, visualizations from the turbulent channel flow simulation cases A and S are used to substantiate the theoretical model predictions proposed by Landahl (1990), Lengani and Simoni (2015), Sirovich et al. (1990). The DNS data from the periodic channel model in case A is used to validate all three model predictions and results from the spatial channel simulation case S are used to corroborate the periodic model validations for the theoretical models proposed by Lengani and Simoni (2015) and Sirovich et al. (1990).

The Landahl model proposes the formation of sublayers streaks, or streamwise elongated u' structures, is a consequence of algebraic instabilities commonly found in turbulent flows (Landahl, 1980). The streaks are generated by the continuous linear growth of these algebraic instabilities in the streamwise (x) direction, necessitated by a linear temporal growth of total streamwise momentum which continues indefinitely until viscous forces impede growth. Landahl (1990) used the conditional sampling technique of variable interval time averaging (VITA) to obtain flow visualizations demonstrating the temporal structural evolution suggested by the theoretical model. The model proposed two structure classes which formed from the original algebraic instabilities: symmetrical and asymmetrical structures which correspond with oblique defomation angles in the spanwise direction of $\theta = 0^\circ$ and $\theta = 5^\circ$, respectively. As the symmetrical structures did not

demonstrate streamwise elongation over time, Landahl (1990) related the asymmetrical structures to sublayer streaks. The asymmetrical structures demonstrated a consistent pattern dominated by a high-speed structure side-by-side in the spanwise direction with a low-speed structure. Once these structures elongated, an irregular wavy appearance was observed consistent with the oscillatory motion of streaks (Kim et al., 1971).

The present DNS results are also used to evaluate the coherent structure formation scheme proposed in the experimental study by Lengani and Simoni (2015) which used Particle Image Velocimetry (PIV) to examine a low-pressure-turbine blade flow regime. In contrast to the study by Landahl (1990) which studied the initial development and evolution of sublayer streaks, Lengani and Simoni (2015) examined the formation of complex three-dimensional coherent structures which accompanied streak breakdown into turbulence. It was proposed that the breakdown of elongated sublayer streaks in the near-wall region induced three-dimensional vortical structures which manifested on the streak flanks. These large-scale structures were related to hairpin vortices (Adrian, 2007), characterized by spanwise vorticity on the top and wall-normal vorticity on the bottom legs. Smaller observed vortical structures, such as vorticity tubes, were proposed to be residuals of the hairpin vortices which contributed to the sinuous motion of the streaks. The breakdown of streaks and these vortical structures generate high velocity fluctuations and lead to the formation of other large-scale turbulence structures.

The study of Sirovich et al. (1990) postulated the existence of secondary instabilities, mainly propagating plane waves, which serve as a "trigger" for the interactions between these primary turbulence structures. Landahl (1972) was one of the first to qualitatively analyze the role of these secondary instabilities to the transition process and the later studies of Bayly et al. (1988), Herbert (1988) supported this mechanism by discovering these secondary instabilities travel obliquely to the streamwise direction and contributed to flow de-stabilization. The flow control studies by Murakami et al. (1992) and Handler et al. (1993) additionally affirmed the proposal by demonstrating that the phase randomization of a small subset of propagating modes, primarily within the energy-containing scales, reduced turbulent kinetic energy and drag by significant amounts. The present

work aims to substantiate the low-Reynolds number results ($Re_\tau = 120$) of Sirovich et al. (1991) for a turbulent flow field at $Re_\tau = 200$ and demonstrate the existence of these propagating waves in a spatial channel for application to future parametric studies for flow control (Xu, Rempfer, and Lumley, 2003). It is imperative to also establish propagating plane waves in a spatial channel due to the significantly more realistic application of the spatial model compared to the periodic model. However, the lack of directly imposed periodicity in the streamwise direction for the spatial channel eliminates the streamwise wavenumber, a necessary component of the theoretical model of Sirovich et al. (1990). Therefore, an alternative proof and analysis is used for the spatial model in the present work which replaces the streamwise wavenumber with a spatial-like wavenumber derived from a temporal frequency and streamwise convection velocity. To establish the existence of spanwise-propagating plane waves, the method of principal orthogonal decomposition (POD) is used to analyze both a spatial and periodic channel.

3.1.1.1 Landahl Model

The Landahl model qualitatively examined the formation and evolution of sublayers streaks in the turbulence system cycle and used the variable interval time averaging (VITA) method to predict structural characteristics suggested by the theoretical model. From the present DNS results in case A, maps of fluctuating streamwise velocity u' are obtained in the x-z plane of peak turbulent kinetic energy production ($y^+ = 15$). To obtain figure 3.1(a), the variable interval spatial averaging (VISA) method (Alfredsson et al., 1988) was applied with an averaging length of 200 wall units in the streamwise and spanwise directions. In accordance with the VISA method, a detection criterion was used to isolate "islands" of high local u' variance and the space-time position of these islands was tracked to visualize the temporal evolution of sublayer streaks. These VISA-educed structures are compared to the asymmetrical structures obtained from the modeled VITA results of Landahl (1990) and numerical VISA results of Alfredsson and Johansson (1988) in figures 3.1(b) and (c), respectively.

All three patterns demonstrate a structural inclination of approximately $\theta = 5^\circ$ in accordance

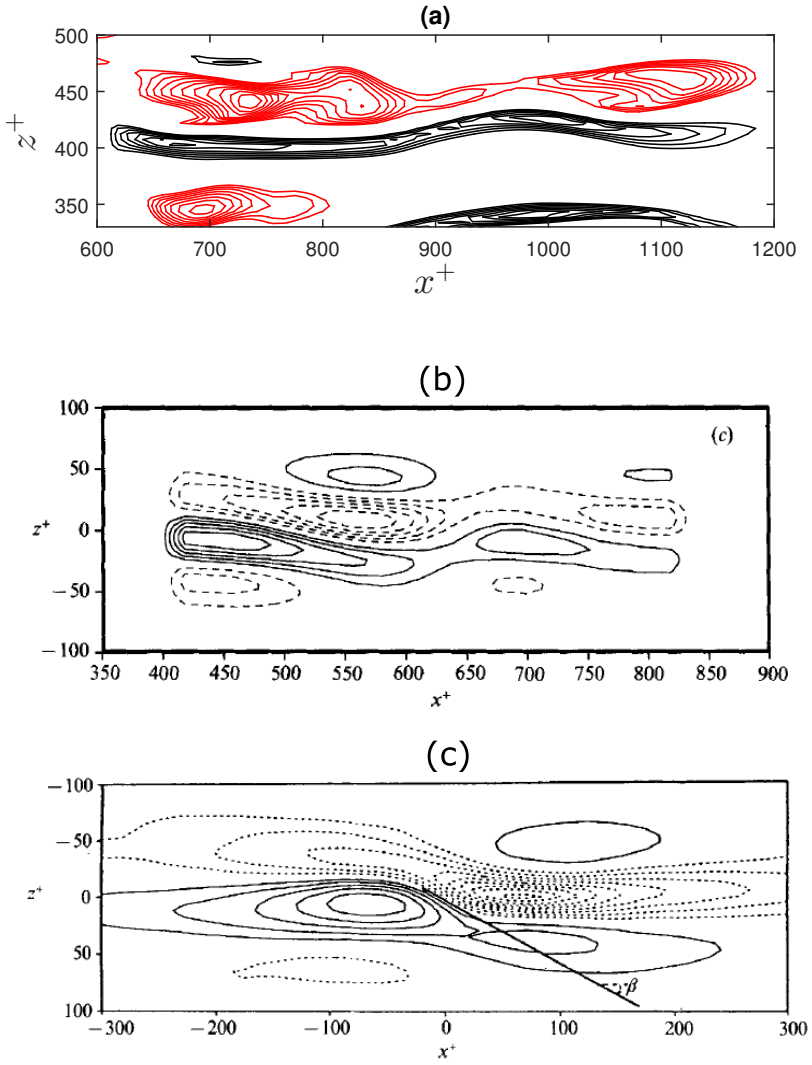

Figure 3.1: Maps of constant u' at $y^+ = 15$. a) Numerical VISA-educed streaks from case A; b) Modeled VITA-educed asymmetrical structures (Landahl, 1990); c) Numerical VISA-educed asymmetrical structures (Alfredsson and Johansson, 1988).

with the theory of Landahl (1990). The spanwise lengths of the streak patterns are also shown to be very similar at approximately $z^+ = 100$, corresponding to the accepted mean spacing between sublayer streaks (Alfredsson and Johansson, 1988). The numerical and modeled results display a comparable streamwise streak length of approximately $x^+ = 500$, demonstrating the three streak patterns are in a similar stage of development. The present DNS results in figure 3.1(a) show more similarity with the theoretical model of Landahl (1990), demonstrating an abrupt onset of the disturbed region and more discernable wavy structure in correspondence with the modeled results in figure 3.1(b).

Similarities with the theoretical model of Landahl (1990) are also observed in the temporal evolution of VISA-educed structures from the present DNS in figure 3.2. The familiar spanwise array of aligned high-speed and low-speed streaks is observed and this pattern demonstrates the expected streamwise advection and elongation for increasing t^+. Similar to the modeled asymmetrical structures, the present DNS results show a consistent oscillatory shape with an increasing amount of inflection points over time.

3.1.1.2 Lengani-Simoni Model

The Lengani and Simoni (2015) model proposed complex three-dimensional coherent structures accompanied the sublayer streaks of turbulence sustenance cycle. These three-dimensional vortical structures manifested as vorticity tubes on the streak flanks or hairpin vortices which envelop the streak. In figure 3.3, a three-dimensional contour representation of the near-wall coherent structures is shown for a single low-speed sublayer streak near the bottom channel wall ($y = 0$) for the periodic channel. The blue streaky structure denotes high levels of negative streamwise fluctuating velocity and the yellow hairpin vortex is composed from high levels of combined spanwise ($\omega_z^{'}$). and wall-normal vorticity ($\omega_y^{'}$). The smaller yellow vortical structures aligned with the streak in the spanwise direction denote high levels of streamwise vorticity ($\omega_x^{'}$) and the vorticity field is filtered such that the coherent structures are isolated from one another.

Both views of the streak in figures 3.3(a) and (b) demonstrate good agreement with the pro-

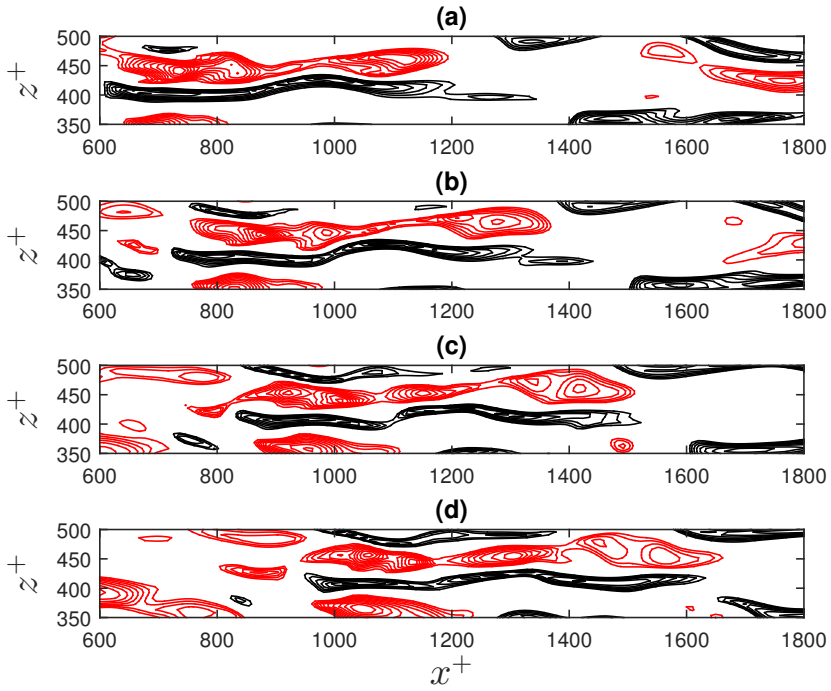

Figure 3.2: VISA-educed maps of constant $u^{'}$ at $y^+ = 15$ for case A. a) $t^+ = 0$; b) $t^+ = 10$; c) $t^+ = 20$; d) $t^+ = 30$. Isoline increment = 0.01; black lines: $u^{'} \leq -0.06$; red lines: $u^{'} \geq 0.06$. $t^+ = 0$ is a starting reference time.

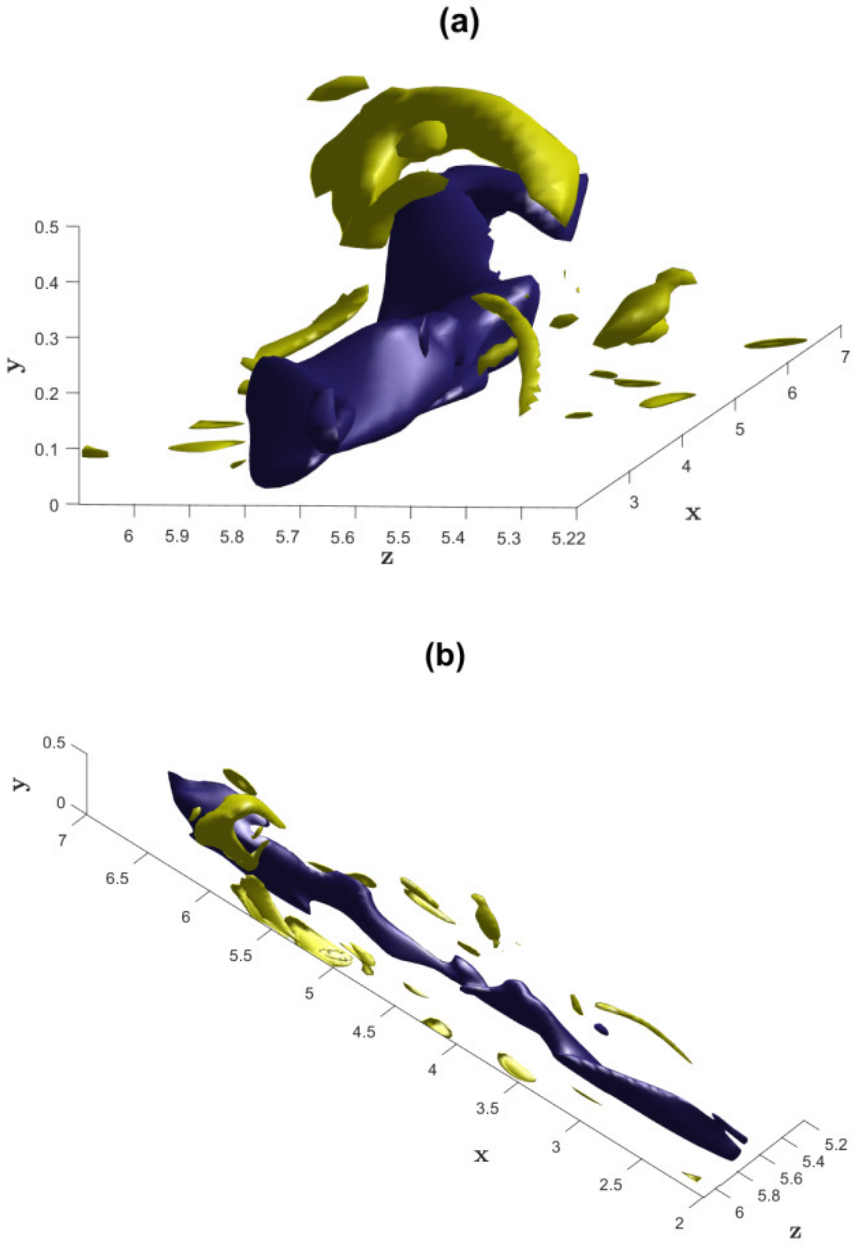

Figure 3.3: An isolated three-dimensional field of coherent structures in the near-wall region for simulation case *A*. Blue contours: sublayer streak; yellow contours: vorticity field. a) Front view; b) top view.

posed coherent structure organization by Lengani and Simoni (2015). The sinuous sublayer streak is accompanied by a large hairpin vortex, characterized by spanwise and wall-normal vorticity, which envelops a portion of the streak. The smaller vortical structures are observed to coincide with the sinuous, wavy motion of the sublayer streak in figure 3.3(b). These numerical results support the proposed development of three-dimensional vortical structures induced by sinuous sublayer streaks close to breakdown. Figure 3.4 shows a similar coherent structure organization for the spatial channel with a sinuous sublayer streak accompanied by a single hairpin vortex on top and vorticity tubes along the sides.

3.1.1.3 Sirovich Model

To visualize the spanwise-propagating plane waves proposed in Sirovich et al. (1991), the method of principal orthogonal decomposition was applied to a periodic and spatial channel. Principal orthogonal decomposition (POD), also known as the Karhunen-Loeve decomposition, is a procedure for extracting the coherent motions from two-point velocity correlations which contain the most energy (Lumley, 1970). Further detailed in Berkooz et al. (1993), this method is based on the decomposition of the velocity field

$$u_i = \sum_{q=1}^{ny} a^q \phi_i^q \tag{3.1}$$

where a^q and $\phi_i^q(y,z)$ are the basis-function coefficients and basis functions (eigenfunctions), respectively. q is the quantum number which refers to two-point separations in the inhomogeneous direction y. In addition, the basis-function coefficients correspond to their respective eigenvectors via

$$a^n = \frac{1}{2\delta} \int_0^{2\delta} u_i \phi_i^q dy \tag{3.2}$$

with satisfaction of the orthonormality condition for the eigenfunctions. The average mean energy of the velocity field is defined by

$$E_{ii} = \frac{1}{2\delta} \int_0^{2\delta} \frac{1}{2} u_i^2 dy \tag{3.3}$$

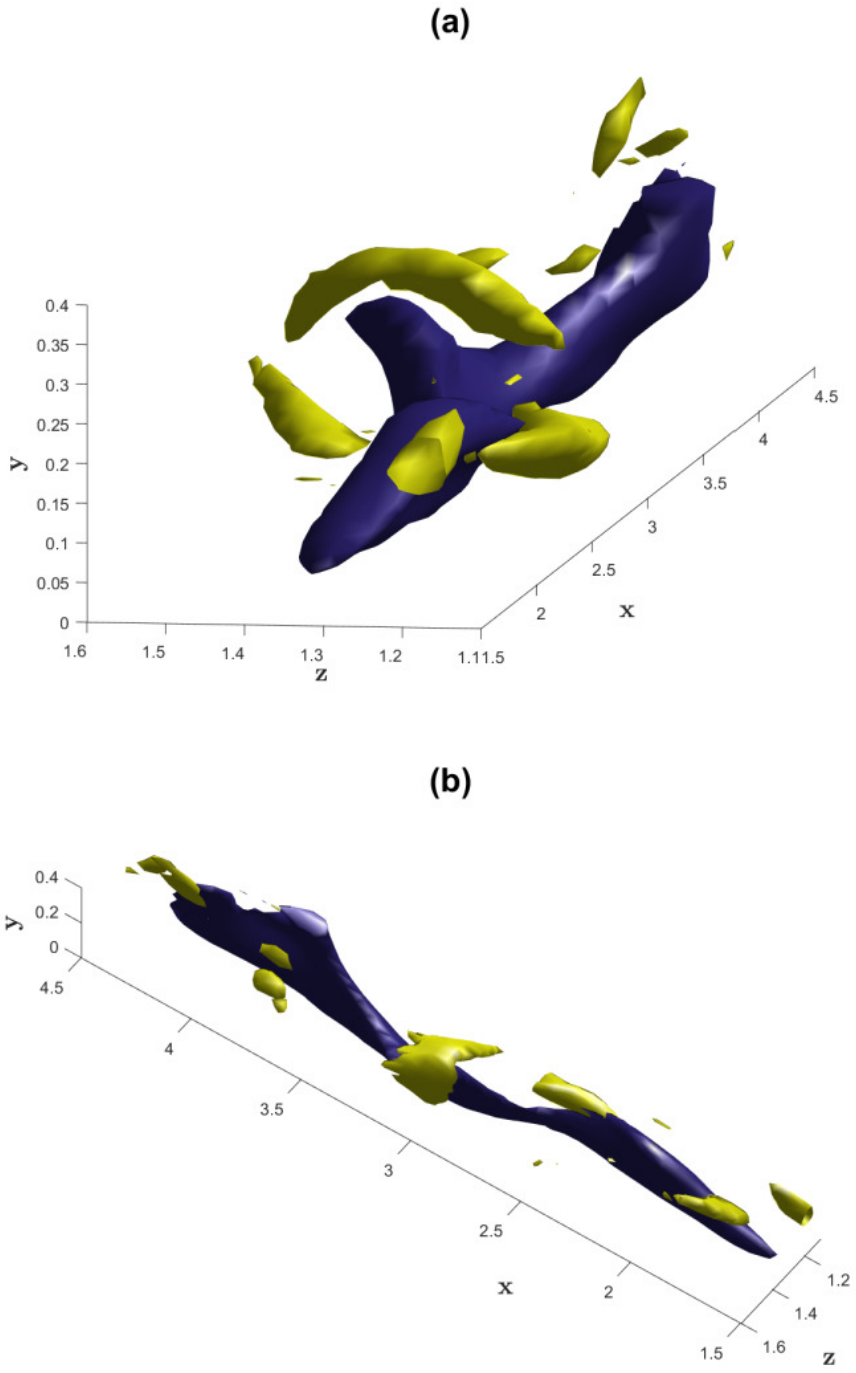

Figure 3.4: An isolated three-dimensional field of coherent structures in the near-wall region for simulation case *S*. Blue contours: sublayer streak; yellow contours: vorticity field. a) Front view; b) top view.

and through substitution of u_i in equation 3.1, the contribution of energy from various N modes is shown through the partial sum

$$E_N = \sum_{q=1}^{N} \frac{1}{2} a^{q2} \tag{3.4}$$

Using the above relations, an eigenvalue problem is created using the two-point autocorrelation tensor R_{ij}

$$\int_0^{2\delta} R_{ij} \phi_j^q dy = \lambda \phi_i^q \tag{3.5}$$

and if a structure contributes energy to the Reynolds stress tensor, it will dominate the two-point correlation statistics and manifest in the POD (Berkooz et al., 1993). For the periodic channel with periodicity in the streamwise (x) and spanwise (z) directions, the three-dimensional two-point correlation tensor is (Moin and Moser, 1989)

$$R_{ij}(r_x, y, y', r_z, t) = < u_i(x, y, z, t) u_j(x + r_x, y', z + r_z, t) > \tag{3.6}$$

where r_x and r_z represent the two-point separations $x - x'$ and $z - z'$ in the streamwise and spanwise directions, respectively. The brackets $<>$ denote ensemble averaging in time and the homogeneous x and z directions. For the spatial channel, the lack of directly imposed periodicity in the streamwise (x) direction prevents the streamwise wavenumber (k_1) which is replaced for POD analysis by a nondimensional frequency f, an important parameter for flow control designs which target specific frequencies. Considering two-point separations in time (r_t) and the periodic spanwise direction (r_z), the three-dimensional two-point correlation tensor for the spatial channel becomes

$$R_{ij}(y, y', r_z, r_t) = < u_i(x, y, z, t) u_j(x, y', z + r_z, t + r_t) > \tag{3.7}$$

with the brackets $<>$ denoting ensemble averaging in time, z and the quasi-periodic streamwise direction x.

For multi-dimensional POD analysis and application to three-dimensional turbulent channel flow, it is fitting to convert the two-point correlation tensor R_{ij} into the spectral density corre-

lation tensor Φ_{ij} (Moin and Moser, 1989)

$$\Phi_{ij}(k_x, y, y', k_z) = \frac{1}{4\pi^2} \int\int e^{-ik_x r_x - ik_z r_z} R_{ij}(r_x, y, y', r_z) dr_x dr_z \tag{3.8}$$

such that the flow field may be expressed as a function of streamwise (k_x) and spanwise wavenumbers (k_z) for the periodic channel. For the spatial channel, a similar transformation is made by performing a two-dimensional Fourier transform of the r_x-r_t planes of R_{ij} as a function of y and y'. For all wavenumber combinations, a Φ matrix of dimensions $3ny \times 3ny$ is assembled

$$\Phi = \begin{bmatrix} \Phi_{11} & \Phi_{12} & \Phi_{13} \\ \Phi_{21} & \Phi_{22} & \Phi_{23} \\ \Phi_{31} & \Phi_{32} & \Phi_{33} \end{bmatrix} \tag{3.9}$$

Hence, a new eigenvalue problem ($A\phi = \lambda\phi$) is generated where A, ϕ and λ represent the integrated spectral density correlation tensor, corresponding eigenfunction and eigenvalue matrices, respectively. To approximate the integral of Φ in the wall-normal y direction, the weighting function matrix D is calculated using the following trapezoidal numerical approximation (Reichert et al., 1994)

$$\int_0^{2\delta} \Phi dy = \sum_{i=1}^{ny} \omega_i \Phi_i = \frac{1}{2} \sum_{i=2}^{ny} (y_i - y_{i-1})[\Phi(y_{i-1}) + \Phi(y_i)] \tag{3.10}$$

where Φ_i is the value of Φ at a discrete grid point and ω_i is the corresponding weight function. To apply standard numerical eigenproblem solution techniques, it is required that the matrix-valued function A, or ΦD in the eigenproblem, be symmetric. This is accomplished through the following convolution

$$\Phi D\phi = \sqrt{D}\Phi\sqrt{D}\phi = \lambda\phi \tag{3.11}$$

Once the D and Φ matrices are created, the resultant eigenproblem is solved to return a system of eigenvalues and eigenfunctions for various modal combinations: (k_1, k_3, q) and (f, k_3, q) for the periodic and spatial POD analyses, respectively.

For both periodic and spatial POD analysis, instantaneous fluctuating velocity fields were collected from simulation cases A and S for a large time window. For an accurate and relevant

comparison to the results of Sirovich et al. (1991) regarding the wavenumber ranges, these fields were interpolated onto an approximately equivalent domain: $L_x = 5\delta$, $L_y = 2\delta$ and $L_z = \pi\delta$. Using the previously outlined procedure for periodic and spatial POD analysis, eigenvalues and eigenfunctions were obtained for a large number of modes.

In table 3.1, the top fifteen energetic modes and their corresponding energy fractions for simulation cases A and S are compared to the results of Sirovich et al. (1991) for a low Reynolds number $Re_\tau = 125$. m, n and o refer to indexes for the streamwise ($k_1 = 2\pi m/L_x$), spanwise wavenumbers ($k_3 = 2\pi n/L_z$) and frequency ($f = 2\pi o/(t_{end} - t_{init})$), respectively. As wavenumber corresponds to frequency by the relation $k = f/v$ where v is a convection velocity, a $f = 0$ mean mode is considered a non-propagating ($k_1 = 0$) mode for the spatial POD analysis. For all three cases, it is demonstrated that non-propagating modes, despite being a small fraction of the total number of modes, are the most energetic. Table 3.1 also demonstrates identical propagating modes which possess the highest energetical content such as the (1,3,1) and (1,2,1) modes, and that a small range of spanwise wavenumbers ($n = 2 - 4$) captures most of the highly energetic propagating modes. This findings supports the flow control design of Handler et al. (1993), which found that randomizing a small range of inertial scales reduced turbulent drag by significant amounts.

To visualize the presence and interactions of these propagating plane waves, Sirovich et al. (1990) derived a frequency and corresponding wave speed for these structures. Using the methodology of Sirovich et al. (1990) to calculate the wave speed for the most energetic propagating modes from table 3.1, we plot a normal speed locus for a discrete number of points for the periodic channel in figure 3.5. It is demonstrated that most waves do propagate at an oblique angle to the streamwise direction in accordance with the expectation of Sirovich et al. (1991).

In order to visualize propagating plane waves in the spatial POD analysis, f requires conversion to a spatial equivalent of the streamwise wavenumber. As Sirovich et al. (1991) postulated that these plane waves advected in the streamwise direction with the mean velocity, the following wavenumber relation $k_t = 2\pi f/v_x$ was used where v_x is the global convection velocity in the streamwise direction. By tracking the evolution of sublayer streaks in figure 3.2, a veloc-

Table 3.1: Energy content of the first 15 eigenfunctions obtained from POD analysis of simulation cases A and S. The Sirovich case refers to $Re_\tau = 125$ data taken from Sirovich et al. (1991).

	Sirovich		Case A		Case S	
Index	(m,n,q)	Energy Frac.	(m,n,q)	Energy Frac.	(o,n,q)	Energy Frac.
1	(0,3,1)	0.0428	(0,2,1)	0.0484	(0,4,1)	0.0500
2	(0,1,1)	0.0399	(0,1,1)	0.0299	(0,2,1)	0.0450
3	(0,4,1)	0.0327	(0,4,1)	0.0286	(0,3,1)	0.0401
4	(0,5,1)	0.0287	(0,3,1)	0.0246	(0,1,1)	0.0295
5	(0,4,2)	0.0229	(0,5,1)	0.0221	(1,1,1)	0.0236
6	(0,1,2)	0.0210	(0,6,1)	0.0208	(1,2,1)	0.0204
7	(0,3,2)	0.0206	(0,4,2)	0.0144	(1,5,1)	0.0198
8	(0,2,1)	0.0197	(0,7,1)	0.0136	(0,5,1)	0.0184
9	(0,2,2)	0.0188	(1,7,1)	0.0116	(0,0,1)	0.0181
10	(0,6,1)	0.0138	(1,4,1)	0.0105	(0,6,1)	0.0176
11	(0,5,2)	0.0131	(1,3,1)	0.0100	(3,1,1)	0.0164
12	(1,3,1)	0.0125	(1,3,2)	0.0092	(1,3,1)	0.0163
13	(1,2,1)	0.0095	(1,1,1)	0.0092	(1,4,1)	0.0159
14	(1,4,1)	0.0084	(1,2,1)	0.0092	(0,2,2)	0.0151
15	(1,5,1)	0.0083	(0,8,1)	0.0090	(1,0,1)	0.0148

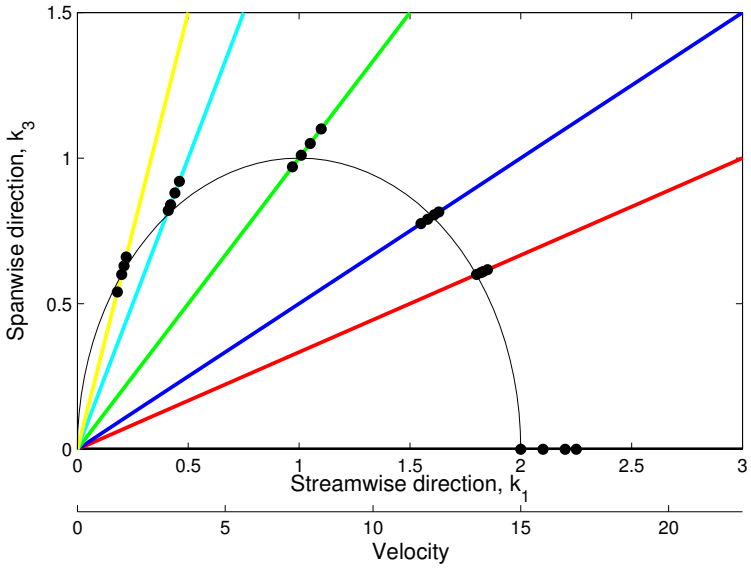

Figure 3.5: Normal speed locus for simulation case A. Dots represent the wavespeed of selected high energetic modes and lines represent high-energy wave envelopes. Black: (0,1) mode; red: (3,1) mode; blue: (2,1) mode; green: (1,1) mode; cyan: (1,2) mode; yellow: (1,3) mode.

ity $v_x = 0.25$ was calculated. Using this conversion for k_t, a normal locus plot was generated and shown in figure 3.6 for the spatial channel, demonstrating similar plane wave orientations to those found in the periodic POD analysis in figure 3.5.

Sirovich et al. (1991) additionally proposed a relationship between these plane wave envelopes and other energetic turbulence structures which advected with the mean flow velocity in the near-wall region, mainly the streaky structures and three-dimensional vortices discussed in the previous theoretical models, which form the bursting process. As the energy contained within the propagating modes is relatively small compared to the non-propagating modes (table 3.1), these plane wave modes were proposed by Sirovich et al. (1990) to be a triggering mechanism for bursting events with the non-propagating modes providing the energy cascade necessary for the bursts to occur. Through a decomposition of the Reynolds shear stress into separate contributions from the non-propagating and propagating modes, Sirovich et al. (1991) demonstrated the presence of both modes were necessary for strong turbulent activity. These discoveries bode well for future flow control efforts as the present work and Sirovich et al. (1990) have collectively shown that most of the turbulent kinetic energy is contained to a small range of modes. Since the propagating waves have been established in both periodic and spatial models despite the lack of a streamwise wavenumber in the spatial channel, flow control designs should aim to inhibit these particular modes to reduce turbulent kinetic energy and drag.

3.1.2 Summary

In summary, the theoretical model predictions proposed by Landahl (1990) and Lengani and Simoni (2015) for the coherent structures of sublayer streaks and accompanying vortical structures were validated through comparison with the present DNS results. For the Landahl (1990) model, the appearance and evolution of the sublayer streaks obtained using the VISA method from the DNS data coresponded very well with the modeled VITA results. For the Lengani and Simoni (2015) model, instantaneous snapshots of a sublayer streak and its surrounding vortical structures were obtained from both the periodic and spatial DNS simulations which matched the pictorial

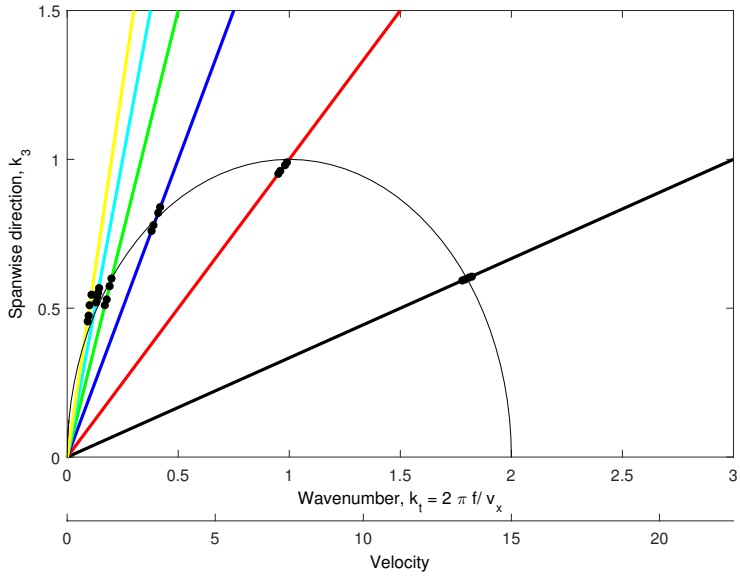

Figure 3.6: Normal speed locus for simulation case *S*. Dots represent the wavespeed of selected high energetic modes and lines represent high-energy wave envelopes. Black: (3,1) mode; red: (1,1) mode; blue: (1,2) mode; green: (1,3) mode; cyan: (1,4) mode; yellow: (1,5) mode.

representation of the theoretical model.

The principal orthogonal decomposition (POD) method was also applied to both a periodic and spatial channel to confirm the theory of propagating plane waves by Sirovich et al. (1991). In agreement with the results of Sirovich et al. (1991) for a lower Reynolds number, non-propagating modes were found to possess the highest energetical content and a normal speed locus was generated in order to visualize the interaction and movement of propagating plane waves. A new POD approach was designed for the spatial channel using two-point correlations in both space and time due to the elimination of the streamwise wavenumber k_1 and a frequency f was used as a replacement. The spatial POD analysis demonstrated similar results to the periodic analysis: mean modes ($f = 0$) corresponded with non-propagating modes and were consistent in containing the highest energy fractions. In addition, a similar spanwise wavenumber range ($n = 2 - 4$) was observed for the highly energetic propagating modes in both periodic and spatial analyses. A normal speed locus was then generated for the spatial channel which showed similar characteristics to the periodic speed locus. These plane wave modes and structures have direct relevance to flow control as the inhibition of the propagating modes would be ideal due to their relatively small energy content and also necessary function towards turbulence production.

3.2 Complex Turbulence: Effects of Rotation

3.2.1 Introduction

In this section, the DNS data base from periodic simulation cases A ($Ro_b = 0$), B ($Ro_b = 0.2$), C ($Ro_b = 0.5$) and D ($Ro_b = 0.9$) are examined for effects of rotational forces on turbulence over a wide range of rotation rates. In spanwise-rotating turbulent channel flow, the Coriolis force acts in the wall-normal direction, resulting in asymmetry across the channel and the creation of two distinct flow regimes: the pressure and suction regions. In the pressure region of the channel, secondary flow circulation and high levels of turbulence are present and in the suction region, re-laminarization of the regime results in low levels of turbulence.

3.2.2 Turbulence Statistics and Coherent Structures

3.2.2.1 General Turbulence and Thermal Statistics

Rotational effects on the mean velocity and temperature profiles are shown for simulation cases *A*-*D* in figures 3.7 and 3.8, respectively. In figure 3.7, the mean velocity profile is symmetric about the channel centerline ($y = 1$) for case *A* ($Ro_b = 0$). With system rotation, the mean velocity distributions become asymmetric as the flow regime is separated into the pressure and suction regions. For rotational cases *B*-*D*, a laminar-like (parabolic) profile is observed near the suction wall ($y = 0$) which is characteristic of the suppressed turbulence in the suction region. As the flow progressively relaminarizes with increasing rotation number, the suction region expands. Near the pressure wall ($y = 2$), a constant gradient of -2Ω is shown in the mean velocity profiles at all rotation rates which is consistent with previous DNS results in Grundestam et al. (2008) and Kristofferson and Andersson (1993). In figure 3.8, the thickness of the thermal diffusive sublayer, characterized by large near-wall temperature gradients, is broader near the suction wall than the pressure wall for rotating simulation cases *B*-*D*. As the rotation number increases, the size of the diffusive layer in the suction region increases and the mean temperature profile shifts towards the pressure wall (Liu and Lun, 2007).

In figure 3.35, the Reynolds stress distributions are shown for simulation cases *A*-*D*. The suppressed amplitudes near the suction wall compared to those near the pressure wall are displayed for all figures in the rotational cases. In figure 3.35(a), $\overline{u'u'}^+$ amplitudes are initially increased for case *B* ($Ro_b = 0.2$) near the pressure wall. However, the pressure wall amplitudes gradually decrease with increasing rotation number in cases *C* ($Ro_b = 0.5$) and *D* ($Ro_b = 0.9$). In figures 3.35(b) and (c), $\overline{v'v'}^+$ and $\overline{w'w'}^+$ amplitudes are shown to monotonically increase with rotation number in the pressure region. In figure 3.35(d), $\overline{u'v'}^+$ remain relatively consistent in the pressure region for the rotational cases.

To illustrate the effects of rotation on wall shear stress and heat transfer, the dimensionless friction Reynolds (Re_τ) and Nusselt (Nu) numbers for both channel walls are provided for

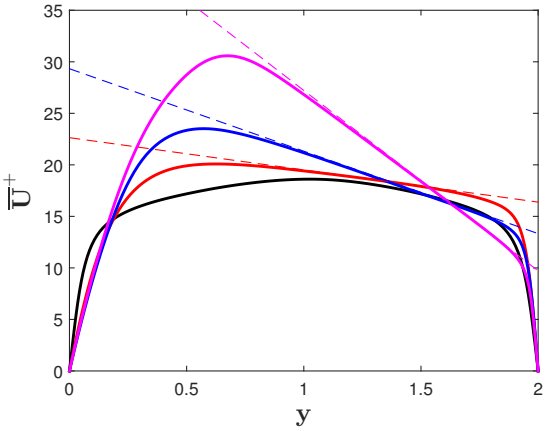

Figure 3.7: Mean velocity distributions with 2Ω lines for full simulation cases *A-D*. Black: case A ($Ro_b = 0$); red: case B ($Ro_b = 0.2$); blue: case C ($Ro_b = 0.5$); magenta: case D ($Ro_b = 0.9$). $- - -$: 2Ω lines.

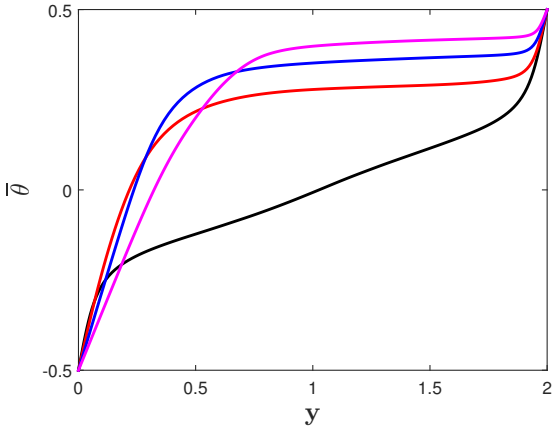

Figure 3.8: Mean temperature distributions for full simulation cases *A-D*. Black: case A ($Ro_b = 0$); red: case B ($Ro_b = 0.2$); blue: case C ($Ro_b = 0.5$); magenta: case D ($Ro_b = 0.9$).

the present simulation cases *A-D* in table 3.2. The introduction of rotation is shown to initially decrease Re_τ on the suction wall while increasing Re_τ on the pressure wall. At higher rotation numbers, these Re_τ trends are shown to significantly weaken or even reverse in case *D* ($Ro_b = 0.9$) for Re_τ on the pressure wall. These results correspond well with Grundestam et al. (2008) which demonstrated that Re_τ on both walls trended towards convergence at high rotation numbers until the eventual full re-laminarization of the flow regime. For the Nusselt number, a dimensionless

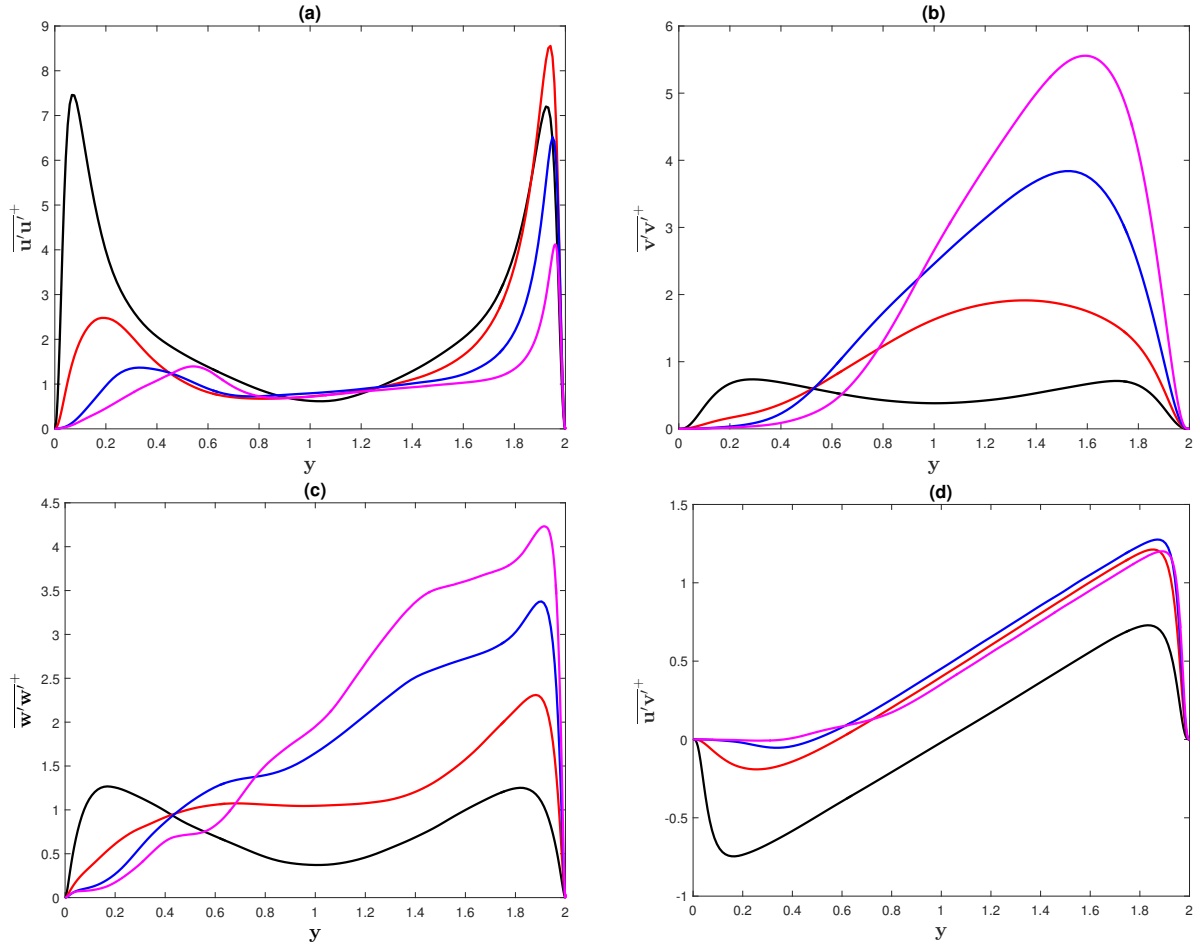

Figure 3.9: Reynolds stress distributions for full simulation cases *A-D*: a) $\overline{u'u'}^{+}$; b) $\overline{v'v'}^{+}$; c) $\overline{w'w'}^{+}$; d) $\overline{u'v'}^{+}$. Black: case A ($Ro_b = 0$); red: case B ($Ro_b = 0.2$); blue: case C ($Ro_b = 0.5$); magenta: case D ($Ro_b = 0.9$).

Table 3.2: Friction Reynolds (Re_τ) and Nusselt (Nu) numbers for present DNS cases A-D. Subscripts s and p denote the suction ($y = 0$) and pressure walls ($y = 2$), respectively.

$Case$	$(Re_\tau)_s$	$(Re_\tau)_p$	Nu_s	Nu_p
A	200	200	6.8	6.8
B	150	235	5.7	5.8
C	138	235	4.3	4.6
D	137	219	3.2	3.4

number generally used to represent surface heat transfer, increasing system rotation is shown to continually decrease Nu on both channel walls. This trend was similarly observed in Liu and Lun (2007).

3.2.2.2 Higher-Order Statistics

The third-moment of a fluctuating velocity component normalized by the cube of the root-mean-square (r.m.s.) velocity component is known as the skewness:

$$S(u_i^{'}) = \frac{\overline{u_i^{'} u_i^{'} u_i^{'}}}{(\overline{u_i^{'} u_i^{'}})^{3/2}} \tag{3.12}$$

The skewness quantifies the asymmetry of a variable's probability density function (PDF) distribution about its mean and measures extreme events occuring in a velocity field. For example, positive skewness indicates large amplitude positive fluctuations have a greater likelihood for occurrence than negative fluctuations of similar strength. The flatness (F), also known as the kurtosis, represents the fourth-order moment of a fluctuating velocity component normalized by the square of its corresponding Reynolds stress component:

$$F(u_i^{'}) = \frac{\overline{u_i^{'} u_i^{'} u_i^{'} u_i^{'}}}{(\overline{u_i^{'} u_i^{'}})^2} \tag{3.13}$$

The flatness is the measure of a variable's "peakedness" and "tailedness" (DeCarlo, 1997), representing the frequency at which extreme events occur as a deviation from the Gaussian distribution ($F = 3$). For example, a high value of flatness ($F > 3$) indicates relatively large values at the edges of the PDF distribution and a higher concentration directly around the mean.

To demonstrate the grid resolution for the full simulations is sufficient for proper higher-order statistics, the skewness and flatness distributions for case A ($Ro_b = 0$) is compared to the DNS results of Kim, Moin, and Moser (1987) and to the experimental measurements of Eckelmann (1974) and Barlow and Johnston (1985) in figures 3.10 and 3.11, respectively. Good agreement is shown between the present DNS and the referenced studies used for comparison. A significant discrepancy is observed for $F(v')$ between the experimental and numerical results; this was explained by Kim et al. (1987) as a result of suspected measurement inaccuracies in the proximity of the channel wall.

In figure 3.12, skewness and kurtosis distributions are shown for simulation cases A-D. Asymmetry for the rotational cases is observed in all profiles. In figures 3.12(a) and (c), rotation is shown to significantly increase values of $S(u')$ and $S(v')$ near the suction wall and decrease those values in the pressure region. In figure 3.12(e), $S(w')$ remains zero throughout the channel regardless of rotation number. In the kurtosis distributions, rotation is not shown to significantly alter the profile values in the pressure region even at high rotation numbers. In the suction region, there is a significant increase of kurtosis values for cases B ($Ro_b = 0.2$) and C ($Ro_b = 0.2$) from the non-rotational case but a decrease for case D ($Ro_b = 0.9$).

3.2.2.3 Energy Budgets

It is instructive to examine the various energy budget components in order to discover which force dynamics are primarily affected by rotational forces. The Reynolds stress equation displays the intercomponent energy transfer (Launder et al., 1975)

$$\frac{D\overline{u_i' u_j'}}{Dt} = P_{ij} + \Pi_{ij} - \varepsilon_{ij} + C_{ij} + D_{ij}^T \tag{3.14}$$

with the terms on the right-hand side of equation 3.14 representing, respectively, the production (P_{ij}), pressure-strain (Π_{ij}), dissipation (ε_{ij}), Coriolis (C_{ij}) and diffusion terms (D_{ij}^T).

In the present work, the production, Coriolis and pressure-strain budgets are investigated due to their high contribution level compared to the other budget terms and correspondence with

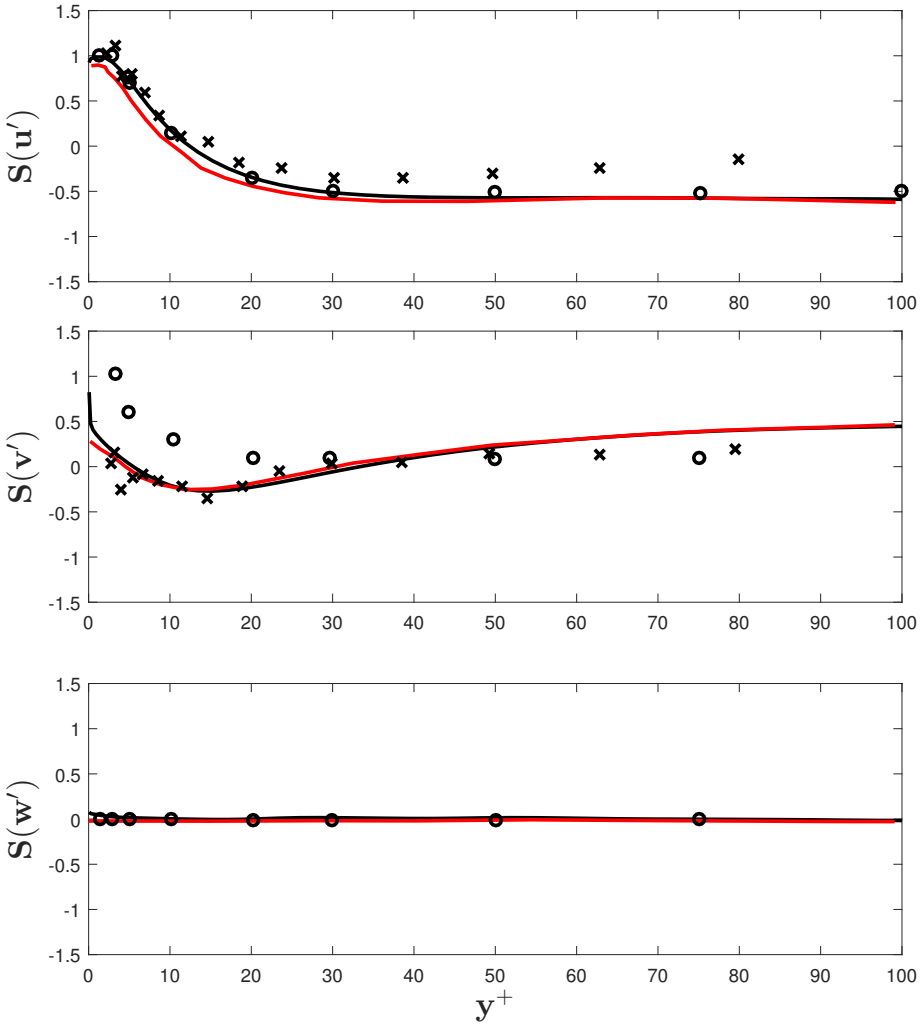

Figure 3.10: Validation of skewness statistics for case A ($Ro_b = 0$). Black lines: present simulations; red lines: Kim and Moin (1984); ○: Kreplin and Eckelmann (1974); x: Barlow and Johnston (1985).

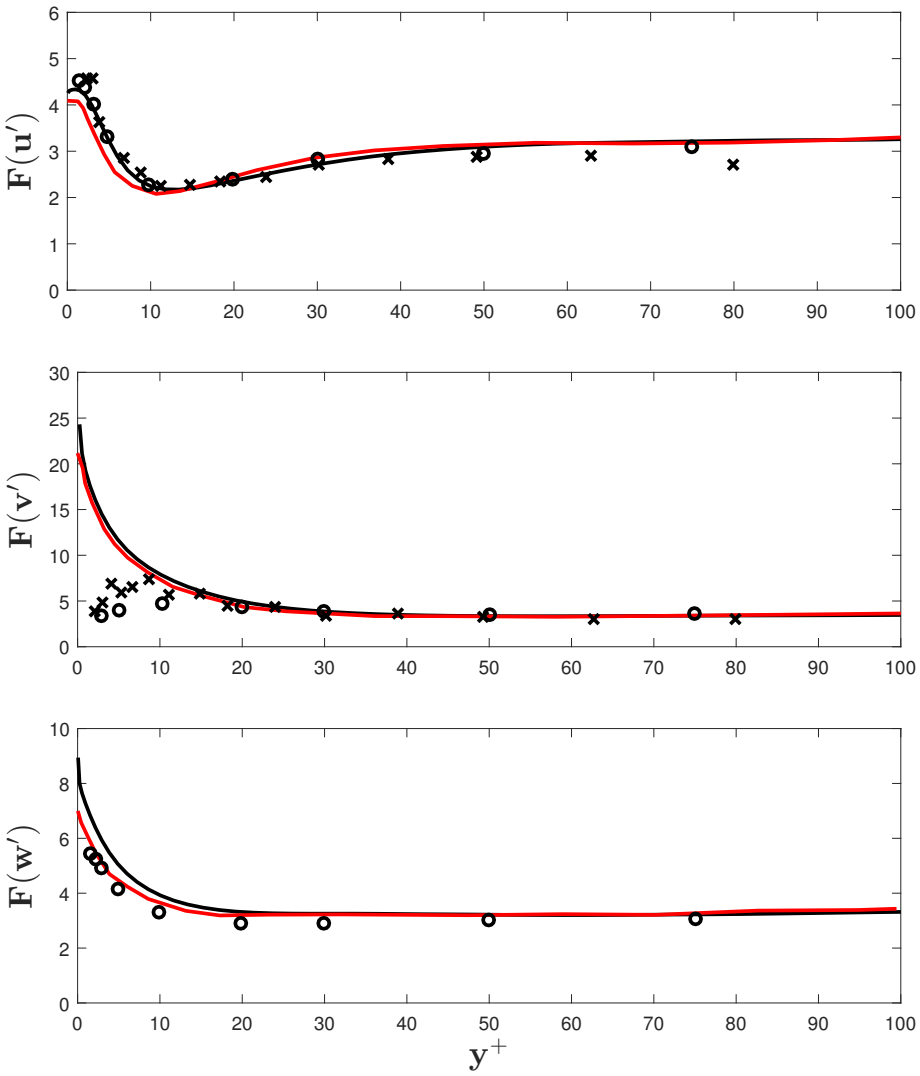

Figure 3.11: Validation of kurtosis statistics for case A ($Ro_b = 0$). Black lines: present simulations; red lines: Kim and Moin (1984); ○: Kreplin and Eckelmann (1974); x: Barlow and Johnston (1985).

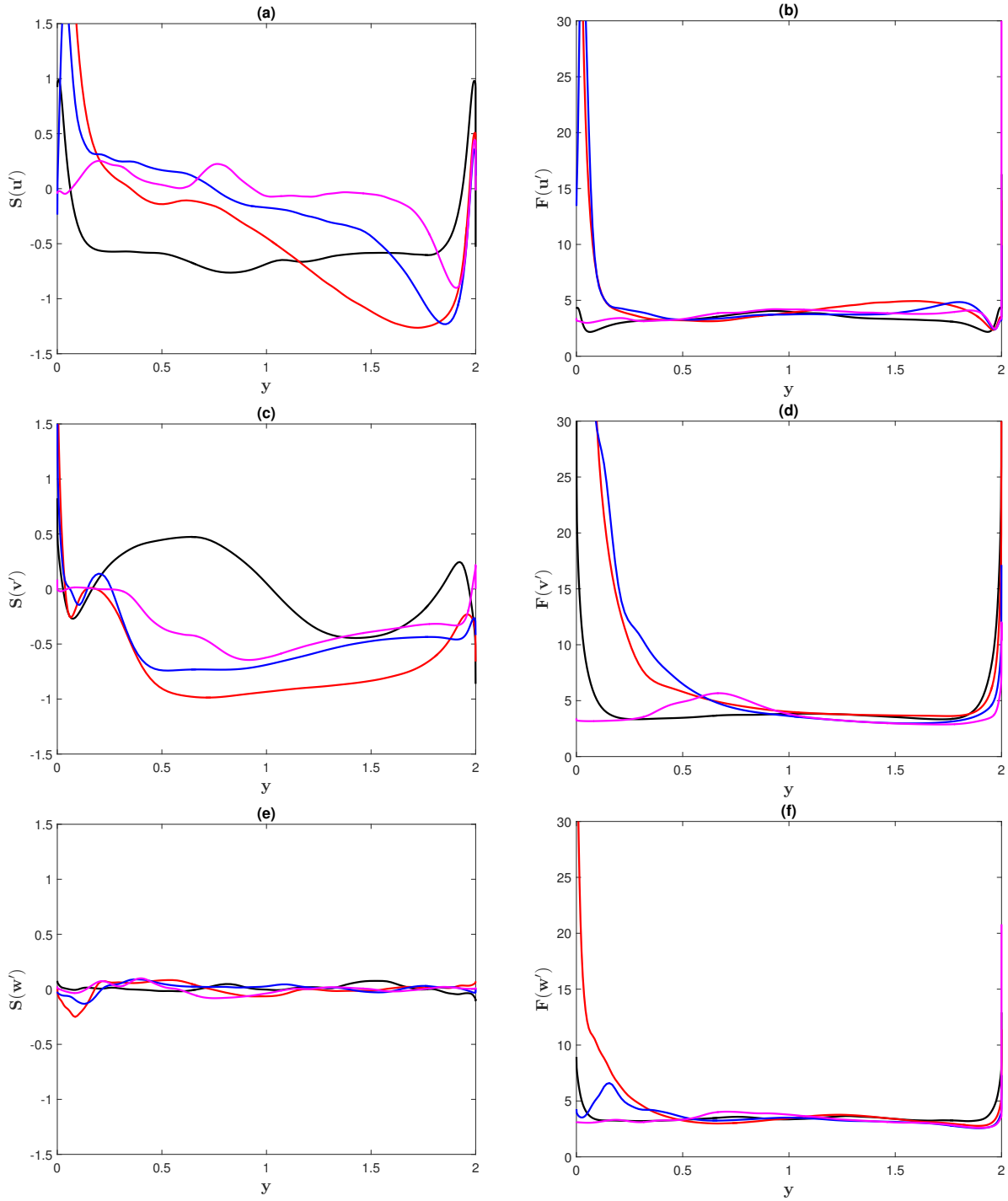

Figure 3.12: Skewness and kurtosis distributions for full simulation cases *A*-*D*: a) $S(u^{'})$; b) $F(u^{'})$; c) $S(v^{'})$; d) $F(v^{'})$; e) $S(w^{'})$; f) $F(w^{'})$. Black: case A ($Ro_{\mathrm{b}} = 0$); red: case B ($Ro_{\mathrm{b}} = 0.2$); blue: case C ($Ro_{\mathrm{b}} = 0.5$); magenta: case D ($Ro_{\mathrm{b}} = 0.9$).

the turbulence generation cycle (Kim et al., 1971). These quantities are expressed in tensor form in equations 3.15, 3.16 and 3.17

$$P_{ij} = -\overline{u_i' u_k'} \frac{\partial \overline{U}_j}{\partial x_k} - \overline{u_j' u_k'} \frac{\partial \overline{U}_i}{\partial x_k} \tag{3.15}$$

$$C_{ij} = 2\Omega_k (\overline{u_i' u_m'} \epsilon_{mjk} - \epsilon_{imk} \overline{u_m' u_j'}) \tag{3.16}$$

$$\Pi_{ij} = -\overline{(u_i' \frac{\partial p'}{\partial x_j} + u_j' \frac{\partial p'}{\partial x_i})} \tag{3.17}$$

and the total (summation of all tensor components) distributions are shown in figures 3.13(b), (c) and (d), respectively.

In figure 3.13(a), the turbulent kinetic energy (k) distributions for simulation cases A-D are shown. The expected suppression of k-amplitudes in the suction region is demonstrated for case B ($Ro_b = 0.2$), but a significant peak near the suction wall continues to persist despite the elimination of the turbulence sustenance cycle; no near-wall peak is observed for cases C ($Ro_b = 0.5$) and D ($Ro_b = 0.9$). In figure 3.13(b), rotational forces are demonstrated to suppress the amplitudes of production (P), the primary contributor to the near-wall k peak in figure 3.13(a) for case A ($Ro_b = 0$). A small near-wall contribution of P is shown for case B ($Ro_b = 0.2$) but is significantly diminished compared to case A ($Ro_b = 0$); no near-wall P contributions are observed for cases C ($Ro_b = 0.5$) and D ($Ro_b = 0.9$). Hence for case B ($Ro_b = 0.2$), the observed peak in figure 3.13(a) is demonstrated to be primarily composed of contributions from the other budget terms with a small supplement from P, demonstrating a fundamental alteration to the dominant processes which contribute towards turbulence production which manifests at low rotation numbers. At higher rotation numbers, re-laminarization mechanisms suppress turbulence production in the near-wall region of the suction side to negligible amounts.

In figure 3.13(c), the amplitudes of the pressure-strain distribution are shown to be suppressed for the rotational cases with the exception of the region next to the pressure wall ($y = 2$). In this region, the pressure-strain budget amplitudes monotonically increase with rotation number. In figure 3.13(d), the Coriolis force is shown to possess significant positive contributions in the suction region for the rotational cases, therefore supplementing the suction side amplitudes seen

in figure 3.13(a). However, the Coriolis force has significant negative contributions in the pressure region, counteracting the production contribution increases shown in figure 3.13(b).

3.2.2.4 Coherent Turbulence Structures

In this section, visualizations of various coherent structures are extracted from the full DNS cases *A*-*C* to ascertain the role of these structures to turbulence production amidst contributions from rotational forces. Although the bursting cycle is maintained in the pressure region (Kristoffferson and Andersson, 1993), the subsequent re-laminarization of the suction region and addition of rotation-induced structures dramatically increase the complexity of the flow regime.

In figure 3.14, maps of fluctuating streamwise vorticity $\omega_x^{'}$ are shown for a y-z crossflow section at $x = 2\pi$ for simulation cases *A*-*C*. In figure 3.14(a), there are spanwise arrays of alternating high and low-speed streaks near both channel walls for case *A* ($Ro_b = 0$) which also represent the local intensity of turbulence. In figures 3.14(b) and (c), the coherence of the high and low-speed structures is disrupted near the suction wall for cases *B* ($Ro_b = 0.2$) and *C* ($Ro_b = 0.5$). With increasing rotation number in the suction region, a significant reduction in the number of turbulence structures is observed along with the expansion of a near-wall region of completely suppressed turbulent activity. In contrast to the suction region, the pressure region continues to demonstrate high levels of turbulent activity and the coherence of turbulence structures is preserved for all rotation rates.

To assess the effects of re-laminarization on the structure of turbulence in the suction region, maps of fluctuating wall-normal vorticity ($\omega_y^{'}$) for full simulation cases *A*-*C* at horizontal x-z sections near the suction wall ($y = 0.06$) are shown in figure 3.15. Remarkable coherence of $\omega_y^{'}$ structures is observed. With $\omega_y^{'}$ dominated by $\partial u^{'}/\partial z$, the elongated structures of $\omega_y^{'}$ shown in figure 3.15(a) for case *A* ($Ro_b = 0$) may be considered the "sidewalls" of sublayer streaks as these structures are composed of significant concentrations, and therefore variations, of streamwise fluctuating velocity $u^{'}$ (Jimenez and Moin, 1991).

With the introduction of spanwise rotation in case *B* ($Ro_b = 0.2$), the wall-normal vorticity

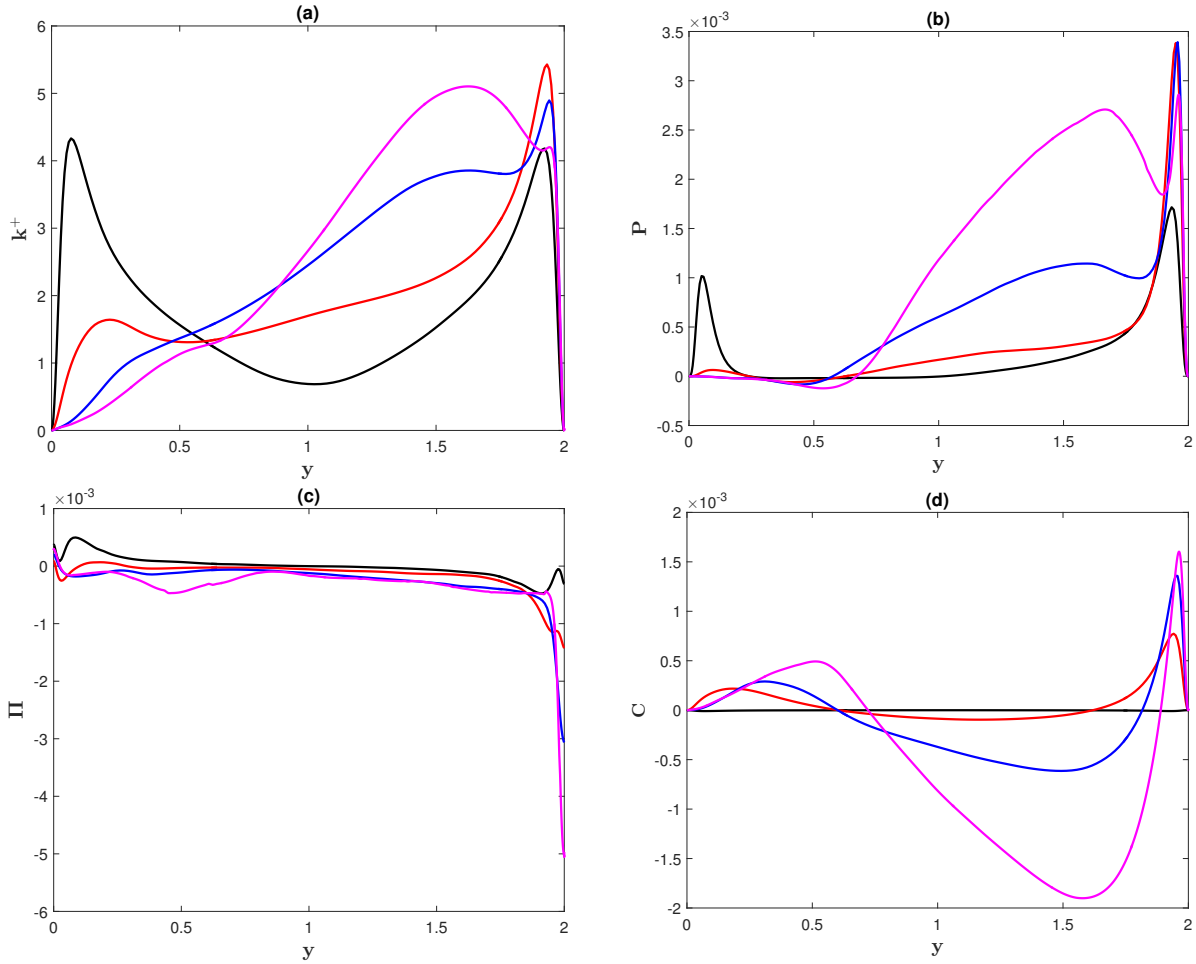

Figure 3.13: Turbulent kinetic energy and energy budgets for full simulation cases *A-D*: a) Turbulent kinetic energy; b) Production budget; c) Pressure-strain budget; d) Coriolis budget. Black: case A ($Ro_b = 0$); red: case B ($Ro_b = 0.2$); blue: case C ($Ro_b = 0.5$); magenta: case D ($Ro_b = 0.9$).

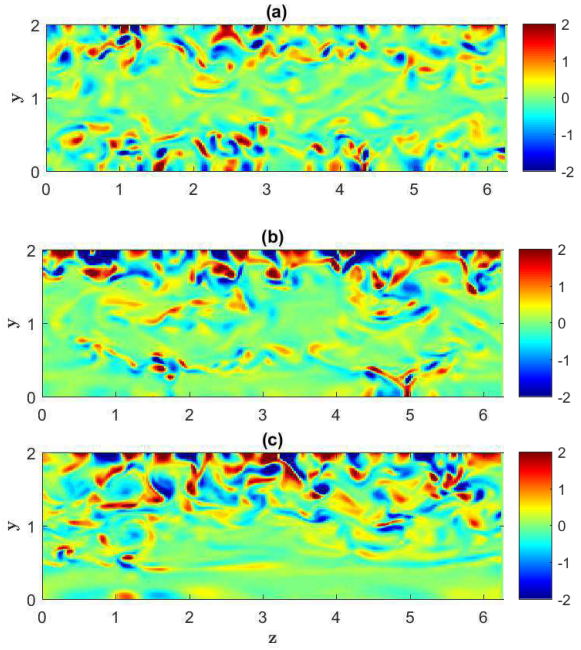

Figure 3.14: Instantaneous $\omega_x^{'}$ map for a y-z section at $x = 2\pi$. a) Case A ($Ro_b = 0$); b) case B ($Ro_b = 0.2$); c) case C ($Ro_b = 0.5$).

field in figure 3.15(b) demonstrates a significant reduction in the number of $\omega_y^{'}$ structures near the suction wall. The re-laminarization of the suction region also results in characteristics of reverse transition such as dense pockets of vortical structures known as "turbulent spots" to be observed (Biringen and Maestrello, 1984, Chambers and Thomas, 1983). The turbulent spots appear intermittently and demonstrate an inclination to the streamwise (x) direction between 15° and 30°, which corresponds with the 30° inclination observed in the transitional flow study by Biringen and Maestrello (1984). For case C ($Ro_b = 0.5$) in figure 3.15(c), the intermittent $\omega_y^{'}$ structures appear even less frequently compared to case B due to further increased re-laminarization of the suction region.

In figure 3.16, maps of fluctuating spanwise vorticity $\omega_z^{'}$ are shown at x-y sections for simulation cases A-C. For case A ($Ro_b = 0$) in figure 3.16(a), spanwise vorticity is observed to be densely concentrated at both channel walls. For cases B ($Ro_b = 0.2$) and C ($Ro_b = 0.5$) in figures 3.16(b) and (c), respectively, the strength of $\omega_z^{'}$ is augmented at the pressure wall ($y = 2$). Near the suction wall ($y = 0$), large-scale vortical structures known as high shear layers are detached

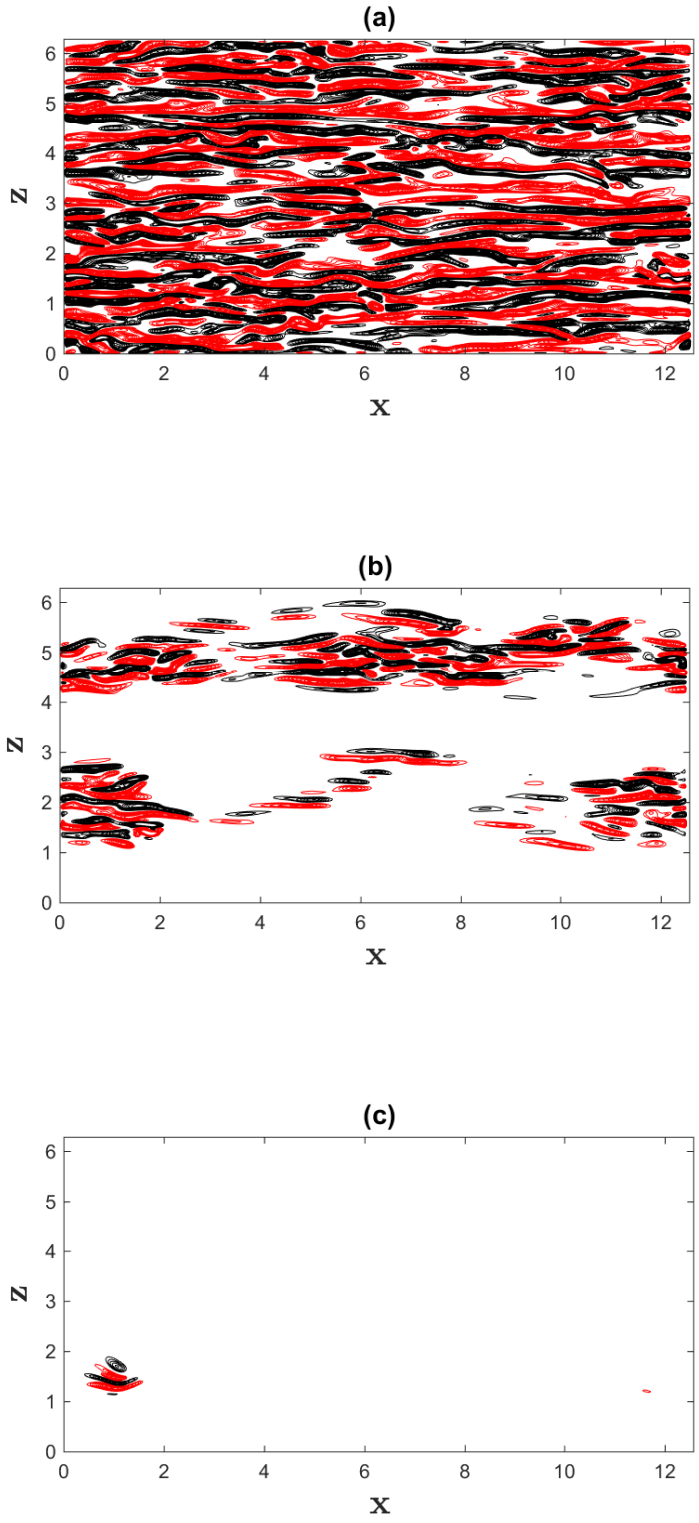

Figure 3.15: Instantaneous $\omega_y^{'}$ map for a x-z section of the near-wall region at $y = 0.06$. Figure displays whole computational box. a) Case A ($Ro_b = 0$); b) Case B ($Ro_b = 0.2$); c) Case C ($Ro_b = 0.5$). Isoline increment = 0.1; black lines: $\omega_y^{'} \leq -0.3$; red lines: $\omega_y^{'} \geq 0.3$.

from the wall in the rotational cases. The wrinkling of the high shear layers is a fundamental characteristic of transition and this feature is highlighted in a smaller x-y cross-section for case B in figure 3.17 (Biringen, 1987). The concave distortion of the high shear layer at $x = 9$ is the result of a secondary instability below the shear layer.

System rotation also generates rotation-induced structures in the pressure region in the form of a spanwise array of longitudinal roll cells, known as Taylor-Gortler vortices (Kristofferson and Andersson, 1993). Time-averaged spanwise and wall-normal velocity vectors from case C ($Ro_b = 0.5$) are shown for a y-z crossflow section at $x = 2\pi$ in figure 3.18(a). These large-scale structures arise from the secondary mean flow advected by the Coriolis force and are responsible for flow circulation throughout the pressure region. The corresponding secondary flow streamlines are shown in figure 3.18(b) and two full pairs of counter-rotating vortices are observed.

The three-dimensional structure of the Taylor-Gortler vortices is shown across the entire channel in figure 3.19 using contours of time-averaged spanwise and wall-normal velocity from case C ($Ro_b = 0.5$). The roll cells appear as streamwise-elongated cylindrical structures which persist throughout the pressure region of the channel. The study by Kristofferson and Andersson (1993) showed the number of roll cell pairs increased with increasing rotation number although the wall-normal length of the circulation region is reduced from progressive re-laminarization.

Of the four coherent structures visualized in this section: sublayer streaks, turbulent spots, high shear layers and Taylor-Gortler vortices, the Taylor-Gortler vortices are considered to be of most interest for MFU design. As a capable MFU model must accurately capture turbulence quantities, it is reasonable to assume that the roll cell arrays which dominate the highly turbulent pressure region also possess a large contribution to turbulence production. Hence these structures are chosen for further investigation. In a later section, a baseline MFU model for rotational turbulence is chosen with $L_z = \pi\delta$ such that one full pair of roll cells is captured and the effect of further spanwise domain length reduction on the Taylor-Gortler vortices is examined.

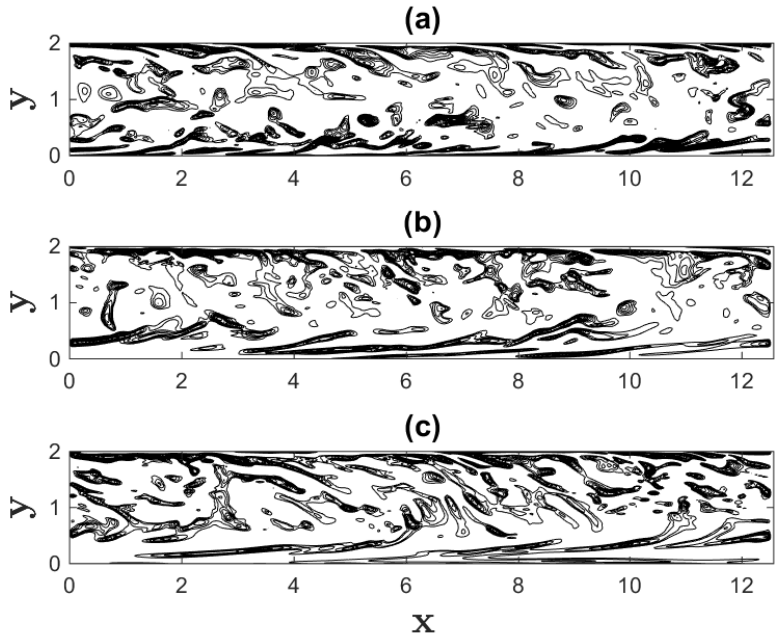

Figure 3.16: Instantaneous $\omega_z^{'}$ map for a x-y section at $z = \pi$. Figure displays whole computational box. a) Case A ($Ro_b = 0$); b) Case B ($Ro_b = 0.2$); c) Case C ($Ro_b = 0.5$). Isoline increment = 0.1; lines: $\omega_z \leq -0.1$.

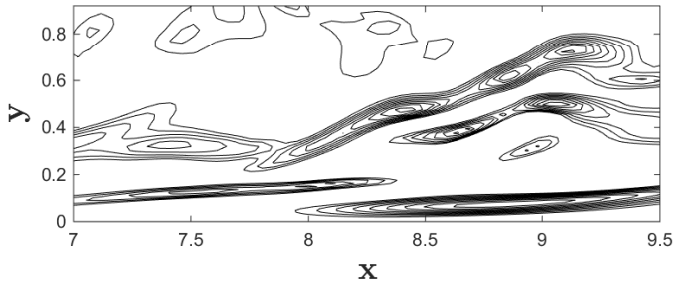

Figure 3.17: Instantaneous $\omega_z^{'}$ map for a x-y section at $z = \pi$ for case B ($Ro_b = 0.2$). Figure shows a reduced cross section in the suction region between $0 \leq y \leq 0.92$ and $7 \leq x \leq 9.5$. Isoline increment = 0.1; lines: $\omega_z \leq -0.1$.

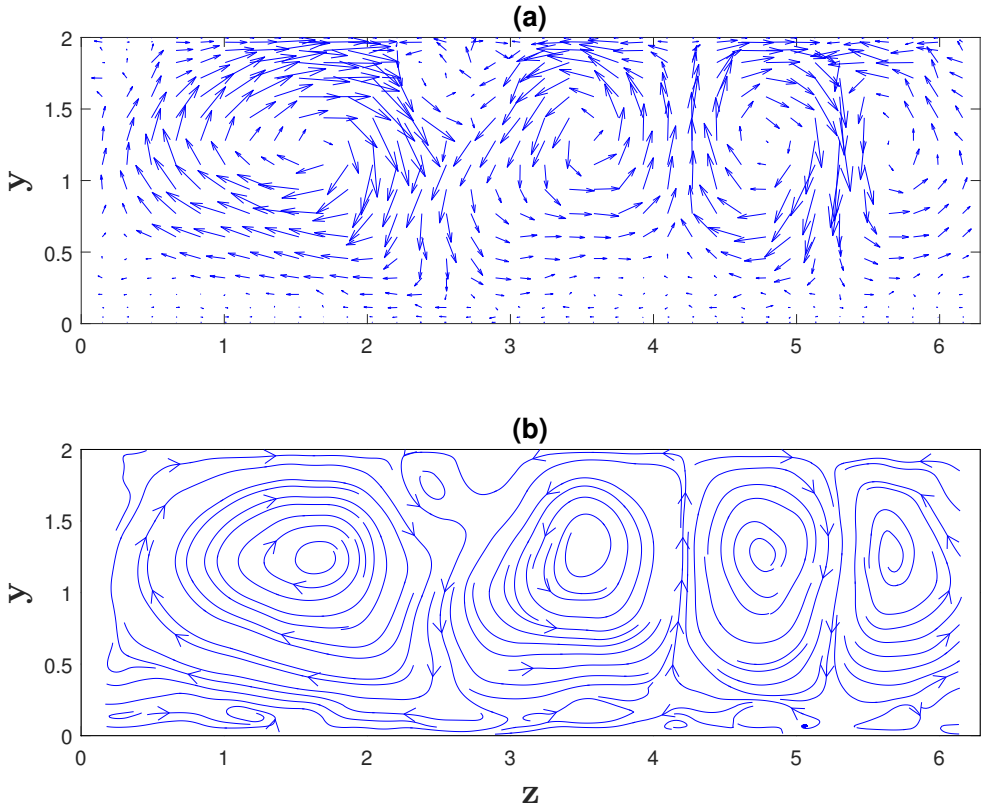

Figure 3.18: (a) Time-averaged v and w velocity vectors for a y-z section at $x = 2\pi$ for case C ($Ro_b = 0.5$). (b) Secondary flow streamlines in the y-z section. Arrows denote the direction of motion.

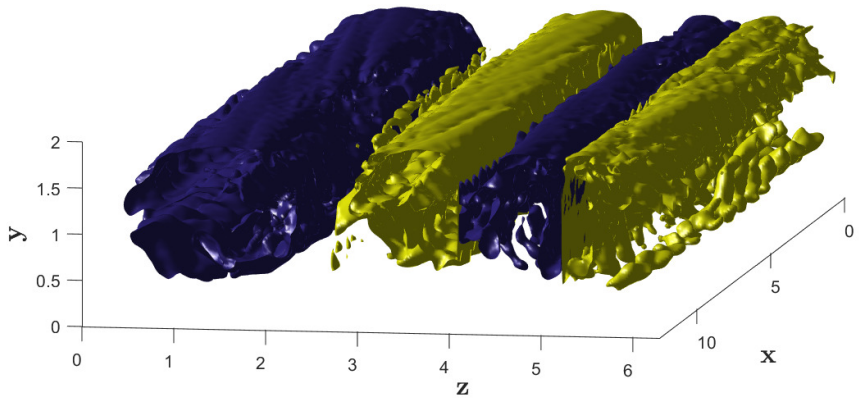

Figure 3.19: Three-dimensional contours of time-averaged v and w velocity for case C ($Ro_b = 0.5$). Blue and yellow contours denote clockwise and counter-clockwise motion, respectively.

3.2.3 Quadrant Analysis

Quadrant analysis of the Reynolds shear stress, which divides $\overline{u'v'}$ into four quadrants according to the signs of fluctuating streamwise (u') and wall-normal (v') velocity where $v' > 0$ signifies motion away from the wall, provides important information on contributions to TKE production (Kline et al., 1967). In equation 3.15, the Reynolds shear stress is shown to have a significant contribution towards the production (P) term. For non-rotating flow, the second and fourth quadrant events dominate the near-wall region of peak TKE production amd at the location of peak production ($y^+ \approx 12$), the contributions from both events are approximately equal (Kim et al., 1971). The second quadrant event, $(\overline{u'v'})_2$ ($u' < 0$ and $v' > 0$), contains the motion attributed with ejections of low-speed fluid away from the wall. The fourth quadrant event, $(\overline{u'v'})_4$ ($u' > 0$ and $v' < 0$), contains the motion attributed to an inrush of high-speed fluid into the wall region. In the present work, quadrant analysis is used to compare cases A ($Ro_b = 0$) and B ($Ro_b = 0.2$) in regards to the relationship between u' and v' whose outer product forms the dominant contribution towards the near-wall P peaks observed in figures 3.13(b).

For simulation case A ($Ro_b = 0$), figure 3.20 shows maps of significant quadrant events in an x-z cross-section at $y = 0.06$, the location of peak production in figure 3.13(b). The bursting event criterion recommended by Comte-Bellot, Sabot, and Saleh (1978)

$$\frac{|u'v'|}{u_{rms}v_{rms}} \geq H \tag{3.18}$$

was used to define significant quadrant events, where H is the threshold level. This H value was set to 1 in the present work and chosen to be similar to the selected threshold values in the bursting event studies by Kim and Spalart (1987) and Bogard and Tiederman (1986). A significantly larger number of powerful second (Q2) and fourth (Q4) quadrant events are observed in comparison to the small number of powerful first (Q1) and third (Q3) quadrant events; the number of significant Q2 and Q4 events is also approximately equal. In figure 3.20(b), the streamwise-elongated structures correspond with the sublayer streaks of the turbulence generation cycle.

Figure 3.21 shows the spatial x-z distributions of significant quadrant events for simulation

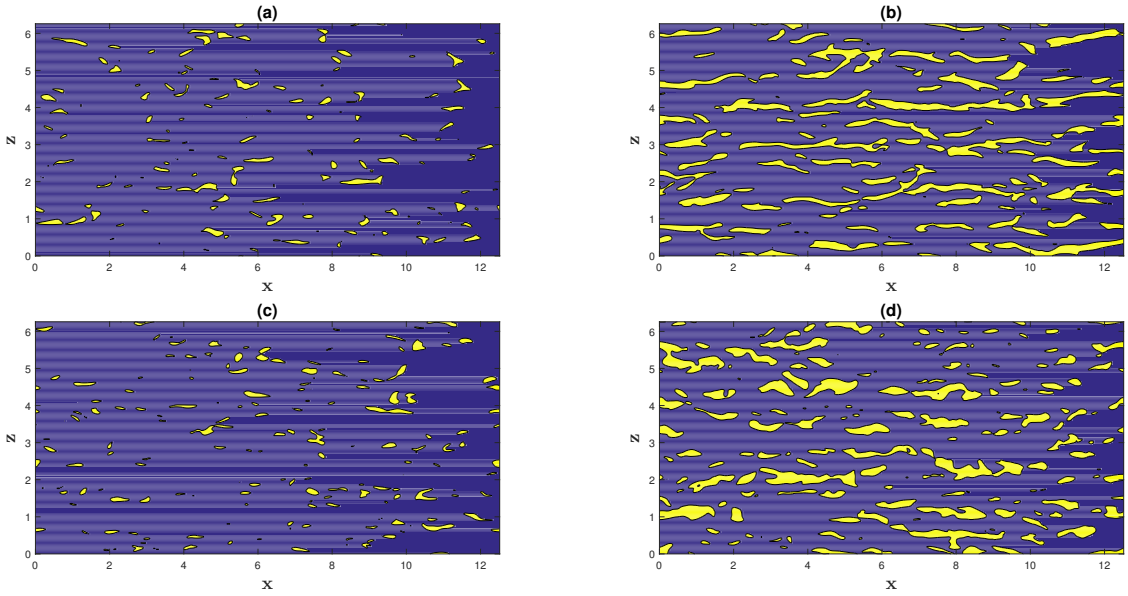

Figure 3.20: Instantaneous spatial distribution of significant quadrant events in a x-z plane at $y = 0.06$ for simulation case A ($Ro_b = 0$): a) First quadrant; b) second quadrant; c) third quadrant; d) fourth quadrant.

case B ($Ro_b = 0.2$) at $y = 0.14$, the corresponding location of peak production in figure 3.13(b). The number of regions with significant Q2 and Q4 activity is significantly diminished compared to case A ($Ro_b = 0$) in figure 3.20. In figures 3.21(b) and (d), structures resembling "turbulent spots" (Biringen and Maestrello, 1984), a characteristical structure of transitional turbulence, are observed. These structures affirm the undergoing process of reverse transition in the suction region as rotational forces drive the flow regime from turbulence towards re-laminarization.

The spatially-averaged (in x and z) quadrant contributions are also shown in figures 3.22(a) and (b) as a function of nondimensional time (t) for cases A ($Ro_b = 0$) and B ($Ro_b = 0.2$), respectively. In figure 3.22(a), the temporal variations are shown to be random and small for case A ($Ro_b = 0$), indicative of the consistent cycle of turbulence production in the near-wall region of turbulent channel flow. Figure 3.22(a) also quantifies the significantly higher contributions from Q2 and Q4 to turbulence production than Q1 and Q3. In figure 3.22(b), the time history for case B ($Ro_b = 0.2$) displays significant changes from figure 3.22(a). For all four quadrants, large, quasi-periodic temporal variations of $\overline{u'v'}$ values are observed over long time scales; the motions are also simultaneous. Although the amplitudes are heavily suppressed compared to case A ($Ro_b = 0$), significant bursts of energetical activity are demonstrated at peak values. The differences between the contributions from Q2 and Q4 to those from Q1 and Q3 are also significantly diminished. At peak amplitude, Q4 events are observed to be the largest contributor to turbulence production.

To analyze the phase differences between the streamwise (u') and wall-normal (v') fluctuating velocities for cases A ($Ro_b = 0$) and B ($Ro_b = 0.2$), the temporal distributions of $\overline{u'v'}$ are decomposed using Fourier transforms. The separate u' and v' signals in figures 3.22(a) and (b) are transformed into spectral signals and a dot product is performed between the two signals. The phase component is extracted from the dot product and visualized in the polar plots in figure 3.23. 0° and 180° refer to the signals being completely in-phase and out-of-phase, respectively. In figure 3.23, a massive shift of the phase contours between the simulation cases A ($Ro_b = 0$) and B ($Ro_b = 0.2$) is observed for all quadrants. Hence a remarkable alignment between streamwise and wall-normal fluctuating velocity, which manifests as the two quantities being almost completely

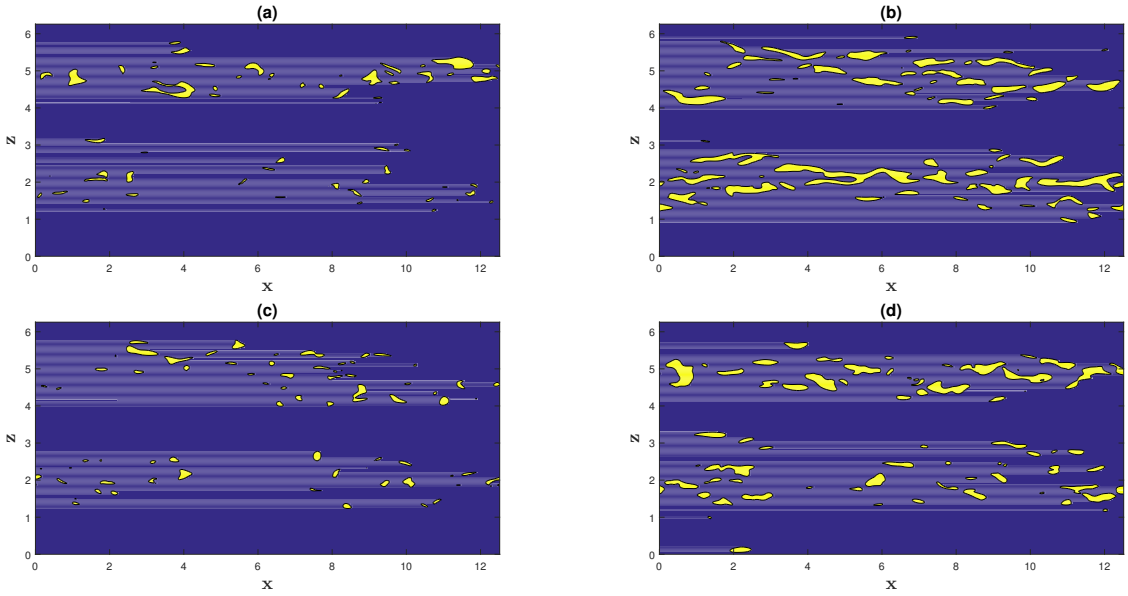

Figure 3.21: Spatial distribution of significant quadrant events in a x-z plane at $y = 0.14$ for simulation case B ($Ro_b = 0.2$): a) First quadrant; b) second quadrant; c) third quadrant; d) fourth quadrant.

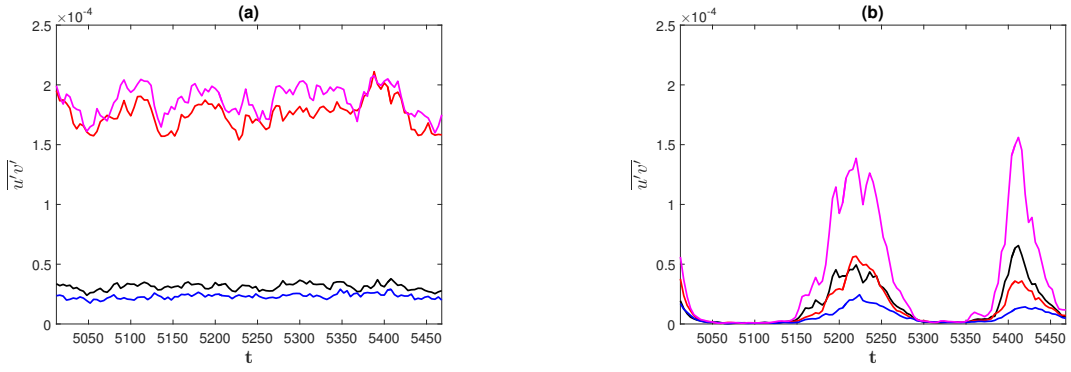

Figure 3.22: Temporal distribution of quadrant events. a) Case A ($Ro_b = 0$); b) case B ($Ro_b = 0.2$). Black: first quadrant (Q1); red: second quadrant (Q2); blue: third quadrant (Q3); magenta: fourth quadrant (Q4).

in-phase or out-of-phase for all four quadrants, is demonstrated in the suction region for case B ($Ro_b = 0.2$). This alignment is also corroborated by the quasi-periodic motions in figure 3.22(b) which occur concurrently for all four quadrants.

3.2.4 Higher-Reynolds number effects

In engineering applications, turbulent flows often encounter higher-Reynolds number effects. Hence it is prudent to investigate how turbulence production and the corresponding turbulence structures are different in higher-Reynolds number flows compared to lower-Reynolds number flows. The higher-Reynolds number simulation case E ($Re_\tau = 406$) is examined and compared to the lower-Reynolds number simulation case B ($Re_\tau = 197$).

In figures 3.24(a) and (b), the mean velocity and temperature distributions are shown for simulation cases B ($Re_\tau = 197$) and E ($Re_\tau = 406$), respectively. In figure 3.24(a), a higher-Reynolds number is shown to significantly decrease the amplitudes of the mean velocity distribution although other distribution characteristics such as the shape and slope in the pressure region are preserved. The decreased amplitudes were expected due to the significant increase of Re_τ (and subsequently u_τ) in simulation case E ($Re_\tau = 406$), which affected the scaling of the distribution. In figure 3.24(b), the mean temperature distribution for case E ($Re_\tau = 406$) is shown to be significantly less asymmetric than the distribution for case B ($Re_\tau = 197$) and resembles the distribution for the no-rotation case A shown in figure 3.8.

In figure 3.25, the turbulent kinetic energy and energy budget (production, pressure-strain and Coriolis) distributions for case B ($Re_\tau = 197$) and case E ($Re_\tau = 406$) are displayed. In figure 3.25(a), case E demonstrates characteristics of higher-Reynolds number flows such as the shifts of both near-wall peaks towards the channel walls and the increasing amplitude of the pressure region peak in the case E ($Re_\tau = 406$) distribution compared to the case B ($Re_\tau = 197$) profile. In figure 3.25(b), the near-wall peak in the pressure region for the case E ($Re_\tau = 406$) distribution also increases in amplitude and shifts towards the channel wall compared to the case B ($Re_\tau = 197$) profile.

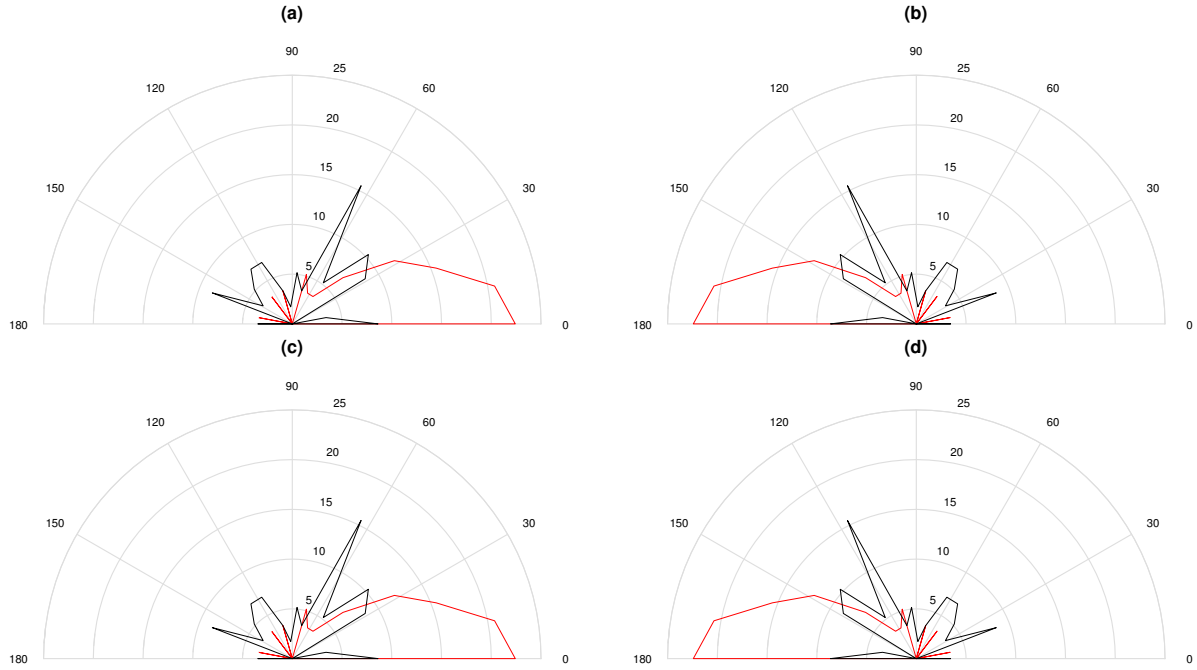

Figure 3.23: Polar plots displaying the respective phase differences between u' and v'. a) First quadrant; b) second quadrant; c) third quadrant; d) fourth quadrant. Black: Simulation case A ($Ro_b = 0$); red: simulation case B ($Ro_b = 0.2$).

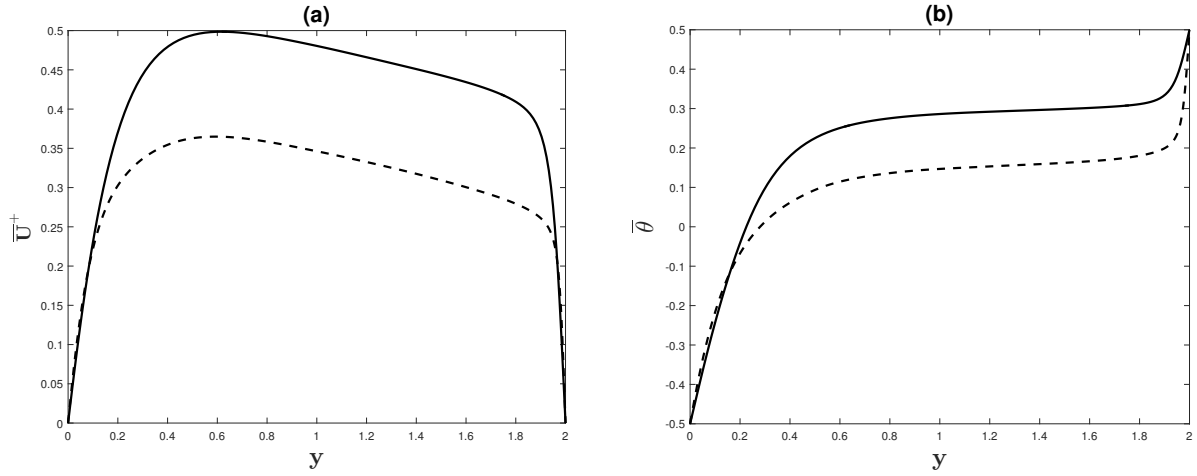

Figure 3.24: Mean velocity and temperature distributions for full simulation cases B and E. a) Mean velocity; b) mean temperature. —: case B ($Re_\tau = 197$); − − −: case E ($Re_\tau = 406$).

In figure 3.25(c), the amplitudes of the pressure-strain distribution for case E are shown to be very similar to that of case B with exception of the region near the pressure wall. Similar to the effects of high-rotation numbers, a higher-Reynolds number increases the amplitude of the pressure-strain budget near the pressure wall significantly. In figure 3.25(d), the near-wall peaks of the Coriolis energy budget distribution are also shown to shift towards the channel walls with a higher Reynolds number, similar to the production budget, although there is less amplitude increase compared to the other energy budget distributions.

It is also imperative to look at how turbulence structures in both the pressure and suction regions are altered by higher-Reynolds number effects. In figure 3.26, x-z planar contours of fluctuating streamwise velocity are shown for simulation cases B ($Re_\tau = 197$) and E ($Re_\tau = 406$) in the region near the suction wall ($y = 0.05$). In figure 3.26(b), the number of powerful fluctuations comprising the "turbulent spots" have increased significantly for simulation case E ($Re_\tau = 406$) and the shape of the overall structure is much more defined.

In figure 3.27, contours of fluctuating streamwise velocity are shown for simulation cases B ($Re_\tau = 197$) and E ($Re_\tau = 406$) in the region near the pressure wall ($y = 1.95$). Similar to figure 3.26(b), figures 3.27(b) demonstrate that higher-Reynolds number effects cause turbulence structures to become smaller and more numerous. Although the overall characterization of the flow field is not changed, the specific characteristics of the turbulence structures is different for high-Reynolds number flows, specifically the diminution and number magnification of the structures.

In figure 3.28, instantaneous x-y maps of fluctuating spanwise vorticity ($\omega_z^{'}$) are shown at $z = \pi$ for simulation cases B ($Re_\tau = 197$) and E ($Re_\tau = 406$). In the regions near both channel walls, the overall turbulence structure is preserved: although the number of structures has increased, elongated slanted structures and clusters of high vorticity concentrations are seen near the suction and pressure walls, respectively. In the center of the channel however, vorticity has clearly increased in the case of simulation case E ($Re_\tau = 406$) perhaps resulting from the alterations to the flow dynamics near both channel walls.

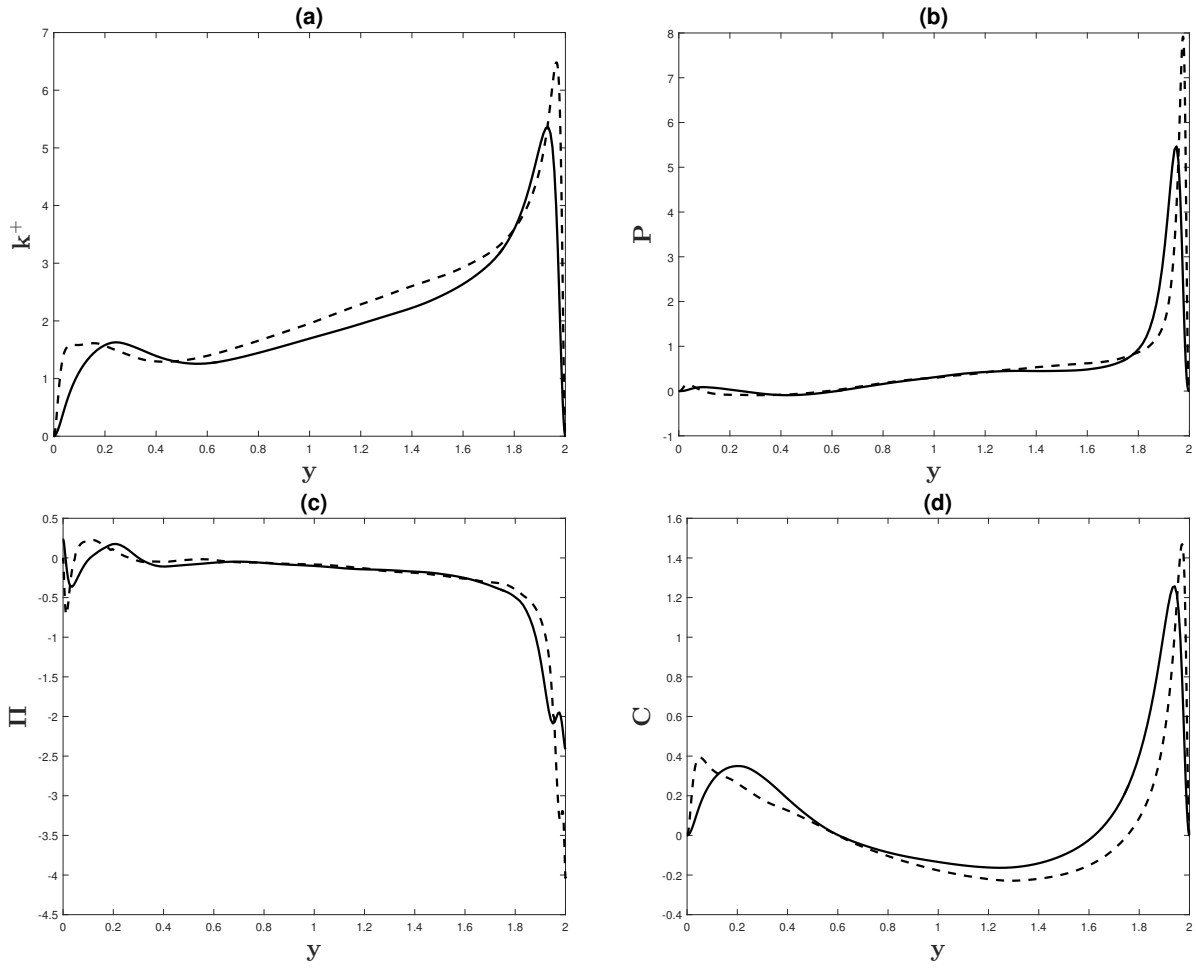

Figure 3.25: Turbulent kinetic energy and energy budgets for full simulation cases B and E. a) Turbulent kinetic energy; b) Production budget; c) Pressure-strain budget; d) Coriolis budget. —: case B ($Re_\tau = 197$); $- - -$: case E ($Re_\tau = 406$).

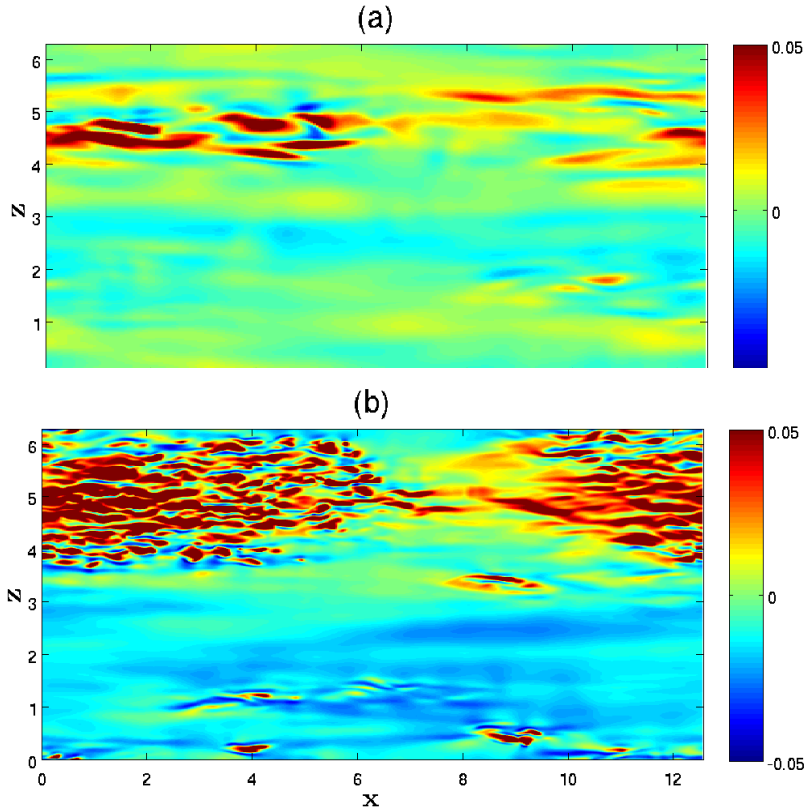

Figure 3.26: Instantaneous $u^{'}$ map for a x-z section of the near-wall region at $y = 0.05$. a) Case B ($Re_\tau = 197$); b) Case E ($Re_\tau = 406$).

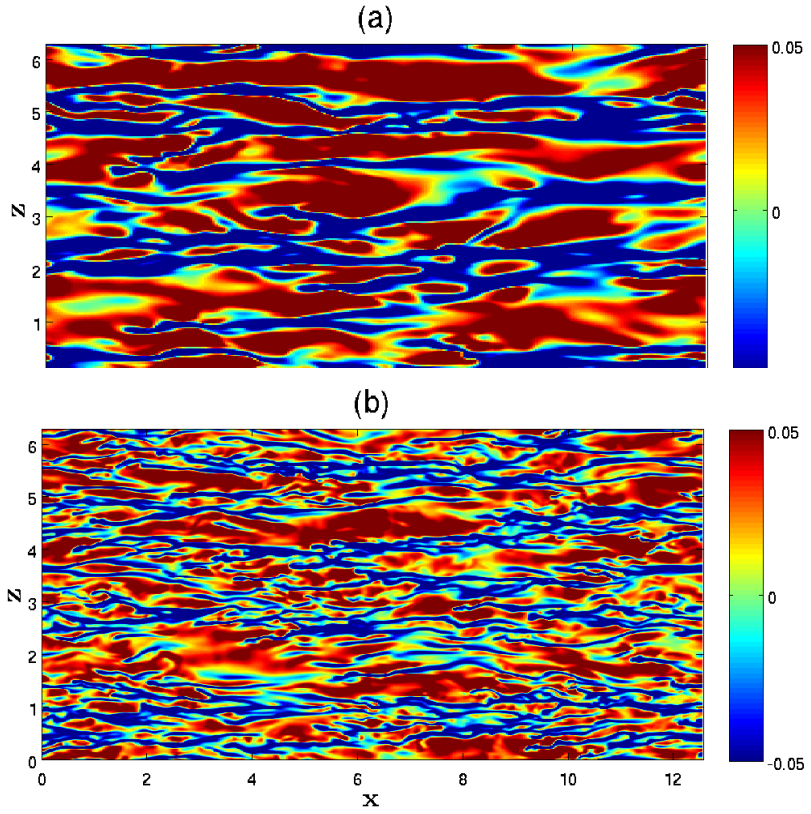

Figure 3.27: Instantaneous $u^{'}$ map for a x-z section of the near-wall region at $y = 1.95$. a) Case B ($Re_\tau = 197$); b) Case E ($Re_\tau = 406$).

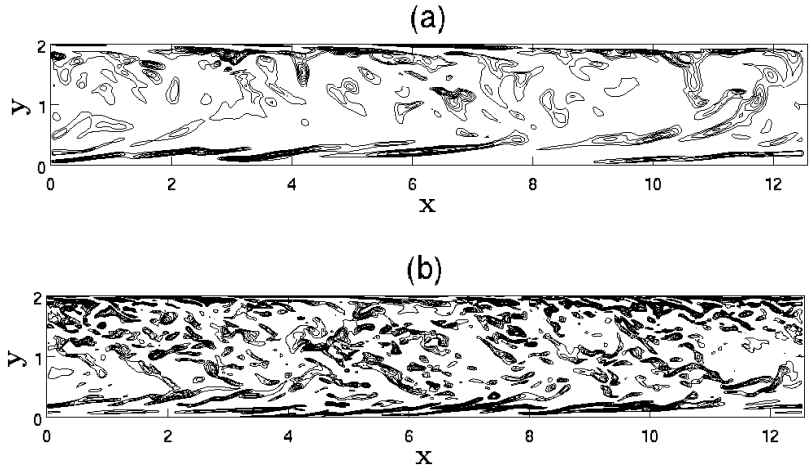

Figure 3.28: Instantaneous $\omega_z^{'}$ map for a x-y section at $z = \pi$. a) Case B ($Re_\tau = 197$); b) Case E ($Re_\tau = 406$). Isoline increment = 0.1; lines: $\omega_z \leq -0.1$.

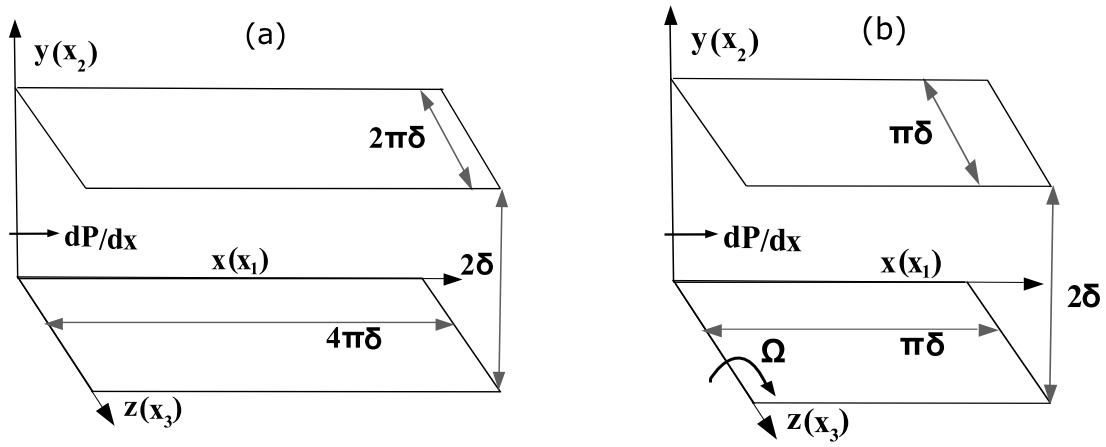

Figure 3.29: Geometry of DNS computational domain for a) full simulations; b) baseline MFU simulations

3.2.5 Minimal Flow Unit

3.2.5.1 Simulation Overview

The direct numerical simulations for the design of the minimal flow unit (MFU) model were computed using the same numerical methods and parameters outlined previously. Additional MFU-specific information regarding the simulations is provided below.

The flow geometries of the present DNS for the full and baseline MFU simulations are shown in figures 3.29(a) and 3.29(b), respectively; all simulations are based on the periodic channel model. Initial MFU fields were generated by data extraction from the steady-state solutions of the full simulations and interpolation onto MFU grids. The listing of simulations and their corresponding domain lengths and grid resolutions are found in the case descriptions (table 3.3). The streamwise length of all MFU simulations was selected as $L_x = \pi\delta$ as examinations of box domains with $L_x = 2\pi\delta$ and $\pi\delta$ showed that a streamwise length of $\pi\delta$ generally approximated the length of sublayer streaks in the near-wall region. This characteristic streak length did not change within the pressure region in the case of spanwise rotation and is also equivalent to the MFU model proposed by Jimenez and Moin (1991) for the non-rotating channel. The MFU simulations $AM1$ and $CM1$ were used to study MFU accuracy for higher-order statistics at the baseline

MFU spanwise domain length $L_z = \pi\delta$. The MFU models denoted $M1$-$M4$ for simulation cases B, C and E gradually reduced the spanwise domain length to $L_z = 0.18\pi\delta$ to study box minimization in that direction and its effect on the accuracy of turbulence statistics.

3.2.5.2 MFU: Spanwise Box Minimization

This section proceeds with the determination of an MFU model for rotational turbulence. In the box minimization study by Jimenez and Moin (1991) for non-rotating turbulent channel flow, the critical spanwise domain length for self-sustaining turbulence was found to be approximately $\lambda_z^+ = 100$. This spanwise wall unit length is in good agreement with the accepted mean value for sublayer streak spacing in the near-wall region, indicating these structures require correct characterization for accurate turbulence statistics (Smith and Metzler, 1983). When turbulent channel flow is subject to spanwise rotation, these sublayer streaks persist in the pressure region. The mean spacing between these structures is calculated for full simulation cases A-C in order to determine if system rotation causes fundamental changes to the structural organization of these sublayer streaks.

In the present work, the mean streak spacing is determined using the spanwise burst distance which is the mean spanwise spacing between bursting events. The bursting event criteria recommended by Comte-Bellot, Sabot, and Saleh (1978)

$$\frac{|u'v'|}{u_{rms}v_{rms}} \geq H \tag{3.19}$$

was used where H is the threshold level which was set to 1 in the present work, as in Kim and Spalart (1987) and Bogard and Tiederman (1986). The latter study also reported the average burst distance was independent of the threshold value over the range $H = 0.25$ to 1.25. In the present work, bursting events were detected at the wall-normal locations $y = 0.06$ for case A ($Ro_b = 0$) and $y = 1.95$ for rotational cases B ($Ro_b = 0.2$) and C ($Ro_b = 0.5$), which corresponded with the location of peak turbulent kinetic energy production for the simulations. A procedure similar to Kim and Spalart (1987) was performed to calculate the bursting distance. Instantaneous fields were checked

Table 3.3: MFU case descriptions and initial conditions.

Case	Re_τ	Ro_b	*Type*	$L_x \times L_y \times L_z$	$nx \times ny \times nz$
A	200	0	Full	$4\pi\delta \times 2\delta \times 2\pi\delta$	$256 \times 129 \times 256$
B	197	0.2	Full	$4\pi\delta \times 2\delta \times 2\pi\delta$	$256 \times 129 \times 256$
C	192	0.5	Full	$4\pi\delta \times 2\delta \times 2\pi\delta$	$256 \times 129 \times 256$
E	406	0.2	Full	$4\pi\delta \times 2\delta \times 2\pi\delta$	$512 \times 513 \times 512$
$AM1$	196	0	MFU	$\pi\delta \times 2\delta \times \pi\delta$	$64 \times 97 \times 96$
$BM1$	188	0.2	MFU	$\pi\delta \times 2\delta \times \pi\delta$	$64 \times 97 \times 96$
$BM2$	191	0.2	MFU	$\pi\delta \times 2\delta \times 0.36\pi\delta$	$64 \times 97 \times 32$
$BM3$	196	0.2	MFU	$\pi\delta \times 2\delta \times 0.24\pi\delta$	$64 \times 97 \times 24$
$BM4$	194	0.2	MFU	$\pi\delta \times 2\delta \times 0.18\pi\delta$	$64 \times 97 \times 16$
$CM1$	190	0.5	MFU	$\pi\delta \times 2\delta \times \pi\delta$	$64 \times 97 \times 96$
$CM2$	192	0.5	MFU	$\pi\delta \times 2\delta \times 0.36\pi\delta$	$64 \times 97 \times 32$
$CM3$	193	0.5	MFU	$\pi\delta \times 2\delta \times 0.24\pi\delta$	$64 \times 97 \times 24$
$CM4$	194	0.5	MFU	$\pi\delta \times 2\delta \times 0.18\pi\delta$	$64 \times 97 \times 16$
$EM1$	390	0.2	MFU	$\pi\delta \times 2\delta \times \pi\delta$	$128 \times 97 \times 192$
$EM2$	385	0.2	MFU	$\pi\delta \times 2\delta \times 0.36\pi\delta$	$128 \times 97 \times 64$
$EM3$	387	0.2	MFU	$\pi\delta \times 2\delta \times 0.24\pi\delta$	$128 \times 97 \times 48$
$EM4$	382	0.2	MFU	$\pi\delta \times 2\delta \times 0.18\pi\delta$	$128 \times 97 \times 32$

Table 3.4: Comparison of mean streak spacing in the peak TKE production planes for full simulation cases *A*-*C* using inner (λ_z^+) and outer (λ_z/δ) variable scaling. Inner scaling is shown using both global ($\lambda_{zg}^+ = zu_\tau/\nu$) and local ($\lambda_{zl}^+ = zu_{\tau p}/\nu$) friction velocities. The minimum spanwise lengths proposed by Jimenez and Moin (1991) for no rotation are provided for comparison.

Case	Re_τ	Ro_b	λ_z/δ	λ_{zg}^+	λ_{zl}^+
Jimenez (1991)	200	0	0.5655	113	113
A	200	0	0.5950	119	119
B	197	0.2	0.5694	112	134
C	192	0.5	0.5333	103	125

at every grid point for the satisfaction of equation 3.19 and points which satisfied the criteria were defined as bursts. The distances between these bursts were calculated and averaged in the streamwise (x) direction. In addition, more than 100 groups were examined for each simulation case to provide an adequate statistical sample.

In table 3.4, the mean spanwise streak spacing (λ_z) is shown for the three full simulation cases along with the critical spanwise domain length proposed by Jimenez and Moin (1991). The results are shown under three different scalings: outer variable scaling (λ_z/δ), inner global variable scaling ($\lambda_{zg}^+ = zu_\tau/\nu$) and inner local variable scaling ($\lambda_{zl}^+ = zu_{\tau p}/\nu$) where $u_{\tau p}$ denotes the local friction velocity on the pressure wall. For no rotation, $u_{\tau p}$ is equivalent to the global friction velocity u_τ.

From case *A* ($Ro_b = 0$) to *C* ($Ro_b = 0.5$), table 3.4 demonstrates a decrease in the mean streak spacing for λ_z/δ and λ_{zg}^+. The inner local variable scale λ_{zl}^+ is shown to increase from case *A* to *C* due to a significantly larger value of $u_{\tau p}$. The study by Kristofferson and Andersson (1993) similarly showed a decrease in λ_z as the rotation number increased. However, their reported decline of λ_z was more significant and offsetting the increase of $u_{\tau p}$ at all rotation rates. This resulted in a constant reduction of λ_{zl}^+ with higher rotation number and a value of $\lambda_{zl}^+ = 60$ for $Ro_b = 0.5$. There are various estimates for sublayer streak spacing in the pressure region of rotating turbulent channel flow. The large-eddy simulation (LES) study of Miyake and Kajishima (1986) reported λ_z remained constant up to a rotation number of $Ro_b = 0.165$ which implied λ_{zl}^+ increased with rota-

tion number due to rising values of $u_{\tau p}$. For the purposes of present MFU design, sublayer streak spacing for cases B and C was determined to be generally similar to the no-rotation case A as both λ_{zl}^{+} and λ_{zg}^{+} remain near the critical value of $\lambda_{z}^{+} = 100$ reported by Jimenez and Moin (1991).

3.2.5.3 MFU accuracy and roll cells

A box minimization study was first conducted using four models with varying spanwise domain lengths for $Ro_b = 0.5$. The MFU simulation cases $CM1$, $CM2$, $CM3$ and $CM4$ correspond to spanwise domain lengths of $L_z = \pi\delta$, $0.36\pi\delta$, $0.24\pi\delta$ and $0.18\pi\delta$, respectively. The largest spanwise length $L_z = \pi\delta$ was selected to capture one full pair of Taylor-Gortler vortices visualized in the previous section and the smallest length $L_z = 0.18\pi\delta$ was chosen to match the critical length proposed by Jimenez and Moin (1991) for non-rotating turbulent channel flow. In figure 3.30, mean streamwise velocity distributions for $Ro_b = 0.5$ demonstrate the MFU model becomes less accurate with decreasing spanwise domain length. All four models correctly characterize the laminar-like (parabolic) profile of the suction region and the constant gradient profile of the pressure region. However, cases $CM3$ ($L_z = 0.24\pi\delta$) and $CM4$ ($L_z = 0.18\pi\delta$) reveal an inaccurate slope in the pressure region.

Although simulation cases $CM3$ and $CM4$ possess spanwise domain lengths equal to or larger than the calculated streak spacing distances in the previous section, significant mean velocity distribution inaccuracies are observed for their respective box dimensions. Hence it is concluded that for rotational turbulence, alternative coherent structures which operate on larger eddies than sublayer streaks are primarily responsible for turbulence production and require proper characterization for accurate MFU models. A relation to the large-scale Taylor-Gortler vortices is examined. In figure 3.31, secondary flow streamlines in the y-z crossflow section for each MFU model are shown at $x = 0.5\pi$. Longitudinal roll cells are well-defined in figures 3.31(a) and (b) which correspond to MFU simulation cases $CM1$ ($L_z = \pi\delta$) and $CM2$ ($L_z = 0.36\pi\delta$), respectively. For simulation case $CM3$ ($L_z = 0.24\pi\delta$) in figure 3.31(c), significant discrepancies are observed in the roll cell characteristics. The wall-normal width of the vortices is decreased by approximately

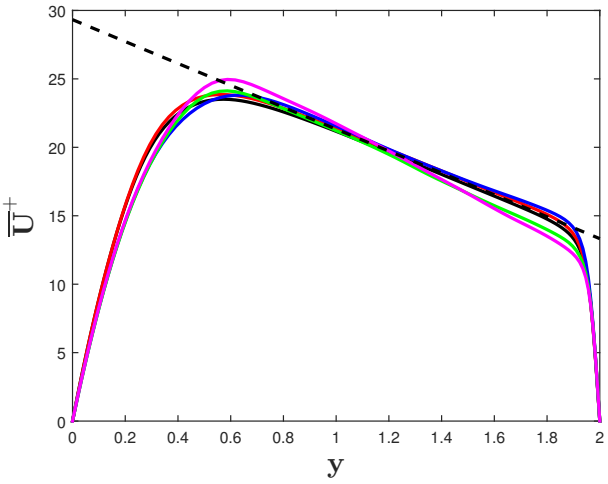

Figure 3.30: Comparison of the mean velocity distributions for $Ro_b = 0.5$. Black: Case C ($L_z = 2\pi\delta$); Red: Case $CM1$ ($L_z = \pi\delta$); Blue: Case $CM2$ ($L_z = 0.36\pi\delta$); Green: Case $CM3$ ($L_z = 0.24\pi\delta$); Magenta: Case $CM4$ ($L_z = 0.18\pi\delta$); $---$: 2Ω line.

50 percent, resulting in a smaller flow circulation region. For simulation case $CM4$ ($L_z = 0.18\pi\delta$) in figure 3.31(d), only a single, thin vortex is observed adjacent to the pressure wall. It is also important to note that in figure 3.31(b) for case $CM2$ ($L_z = 0.36\pi\delta$), the two vortices are not of equal size in the wall-normal y direction as the roll cells in figure 3.18, which indicates some characteristic transformation of the vortices. Hence case $CM1$ ($L_z = \pi\delta$) is the only MFU simulation case to capture at least one full pair of roll cells.

In figure 3.32, a three-dimensional representation of the MFU roll cells for case $CM1$ is shown using contours of time-averaged spanwise and wall-normal velocity. It is demonstrated that the streamwise coherence of the roll cells' tube-like struture is preserved despite the significant reduction of the streamwise domain from $L_x = 4\pi\delta$ in case C (figure 3.19) to $L_x = \pi\delta$.

The normal and shear Reynolds stress distributions for the full and MFU simulations are shown in figure 3.33. Similar to the mean velocity distributions in figure 3.30, increasing inaccuracy is observed for smaller L_z in the distributions of $\overline{u'u'}^+$ and $\overline{w'w'}^+$ in figures 3.33(a) and (c), respectively. The underestimations of the normal Reynolds stresses in case $CM4$ ($L_z = 0.18\pi\delta$) correspond with the absence of a Taylor-Gortler vortex pair in figure 3.31(d). Without the flow circulation advected by these vortices in the pressure region, it is expected that turbulent fluctuations are reduced. The overestimations of peak $\overline{u'u'}^+$ and $\overline{v'v'}^+$ amplitudes in simulation case $CM2$ ($L_z = 0.36\pi\delta$) can be attributed to the reduced size of a vortex in figure 3.31(b) and case $CM1$ ($L_z = \pi\delta$) is the most accurate MFU model for general turbulence statistics. The Reynolds shear stress $\overline{u'v'}^+$ distributions from the MFU simulations are demonstrated to be remarkably accurate for all spanwise domain lengths although only case $CM1$ captures a small range of negative $\overline{u'v'}^+$ amplitudes in the suction region at approximately $y = 0.4$.

For MFU model design, accurate mean velocity distributions are shown to correlate with a longitudinal roll cell pair which is captured in full length. Past a critical value which is marginally less than $L_z = 0.36\pi\delta$, reduction of the spanwise domain length results in the contraction of the Taylor-Gortler vortices in the wall-normal direction, leading to inaccurate mean flow statistics. The relationship between Taylor-Gortler vortices and mean flow is supported by the formation of

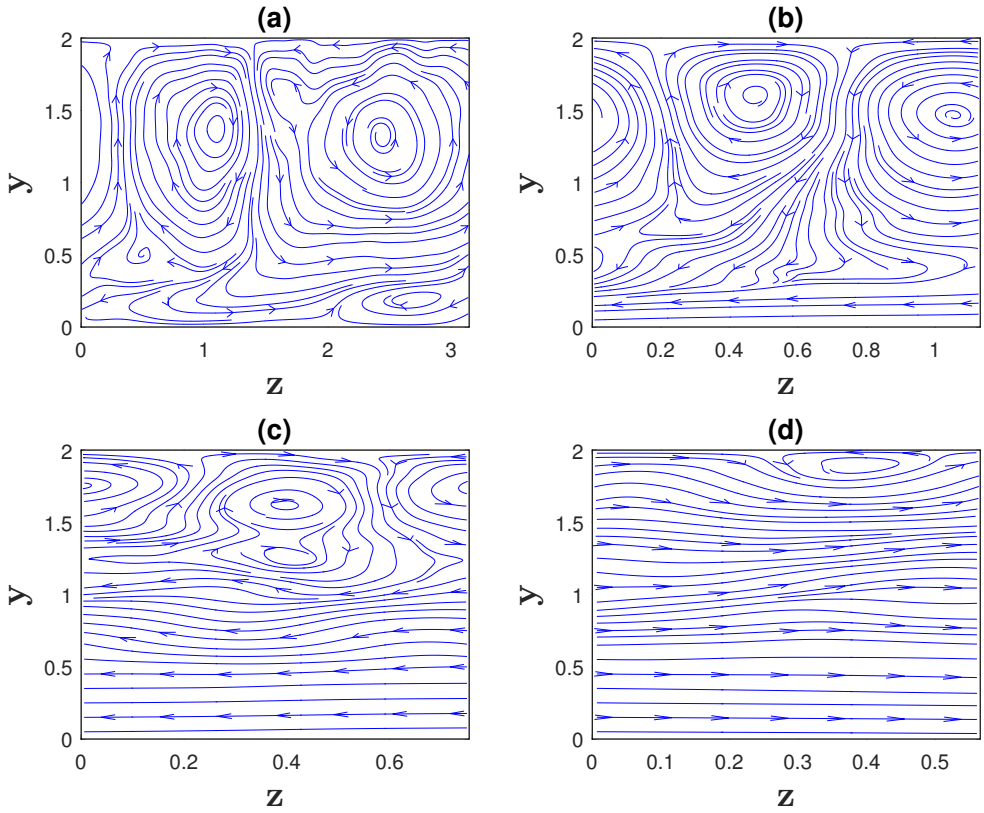

Figure 3.31: MFU secondary flow streamlines in the y-z section at $x = 0.5\pi$ for $Ro_b = 0.5$. Arrows denote the direction of motion. (a) Case $CM1$ ($L_z = \pi\delta$); (b) Case $CM2$ ($L_z = 0.36\pi\delta$); (c) Case $CM3$ ($L_z = 0.24\pi\delta$); (d) Case $CM4$ ($L_z = 0.18\pi\delta$).

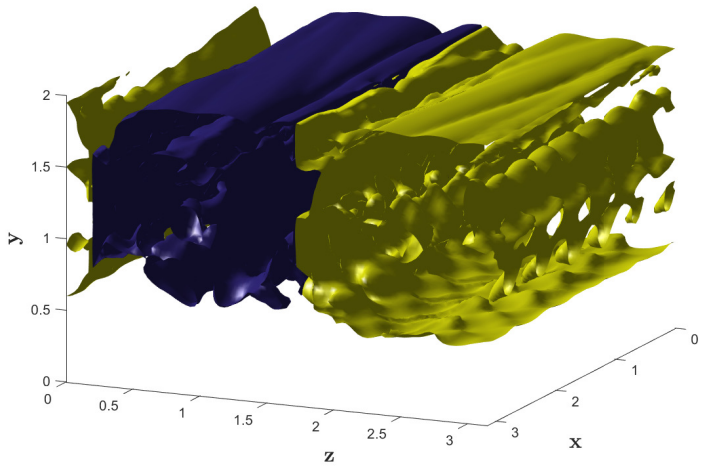

Figure 3.32: Three-dimensional contours of time-averaged v and w velocity for MFU simulation case $CM1$ ($Ro_b = 0.5$). Blue and yellow contours denote clockwise and counter-clockwise motion, respectively.

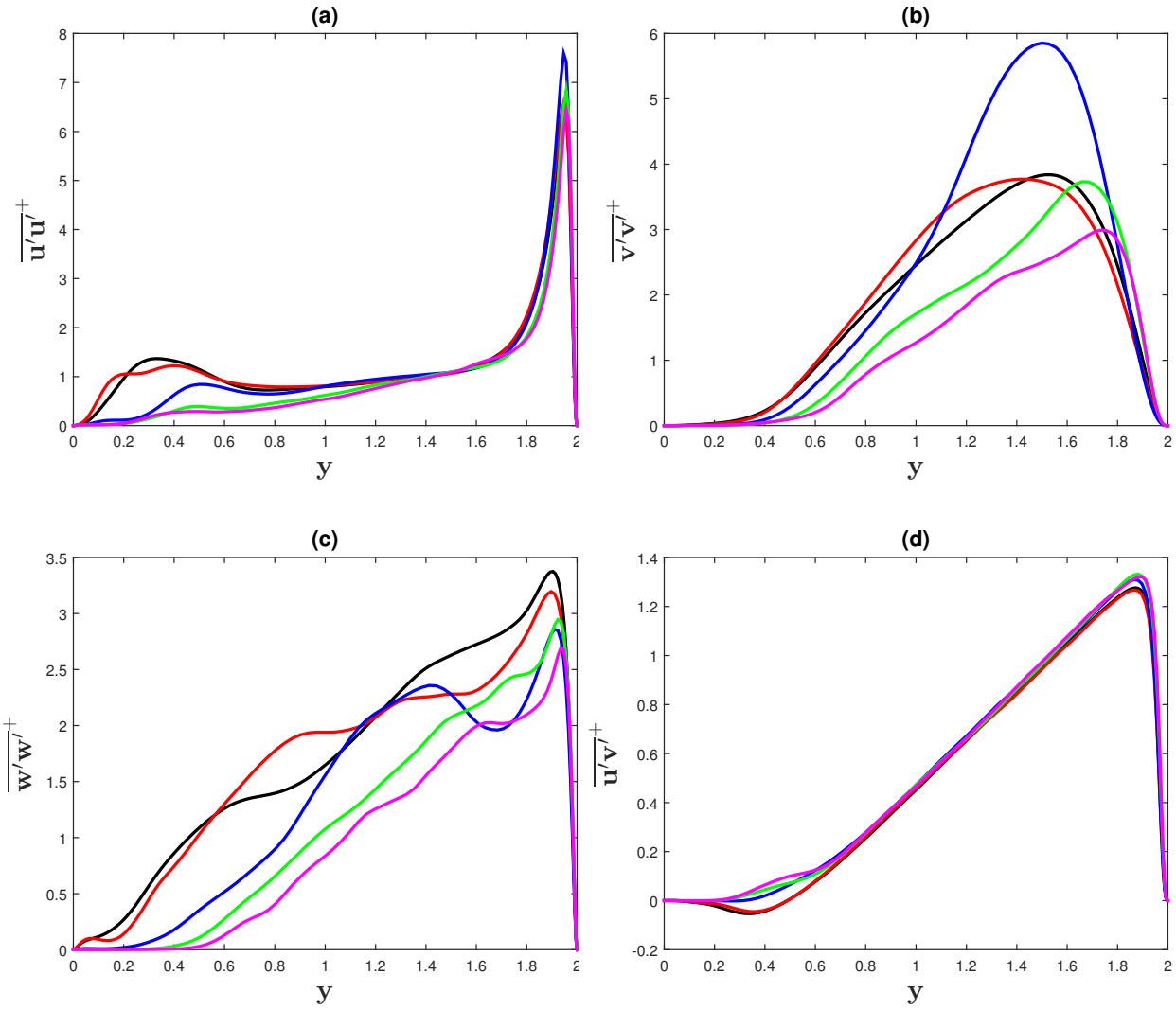

Figure 3.33: Comparison of Reynolds stress distributions for $Ro_b = 0.5$: a) $\overline{u'u'}^+$; b) $\overline{v'v'}^+$; c) $\overline{w'w'}^+$; d) $\overline{u'v'}^+$. Black: Case C ($L_z = 2\pi\delta$); Red: Case $CM1$ ($L_z = \pi\delta$); Blue: Case $CM2$ ($L_z = 0.36\pi\delta$); Green: Case $CM3$ ($L_z = 0.24\pi\delta$); Magenta: Case $CM4$ ($L_z = 0.18\pi\delta$).

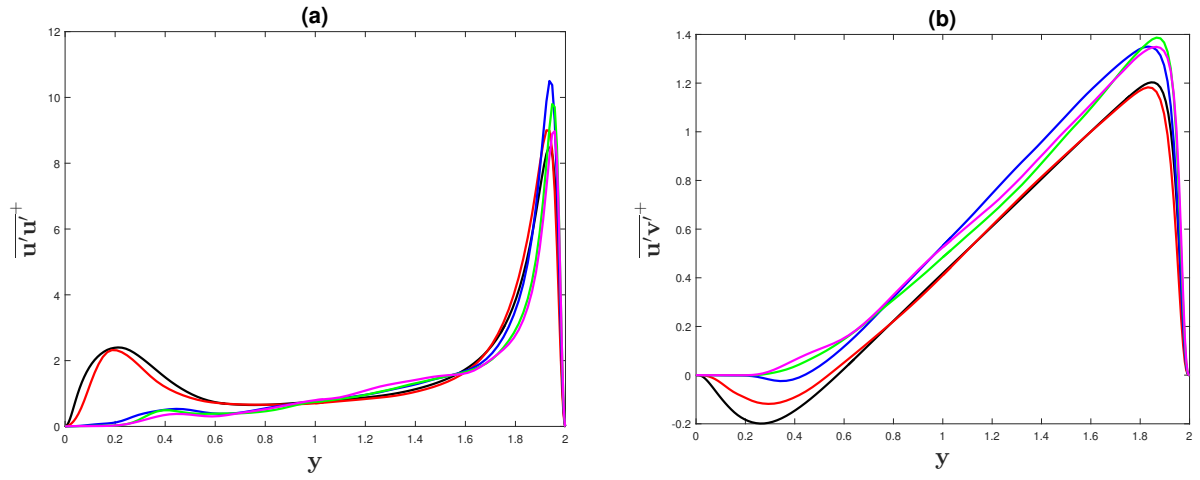

Figure 3.34: Comparison of Reynolds stress distributions for $Ro_b = 0.2$. a) $\overline{u'u'}^+$; b) $\overline{u'v'}^+$. Black: Case B ($L_z = 2\pi\delta$); Red: Case $BM1$ ($L_z = \pi\delta$); Blue: Case $BM2$ ($L_z = 0.36\pi\delta$); Green: Case $BM3$ ($L_z = 0.24\pi\delta$); Magenta: Case $BM4$ ($L_z = 0.18\pi\delta$).

roll cells in the secondary mean (time-averaged) flow advected by the Coriolis force. In addition, the roll cell characteristics are shown to influence the accuracy of the Reynolds stress distributions as well; a single reduced vortex in case $CM2$ resulted in inaccurate distributions of $\overline{u'u'}^+$ and $\overline{v'v'}^+$. Consequently, accurate turbulence statistics with system rotation are not dependent on turbulent sublayer streak spacing as in non-rotating turbulent channel flow, but instead they depend on capturing at least one full pair of large-scale roll cells, necessitating a longer spanwise domain length for a capable MFU model.

MFU results for simulation case B ($Ro_b = 0.2$) were very similar to those for simulation case C ($Ro_b = 0.5$). The streamwise and shear Reynolds stress distributions for the full and MFU simulations are shown in figure 3.34 for $Ro_b = 0.2$. Increasing inaccuracy was observed with decreasing L_z and MFU case $BM1$ ($L_z = \pi\delta$) performed the best for accurately approximating the Reynolds stresses.

3.2.5.4 MFU: Higher-Reynolds Number Effects

Since the focus of MFU model design in the previous section involved turbulence structures in the outer layer of the channel, it is necessary to demontrate clear separation between

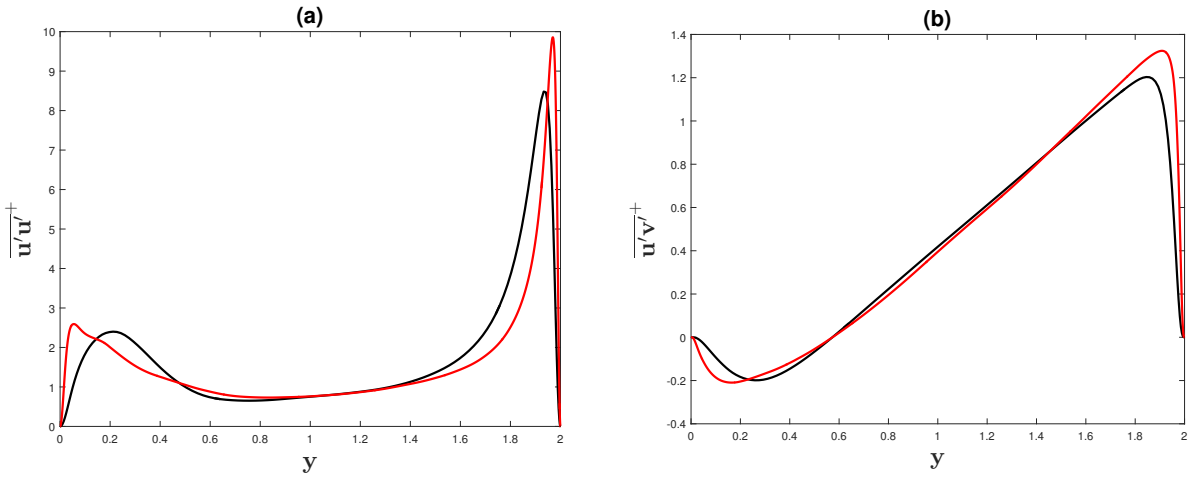

Figure 3.35: Comparison of Reynolds stress distributions for $Ro_b = 0.2$ for a lower and higher-Reynolds number: a) $\overline{u'u'}^+$; b) $\overline{u'v'}^+$. Black: Case B ($Re_\tau = 197$); Red: Case E ($Re_\tau = 406$).

the inner and outer regions of the channel, which occurs at higher-Reynolds number flows, to clarify the application of the proposed MFU model towards rotational flows. In addition, the study by Brethouwer et al. (2013) demonstrated through the examination of oblique turbulent-laminar patterns in the suction region for a wide range of rotation and Reynolds numbers, that Reynolds number effects were significant for spanwise-rotating turbulent channel flow. Hence a higher-Reynolds number simulation case E was performed for rotation number $Ro_b = 0.2$ and a corresponding MFU analysis was conducted such that the results were compared to those from the lower-Reynolds number simulation case B.

First, it is prudent to demonstrate that the lower and higher-Reynolds number simulations possess distinct characteristics in their corresponding turbulence statistics. A comparison of the distributions of the streamwise and shear Reynolds stresses from the low (Case B) and higher (Case E) Reynolds number simulations is shown in figures 3.35(a) and (b), respectively. Characteristics of higher-Reynolds number flows are observed for simulation case E such as the shifts of the near-wall peaks towards the channel walls and the increasing amplitude of the peaks in both case E distributions compared to the case B profiles (Moser et al., 1999).

For the higher-Reynolds number simulation case E, the box minimization study performed

in the previous section for the lower-Reynolds number simulation was also conducted using four MFU models with varying spanwise domain lengths for $Ro_b = 0.2$. Similarly, the MFU simulation cases $EM1$, $EM2$, $EM3$ and $EM4$ correspond to spanwise domain lengths of $L_z = \pi\delta$, $0.36\pi\delta$, $0.24\pi\delta$ and $0.18\pi\delta$, respectively. In figure 3.36, the mean streamwise velocity distributions for the higher-Reynolds number simulation case continued to demonstrate that the MFU model became less accurate with decreasing spanwise domain length. All four MFU simulations captured the laminar-like (parabolic) profile of the suction region. However, there were significant amplitude differences between the four MFU distributions and the full simulation distribution; case $EM4$ ($L_z = 0.18\pi\delta$) also failed to capture the constant gradient profile of the pressure region. Case $EM1$ ($L_z = \pi\delta$) possessed the most accurate approximation of the four MFU models but was inaccurate compared to its corresponding MFU case $BM1$ for a lower-Reynolds number.

The normal and shear Reynolds stress distributions for the full and MFU simulations are shown in figure 3.37 for the higher-Reynolds number case. Similar to the lower-Reynolds number results in figure 3.33(a), increasing inaccuracy was observed with decreasing L_z in the distribution of $\overline{u'u'}^+$ in figure 3.37(a). In figures 3.37(b) and (c), there was little correlation with L_z and MFU model accuracy for the distributions of $\overline{v'v'}^+$ and $\overline{w'w'}^+$, respectively. As with the lower-Reynolds number simulations, the domain box with $L_z = \pi\delta$ (Case $EM1$) was the most accurate MFU model for general turbulence statistics. However, the MFU model performed more poorly for the higher-Reynolds number simulation than the lower-Reynolds simulation. For example, the Reynolds shear stress $\overline{u'v'}^+$ distribution in figure 3.37(d) for case $EM1$ was significantly less accurate than the corresponding distribution for case $CM1$ in figure 3.33(d). This loss of accuracy with increasing Reynolds number concurs with the study by Lozano-Duran and Jimenez (2014), which demonstrated that a larger domain size at very large Reynolds numbers ($Re_\tau \approx 4200$) was required to calculate accurate one-point turbulence statistics compared to the lower-Reynolds number MFU domain proposed by Jimenez and Moin (1991).

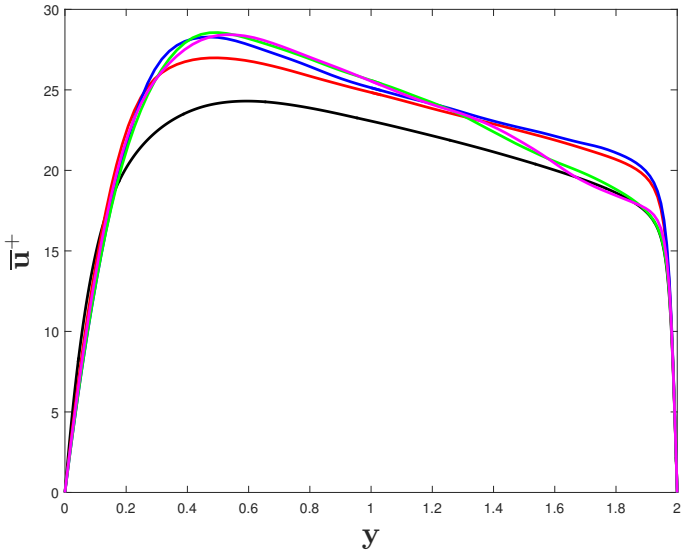

Figure 3.36: Comparison of the MFU mean velocity distributions for $Ro_b = 0.2$ at a higher-Reynolds number. Black: Case E ($L_z = 2\pi\delta$); Red: Case $EM1$ ($L_z = \pi\delta$); Blue: Case $EM2$ ($L_z = 0.36\pi\delta$); Green: Case $EM3$ ($L_z = 0.24\pi\delta$); Magenta: Case $EM4$ ($L_z = 0.18\pi\delta$).

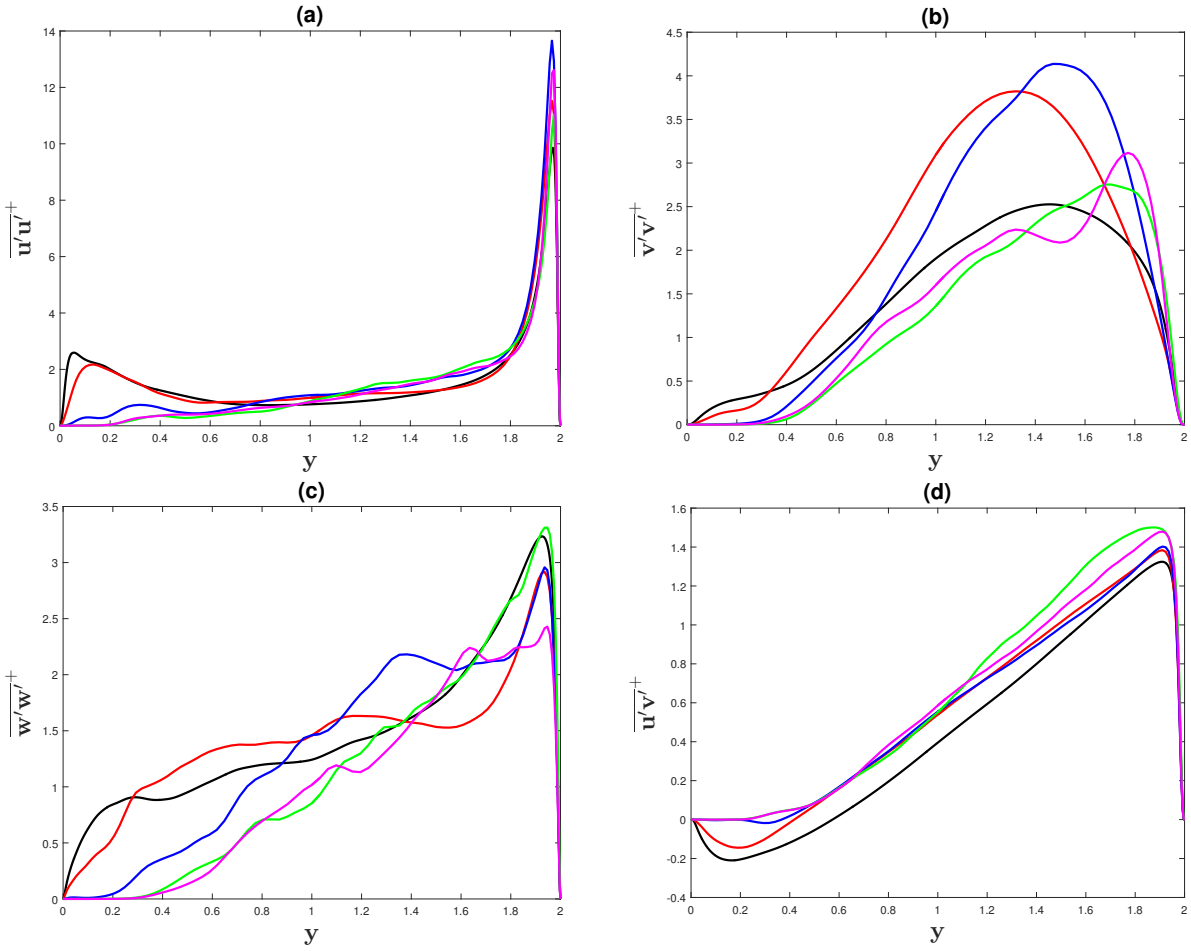

Figure 3.37: Comparison of MFU Reynolds stress distributions for $Ro_b = 0.2$ at a higher-Reynolds number. a) $\overline{u'u'}^+$; b) $\overline{v'v'}^+$; c) $\overline{w'w'}^+$; d) $\overline{u'v'}^+$. Black: Case E ($L_z = 2\pi\delta$); Red: Case $EM1$ ($L_z = \pi\delta$); Blue: Case $EM2$ ($L_z = 0.36\pi\delta$); Green: Case $EM3$ ($L_z = 0.24\pi\delta$); Magenta: Case $EM4$ ($L_z = 0.18\pi\delta$).

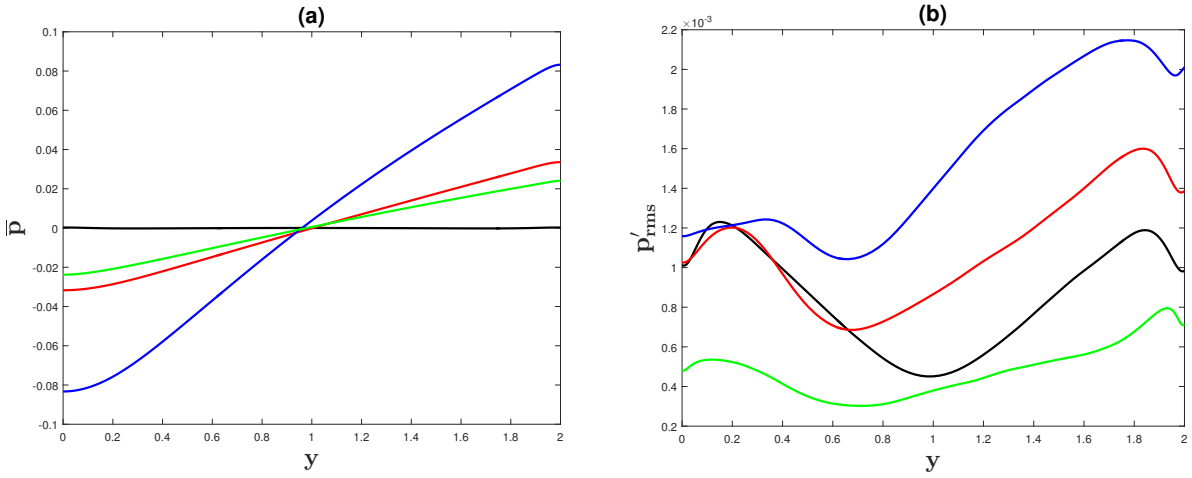

Figure 3.38: Comparison of statistical pressure distributions for the full simulation cases *A*-*C*, *E*. a) $\overline{p}$; b) p'_{rms}. Black: Case *A* ($Re_\tau = 200$, $Ro_b = 0$); Red: Case *B* ($Re_\tau = 197$, $Ro_b = 0.2$); Blue: Case *C* ($Re_\tau = 192$, $Ro_b = 0.5$); Green: Case *E* ($Re_\tau = 406$, $Ro_b = 0.2$).

3.2.5.5 MFU: Pressure Statistics

For rotational flows, the pressure gradient is an important factor in the radial flow spread as it is comprised of the contributions from the centrifugal forces (see Chapter 2). Hence a study of pressure statistics is appropriate for comparing the effectiveness of a model's ability to characterize turbulence. The mean pressure and root-mean-square fluctuating pressure distributions from full simulation cases *A*-*D* are shown in figures 3.38(a) and (b), respectively. In figure 3.38(a), the Coriolis force in simulation cases *B*-*D* was shown to generate an asymmetric profile with a negative and positive mean pressure in the suction and pressure regions, respectively. A higher-Reynolds number was shown to decrease the gradient of the linear mean pressure distribution for $Ro_\mathrm{b} = 0.2$. In figure 3.38(b), an increasing rotation number was demonstrated to significantly increase the amplitudes of the pressure fluctuations in the pressure region but the higher-Reynolds number simulation case *D* showed significantly suppressed p'_{rms} amplitudes throughout the channel.

The effect of a decreasing spanwise length L_z was examined using distributions of pressure statistics for full simulation case *B* and MFU simulation cases *BM*1-*BM*4 in figure 3.39. In figure 3.39(a), the spanwise length was shown to not affect the accuracy of the MFU model as all

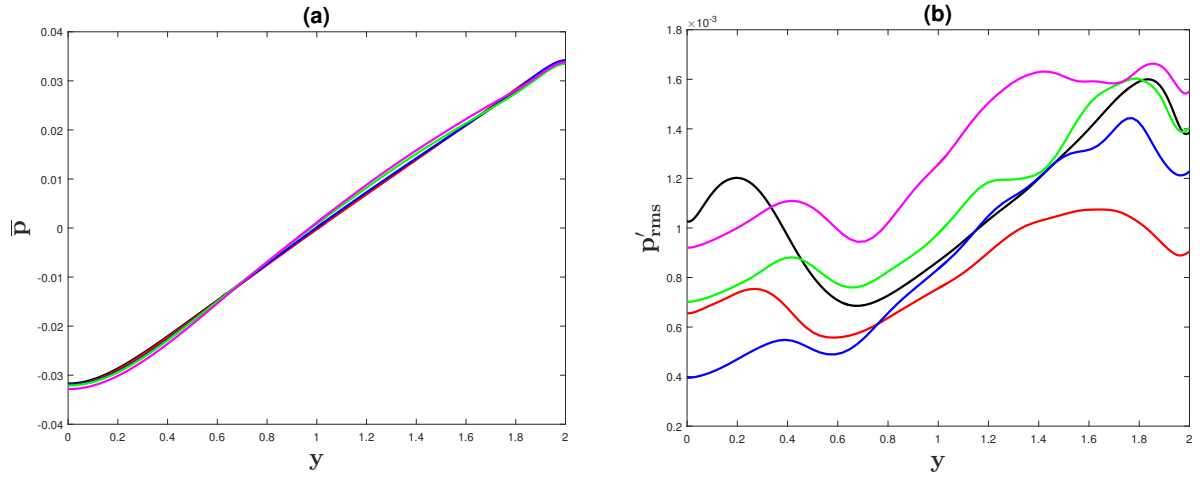

Figure 3.39: Comparison of statistical pressure distributions for the full and MFU simulations for $Ro_b = 0.2$. a) $\overline{p}$; b) p'_{rms}. Black: Case B ($L_z = 2\pi\delta$); Red: Case $BM1$ ($L_z = \pi\delta$); Blue: Case $BM2$ ($L_z = 0.36\pi\delta$); Green: Case $BM3$ ($L_z = 0.24\pi\delta$); Magenta: Case $BM4$ ($L_z = 0.18\pi\delta$).

four MFU simulations accurately approximated the linearity and slope of the mean pressure distribution across the channel. In figure 3.39(b), none of the MFU models were shown to have an accurate root-mean-square pressure fluctuation distribution and little correlation between L_z and MFU accuracy was observed.

3.2.5.6 MFU: Higher-Order Statistics

In a previous section, the baseline MFU model ($L_z = \pi\delta$) was shown to produce accurate mean velocity and Reynolds stress distributions in comparison to the full simulations. By design, MFU models are not expected to accurately model higher-order statistics (Jimenez and Moin, 1991). However, it is instructive to understand the limit at which the MFU models fail to represent the fundamental physics of rotational turbulence. Hence an assessment of higher-order velocity statistics is conducted based on the DNS results of the full and MFU simulations.

For the no-rotation case A ($Ro_b = 0$), the skewness and kurtosis distributions of the full and MFU simulations are shown in figures 3.40(a) and 3.40(b), respectively, indicating favorable comparisons with the full simulation. The main features of $S(u'_i)$ are captured in the MFU model although higher amplitude oscillations and increased asymmetry are observed, as a result of the

decreased grid resolution and domain lengths in case $AM1$. For the flatness distributions displayed in figure 3.40(b), the MFU model shows good accuracy throughout the channel.

The higher-order statistics of skewness and kurtosis are shown for cases C and $CM1$ ($Ro_b = 0.5$) in figures 3.40(c) and 3.40(d), respectively. In the pressure region, the MFU model provides an accurate approximation. However, large increases in $S(u')$, $F(u')$ and $F(v')$ distributions near the suction wall are not correctly realized in the MFU simulations where these quantities decrease. For the full simulations, the increase of $F(u')$ from case A to case C in the suction region is attributed to the disappearance of the turbulence sustenance cycle and subsequent re-laminarization of that region. The turbulence sustenance cycle is characterized by interactions between coherent high and low-speed structures which would produce a leveled PDF distribution and consequently low kurtosis levels. Rotational forces eliminate this structural organization in the suction region and the study by Brethouwer et al. (2013) demonstrated that the flow regime becomes quiescent although it is punctuated by quasi-periodic bursts of high turbulence activity which corresponds with a "peaked" PDF distribution and high kurtosis levels.

The reason for the discrepancy in $F(u')$ between the full and MFU simulations in the suction region in figure 3.40(d) is the MFU model's inability to capture extreme high and low-amplitude fluctuations as shown in the time-averaged x-z plane comparison of u' in figures 3.41(a) and (c). The flow regime of the full simulation in figure 3.41(a) displays pockets of extreme u' levels but no corresponding events are seen in the MFU regime in figure 3.41(c). This issue is also reflected in the comparison of PDF distributions in figures 3.41(b) and (d). Unlike the full simulation PDF shown in figure 3.41(b), a non-physical limitation on u' amplitudes is shown to exist on both ends of the MFU PDF in figure 3.41(d). This truncation results in an incorrect PDF distribution with no tails, causing large underestimations of kurtosis in the suction region as shown in figure 3.40(d). A similar mechanism is also responsible for the suction side differences in $F(v')$ and $S(u')$ between the full and MFU simulations.

Hence MFU inaccuracy in the suction region is attributed to the inability of the MFU model to accurately capture the re-laminarized flow regime characterized by extreme fluctuations in a

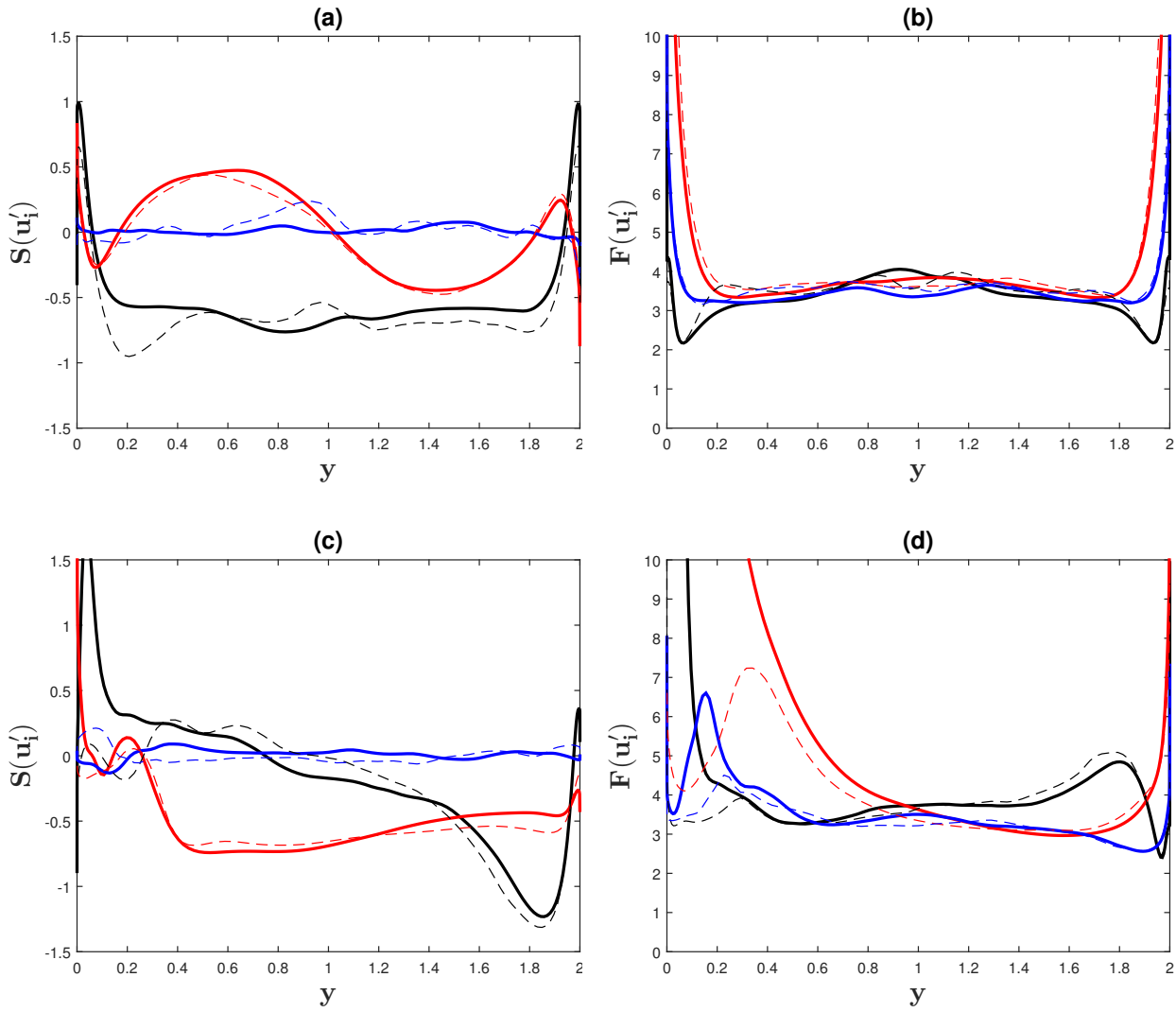

Figure 3.40: Comparison of MFU higher-order statistics. Cases A and $AM1$ ($Ro_b = 0$): a) Skewness; b) Kurtosis. Cases C and $CM1$ ($Ro_b = 0.5$): c) Skewness d) Kurtosis. —: Full simulations; − − −: MFU simulations. Black: u'; Red: v'; Blue: w'.

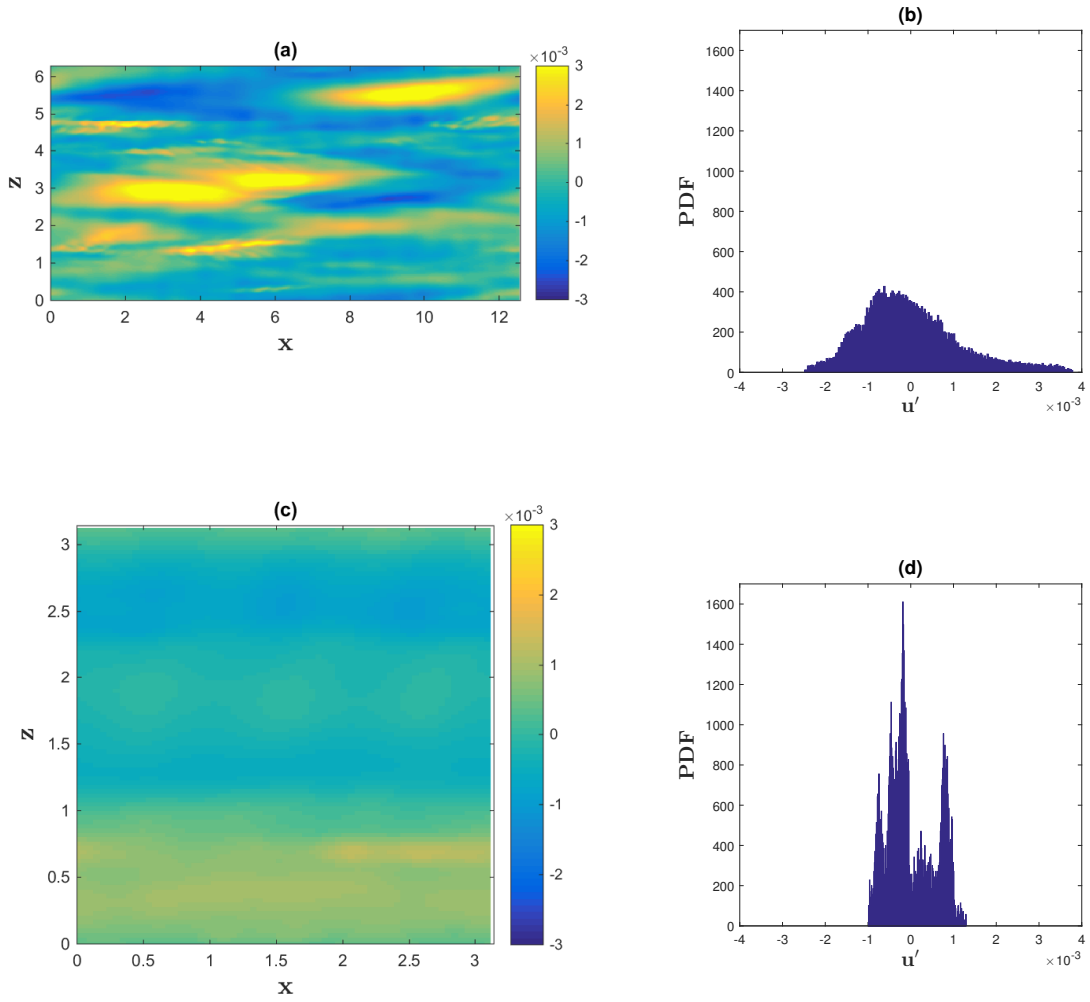

Figure 3.41: Full/MFU simulation comparison of time-averaged x-z fields and probability density functions of $u^{'}$ at $y = 0.06$ (Suction region) for $Ro_{\mathrm{b}} = 0.5$. a) Case C field; b) Case C PDF; c) Case $CM1$ field; b) Case $CM1$ PDF.

quiescent regime (turbulent spots). The MFU model demonstrated good accuracy for higher-order statistics in regions of high turbulent activity, which came as a result of the MFU design capturing the Taylor-Gortler vortices responsible for turbulence production in the pressure region. But with respect to higher-order statistics, the MFU model failed to maintain accuracy in the re-laminarized suction region which is governed by different physical dynamics and coherent structures than the pressure region.

3.2.6 Summary

Results from a direct numerical simulation of complex turbulent channel flows were examined with respect to Taylor-Gortler vortices (roll cells). For the design of a minimal flow unit for rotational turbulence, a baseline MFU model with spanwise domain length of $L_z = \pi\delta$ was selected to accomodate a single full pair of Taylor-Gortler vortices due to the presence of these structures in the highly turbulent pressure region. An examination of the spacing between sublayer streaks in the pressure region of the rotational case showed that the spacing distance remained approximately the same in comparison to the near-wall region of a no-rotation case. A box minimization study with reduced spanwise domain lengths down to $L_z = 0.18\pi\delta$, the MFU length for the non-rotating turbulent channel flow, was conducted. Observed discrepancies in the mean velocity distributions demonstrated that MFU accuracy did not depend on sublayer streak distance as for the non-rotational channel and a significantly larger minimum spanwise length $L_z = \pi\delta$ was required for accurate turbulent statistics, corresponding to the minimum length for proper realization of one full pair of Taylor-Gortler vortices. If these vortices were inaccurately represented from further truncation of the spanwise domain length, turbulent fluctuations were inaccurate and/or an incorrect mean velocity gradient was produced in the pressure region.

This MFU model analysis was extended to another low-Reynolds case with a different rotation number and similar results were observed. For a higher-Reynolds number, the MFU model demonstrated decreased accuracy compared to the lower-Reynolds simulation. Hence for large Reynolds numbers, MFU models may require a significantly larger domain box to accurately ap-

proximate turbulence statistics and alternative factors for MFU design require consideration, such as Reynolds number effects on sublayer streak length and turbulence structures in the suction region. MFU accuracy for pressure statistics was also examined and it was observed that the MFU model accurately approximated the distributions of mean pressure but not fluctuating pressure. To test the limitations of the MFU model, higher-order statistics from the baseline MFU model were compared to those from the full simulations. The model produced accurate distributions of skewness and kurtosis for a non-rotating channel but was unable to maintain this accuracy with rotation in the suction region. The MFU model accurately captured higher-order statistics in the pressure region due to the successful realization of roll cells but could not properly capture the re-laminarized suction region which contained intermittent high-amplitude velocity fluctuations, a consequence of the "turbulent spots" structures. These findings indicate that when the MFU model is extended beyond its intended function of general turbulence quantities (mean velocity, Reynolds stresses) to higher-order statistics, the model continues to perform well in regions of high turbulence due to its ability to capture the coherent structures which contribute to turbulence production. However, the model fails in regions with different physical dynamics such as the low-turbulence suction region.

Chapter 4

Turbulence Closures Models

4.1 Reynolds-Averaged Navier-Stokes (RANS) Models

4.1.1 Introduction

Due to significantly reduced computational costs compared to DNS, Reynolds-Averaged Navier-Stokes (RANS) are highly desirable if they can accurately parameterize turbulent transport. In the present work, we employ DNS to integrate the Navier-Stokes and energy equations and utilize this database to assess four RANS models proposed by (a) Reif et al. (1999), (b) Speziale and Gatski (1993), (c) Girimaji (1996) and (d) Grundestam et al. (2005). In addition, the pressure-strain functions proposed in Speziale and Gatski (1993) and Girimaji (1996) are investigated for their influence on the modeled Reynolds stress distributions.

4.1.2 RANS Model Overview

The engineering approach for the calculation of turbulent flows generally consists of the use of Reynolds-averaged (time-averaged) Navier-Stokes (RANS) equations which require heuristic closure approximations to model the Reynolds stresses that appear in these equations as a result of the time-averaging process. Accurate parameterization of these quantities in terms of the fundamental variables of the problem, often with the application of an eddy (turbulent) viscosity coefficient, is essential for an accurate prediction of turbulent transport. RANS models are often incorporated into engineering applications but have difficulties especially for the modeling of

complex flows with extra mean rates-of-strain. In the present work, the current state of turbulence models in regards to spanwise-rotating turbulent channel flow is evaluated through the examination of four commonly used turbulence models in their ability to accurately characterize turbulent transport with rotational effects.

In the present work for model testing, nonlinear eddy viscosity models are used due to their advantages over linear eddy viscosity models such as the k-ε model (Launder and Shama, 1974) for complex turbulent flows. Linear eddy viscosity models invoke a linear constitutive relationship between the Reynolds stresses and mean flow straining field (Boussinesq approximation) and although these models have produced satisfactory predictions in two-dimensional thin shear flows, they perform poorly in complex turbulent flows with more than one mean flow velocity gradient such as the spanwise-rotating turbulent channel flow considered here (Launder et al., 1975). In figure 4.1, the Reynolds stress distributions of the k-ε model were compared to the present DNS data and a sample nonlinear eddy viscosity model (Grundestam et al., 2005) for case D ($Ro_b = 0.9$). In comparison to the nonlinear eddy viscosity model, the k-ε model demonstrated significantly poorer accuracy especially in regards to proper characterization of the pressure region ($1 \leq y \leq 2$). The k-ε model does produce a very similar distribution with the nonlinear eddy viscosity model for $\overline{u_3'u_3'}^+$ but in general, a clear disadvantage for the linear eddy viscosity model is observed at the high rotation number compared to the nonlinear model.

All of the turbulence closure approximations considered in this work invoke the nonlinear eddy viscosity hypothesis which models the Reynolds stresses as functions of the turbulent kinetic energy (k), dissipation rate (ε) and mean flow gradients in the form of the mean strain rate (S_{ij}) and rotation tensors (W_{ij}). The turbulence model proposed by Reif et al. (1999) (hereafter referred to as the PRDO model) is similar to the $k-\varepsilon$ model in which partial differential equations (PDEs) for k and ε are solved. In addition, the PRDO model incorporates two PDEs for the temporal evolution of $\overline{v^2}$ and f, where $\overline{v^2}$ is the modeled (time-averaged) wall-normal Reynolds stress and f is an elliptic relaxation function which provides kinematic blocking of turbulent transport near the channel walls. Through analytical derivation for this set of four PDEs, the PRDO model produces

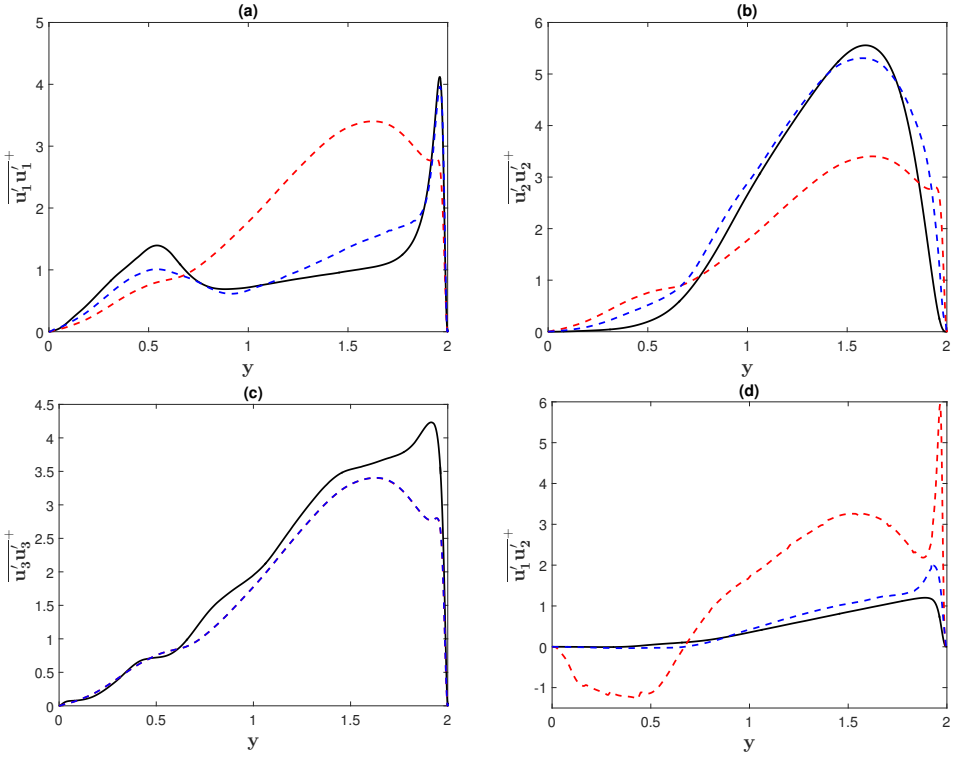

Figure 4.1: Modeled Reynolds stress profiles for case D ($Ro_b = 0.9$). (a) $\overline{u_1'u_1'}^+$; (b) $\overline{u_2'u_2'}^+$; (c) $\overline{u_3'u_3'}^+$; (d) $\overline{u_1'u_2'}^+$. Black: DNS; red: linear eddy viscosity model (Launder and Shama (1974)); blue: nonlinear eddy viscosity model (Grundestam et al. (2005)).

the explicit expression for the Reynolds stresses shown in equation 4.1

$$\overline{u_i'u_j'} = \frac{2}{3}k\delta_{ij} - 2C_\mu^*\overline{v^2}TS_{ij} \tag{4.1}$$

where C_μ^* is a function of the strain rate (S_{ij}) and rotation tensors (W_{ij}) and

$$T = max\left[\frac{k}{\varepsilon}; 6\left(\frac{\nu}{\varepsilon}\right)^{1/2}\right] \tag{4.2}$$

represents a turbulent timescale.

The Speziale-Gatski (SG) and Girimaji (GI) turbulence models, proposed by Speziale and Gatski (1993) and Girimaji (1996), respectively, are EARSM which belong to a common subtype of nonlinear eddy viscosity models. In EARSM, an implicit algebraic model for the anisotropic tensor (b_{ij}) is constructed from the Reynolds stress transport equation through the modeling of individual energy balance terms and an explicit form for b_{ij} is derived analytically. An expression

for the Reynolds stresses is then obtained using the following relation:

$$b_{ij} = \frac{\overline{u_i' u_j'}}{2k} - \frac{1}{3}\delta_{ij} \tag{4.3}$$

The explicit expressions for the Reynolds stresses from the SG and GI models are shown in equations 4.4 and 4.5, respectively. In both models, the terms η_1 and η_2 are equivalent to invariants of the normalized strain rate and rotation tensors, or $S_{ij}S_{ij}$ and $W_{ij}W_{ij}$, respectively. In equation 4.4, α_1 is a function of the production-dissipation ratio and in equation 4.5, the G coefficients are functions of η_1 and η_2.

$$\begin{aligned}\overline{u_i' u_j'} = \frac{2}{3}k\delta_{ij} - 2(S_{ik}S_{kj} - \frac{1}{3}S_{mn}S_{mn}\delta_{ij}) - \\ \frac{6(1+\eta_1^2)\alpha_1 k}{3+\eta_1^2+6\eta_2^2\eta_1^2+6\eta_2^2}(S_{ij} + S_{ij}W_{kj} - W_{ik}S_{kj})\end{aligned} \tag{4.4}$$

$$\begin{aligned}\overline{u_i' u_j'} = 2kG_1 S_{ij} + 2kG_2(S_{ik}W_{kj} + W_{ik}S_{kj}) + \\ 2kG_3(S_{ik}S_{kj} - \frac{1}{3}S_{mn}S_{mn}\delta_{ij}) + \frac{2}{3}k\delta_{ij}\end{aligned} \tag{4.5}$$

The model proposed by Grundestam et al. (2005) (hereafter refered to as the GWJ model) is also an EARSM derived from the Reynolds stress transport equation. Unlike the SG and GI models which use the linear SSG pressure-strain function to model the pressure-strain energy balance term (Speziale et al., 1991), the GWJ model uses a nonlinear pressure-strain function in its formulation. The GWJ model proposes the explicit expression for the Reynolds stresses

$$\overline{u_i' u_j'} = \frac{2}{3}k\delta_{ij} + k\sum_{k=1}^{10}\beta_k T_{ij}^k \tag{4.6}$$

where the T_{ij} tensor components are various functions of the mean strain rate and rotation tensors. Similarly, the β coefficients depend on the tensor invarants defined as

$$\Pi_S = S_{ij}S_{ji}, \quad \Pi_{\Omega^*} = W_{ij}W_{ji}, \quad IV = S_{ij}W_{jk}W_{ki} \tag{4.7}$$

Most of these closure formulations have been shown to produce significant errors in predicting the mean velocity and temperature distributions for rotating turbulent channel flow (e.g. Grundestam et al. (2005) for the GWJ model). Hence in this work, we examine the details of these models to assess the likely sources of such errors in the modeled mean and fluctuating quantities.

4.1.3 RANS Model Results

The normal Reynolds stress $\overline{u_i' u_i'}^+$ and primary shear Reynolds stress $\overline{u_1' u_2'}^+$ distributions calculated using the four aforementioned RANS-based models are compared directly to the present DNS results for simulation cases *A*-*D*. For the no-rotation case *A*, the comparisons are shown in figure 4.2. The approximations of the GWJ and GI models are observed to be similar for all Reynolds stress components. The SG and PRDO models demonstrate the best agreement with DNS results for the normal and shear Reynolds stress distributions, respectively. Also noted in Rung and Thiele (1999), the SG model is observed to not satisfy realizability as the modeled distribution of $\overline{u_2' u_2'}^+$ contains non-physical negative amplitudes near both channel walls. Realizability is a set of mathematical and physical principles that need to be satisfied to prevent the turbulence model from generating non-physical results. The three realizability conditions proposed by Schumann (1977) are

$$\overline{u_i' u_i'} \geq 0 \tag{4.8}$$

$$\overline{u_i' u_j'}^2 \leq \overline{u_i' u_i'}\,\overline{u_j' u_j'} \tag{4.9}$$

$$det(\overline{u_i' u_j'}) \geq 0 \tag{4.10}$$

where *det* is the tensor determinant.

For case *B* ($Ro_b = 0.2$), the modeled Reynolds stresses and DNS results are shown in figure 4.3 and all four turbulence models demonstrate proper characterization of the suppressed and enhanced turbulence levels in the suction and pressure regions, respectively. However, the three EARSM-type models (GWJ, SG, GI) display better agreement with DNS results than the PRDO model, which displayed identical distributions of $\overline{u_i' u_i'}^+$. The poor performance of the PRDO model is likely the result of the linear relationship between the Reynolds stress and mean strain rate tensors (Equation 4.1). With respect to the DNS, the SG model showed the best agreement for the normal Reynolds stresses but all four turbulence models failed to predict the Reynolds shear stress profile in the pressure region. For all cases, the PRDO and GWJ models produce identical distributions for spanwise Reynolds stress $\overline{u_3' u_3'}^+$ which was unexpected due to the significant dif-

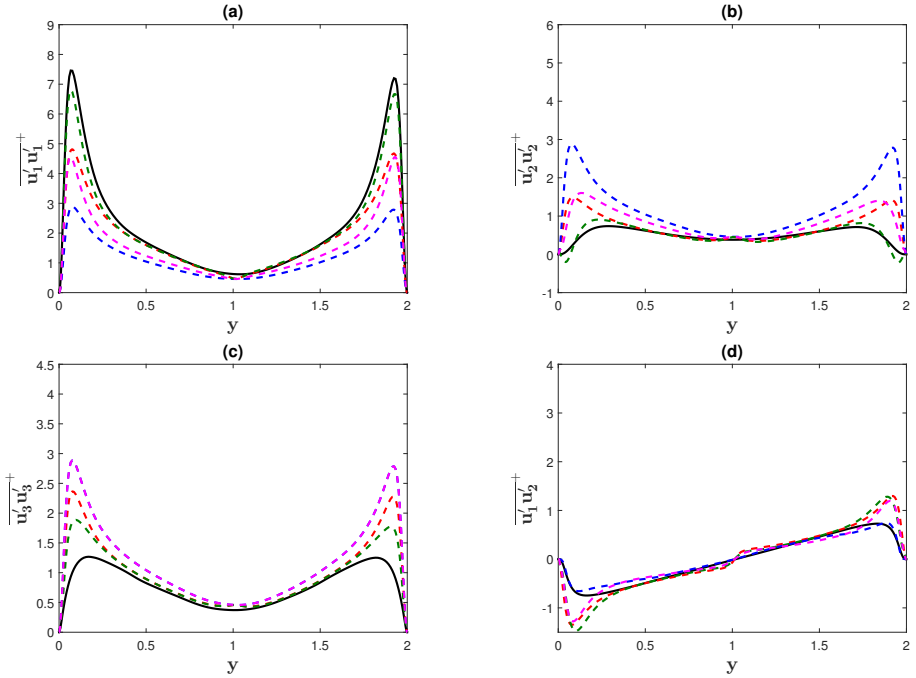

Figure 4.2: Modeled Reynolds stress profiles for case A ($Ro_b = 0$). (a) $\overline{u_1' u_1'}^+$; (b) $\overline{u_2' u_2'}^+$; (c) $\overline{u_3' u_3'}^+$; (d) $\overline{u_1' u_2'}^+$. Black: DNS; blue: PRDO; green: SG; red: GI; magenta: GWJ.

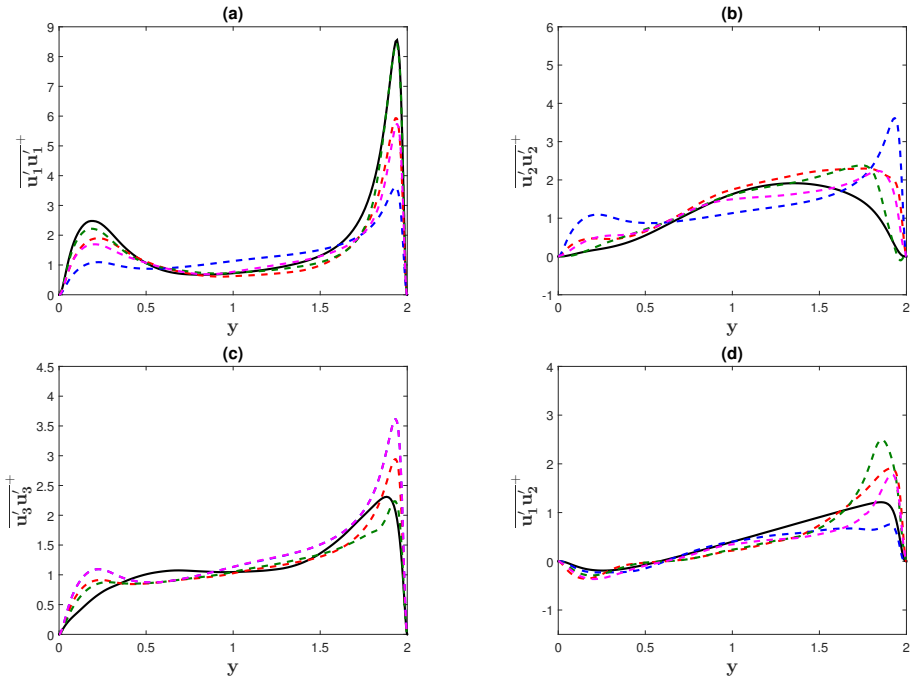

Figure 4.3: Modeled Reynolds stress profiles for case B ($Ro_b = 0.2$). (a) $\overline{u_1' u_1'}^+$; (b) $\overline{u_2' u_2'}^+$; (c) $\overline{u_3' u_3'}^+$; (d) $\overline{u_1' u_2'}^+$. Black: DNS; blue: PRDO; green: SG; red: GI; magenta: GWJ.

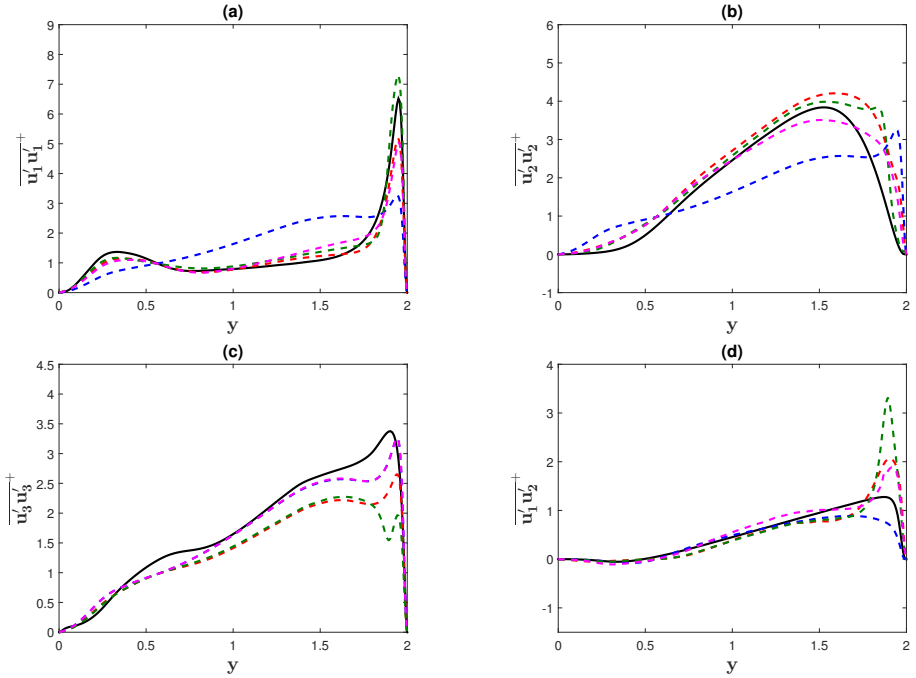

Figure 4.4: Modeled Reynolds stress profiles for case C ($Ro_b = 0.5$). (a) $\overline{u_1' u_1'}^+$; (b) $\overline{u_2' u_2'}^+$; (c) $\overline{u_3' u_3'}^+$; (d) $\overline{u_1' u_2'}^+$. Black: DNS; blue: PRDO; green: SG; red: GI; magenta: GWJ.

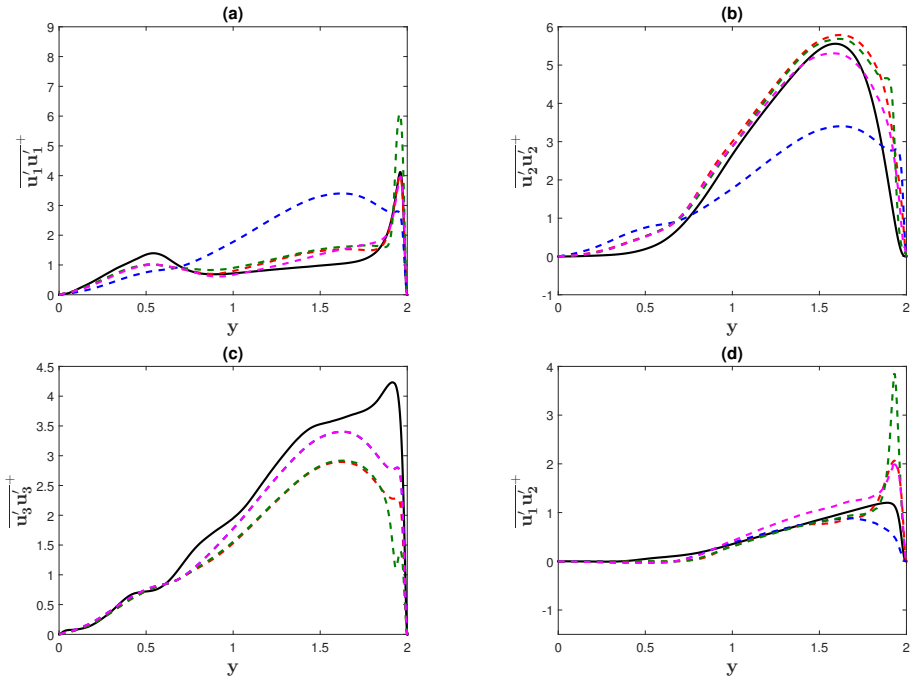

Figure 4.5: Modeled Reynolds stress profiles for case D ($Ro_b = 0.9$). (a) $\overline{u_1' u_1'}^+$; (b) $\overline{u_2' u_2'}^+$; (c) $\overline{u_3' u_3'}^+$; (d) $\overline{u_1' u_2'}^+$. Black: DNS; blue: PRDO; green: SG; red: GI; magenta: GWJ.

ferences in the modeled PRDO and GWJ expressions shown in equations 4.1 and 4.6, respectively. The SG model again fails to satisfy realizability as negative amplitudes of $\overline{u_2'u_2'}^+$ are observed near the pressure wall ($y = 2$) in figure 4.3(b).

The DNS and modeled Reynolds stresses for cases *C* ($Ro_b = 0.5$) and *D* ($Ro_b = 0.9$) are shown in figures 4.4 and 4.5, respectively. The invariance of the normal Reynolds stress distributions from the PRDO model continues to result in poor agreement with the DNS in relation to EARSM. The GWJ model demonstrates the best correspondence with DNS data for cases *C* and *D*. For case *C*, the modeled SG Reynolds stress distributions develop disparities with the DNS near the pressure wall as the peak modeled amplitude of $\overline{u_1'u_2'}^+$ is significantly over-estimated in figure 4.4(d) and an unexpected decrease of $\overline{u_3'u_3'}^+$ amplitudes is observed in figure 4.4(c). For case *D*, these issues worsen and the modeled SG distributions demonstrate significant deviations from the DNS for all Reynolds stress components except $\overline{u_2'u_2'}^+$. For cases *C* and *D*, the SG model is shown to satisfy the previously violated realizability condition as the modeled distributions of $\overline{u_2'u_2'}^+$ in figures 4.4(b) and 4.5(b) remain non-negative throughout the entire channel.

For no-rotation, all four tested turbulence models produced Reynolds stress distributions in close agreement with the present DNS results. For rotating simulation cases *B*-*D*, the EARSM (GWJ, SG, GI) had significantly better agreement with the DNS than the PRDO model, a different type of nonlinear eddy viscosity model. This observation supports the current trend of turbulence model design for rotational favoring EARSM-type closures Grundestam et al. (2005). One notable deficiency of EARSM is generally manifested in the near-wall regions where significant deviations of $\overline{u_i'u_j'}$ from the DNS distributions are observed. It is therefore instructive to examine the parameterization used for the pressure-strain term as this term is responsible for intercomponent energy transfer.

4.1.4 EARSM: Pressure-Strain Modeling

The pressure-strain term (Equation 3.17) is of paramount importance as the correlations between pressure and rate-of-strain fluctuations play a dominant role in intercomponent energy

transfer (Launder et al., 1975) within the Reynolds stress equation (Equation 3.14). Both the SG and GI EARSM apply the linear Speziale, Sarkar and Gatski (SSG) pressure strain function (equation 4.11), albeit with different sets of numerical coefficients as their algebraic formulations differ.

$$\Pi_{ij} = -C_1 \epsilon b_{ij} + C_2 k S_{ij} + C_3 k (b_{ik} S_{kj} + S_{ik} b_{kj}) - \frac{2}{3} C_3 b_{mn} S_{mn} \delta_{ij} - C_4 k (b_{ik} W_{kj} - W_{ik} b_{kj}) \tag{4.11}$$

In figures 4.6 and 4.7, the distributions of the pressure-strain closure formula for the SG and GI models are compared to the pressure-strain distributions directly extracted from the present DNS data to evaluate possible sources of error specifically for cases A ($Ro_b = 0$) and B ($Ro_b = 0.2$).

Figure 4.6 displays results for case A ($Ro_b = 0$), the modeled pressure-strain function values for both models are similar to the DNS results in the interior of the channel. However, near both walls where most of the intercomponent energy transfer takes place, the modeled pressure-strain amplitudes are drastically overestimated for both the SG and GI models. This discrepancy is not unexpected as the SSG function is a single-point closure which captures only the local effects of the pressure-strain correlations, neglecting nonlocal effects such as wavevector information (Mishra and Girimaji, 2013). In figure 4.7, similar comparisons are presented for case B ($Ro_b = 0.2$). It is observed that the modeled pressure-strain distributions have better agreement with the DNS data with increasing rotation number near the suction wall ($y = 0$) and the only major disparity occurs near the pressure wall with suppressed amplitudes from re-laminarization in the suction region.

In figures 4.6 and 4.7, it is observed that Π_{11} is a loss term for $\overline{u_1' u_1'}^+$ and Π_{22} and Π_{33} are gain terms for their corresponding Reynolds normal stresses. This is expected because the main contribution of the pressure-strain correlation term is to isotropize (return-to-isotropy) the normal Reynolds stress components. In non-rotating turbulent channel flow, the production term contributes only to $\overline{u_1' u_1'}^+$, so the pressure-strain tensor isotropizes the normal Reynolds stresses through a negative contribution to $\overline{u_1' u_1'}$ and positive contributions to $\overline{u_2' u_2'}^+$ and $\overline{u_3' u_3'}^+$. It is also observed that these pressure-strain models extract too much energy from $\overline{u_1' u_1'}^+$ and transfer excess energy to $\overline{u_2' u_2'}^+$ and $\overline{u_3' u_3'}^+$, which is directly reflected in the corresponding modeled

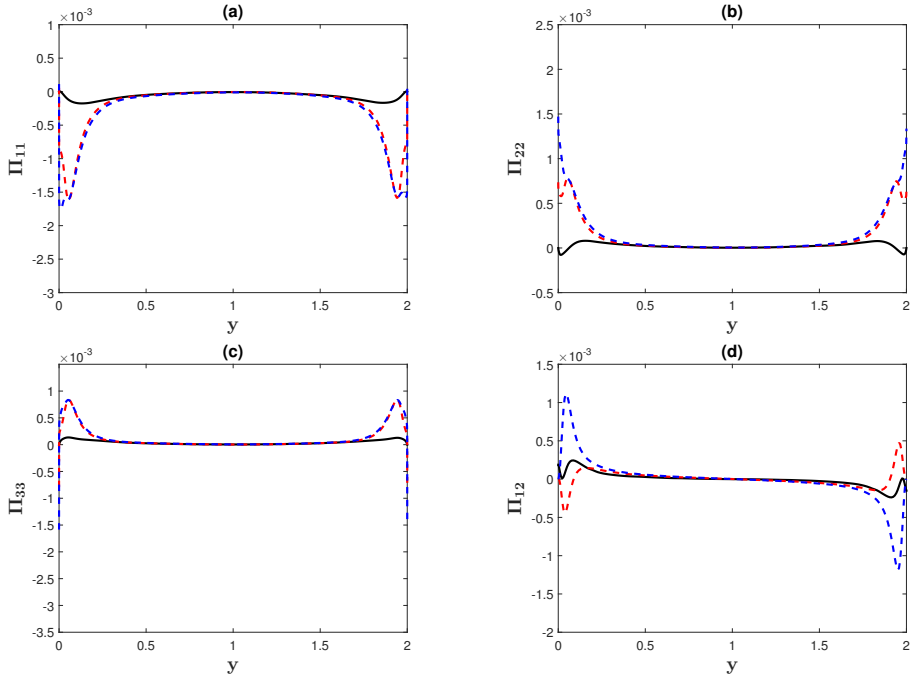

Figure 4.6: Modeled pressure-strain budget term profiles for case A ($Ro_b = 0$). (a) Π_{11}; (b) Π_{22}; (c) Π_{33}; (d) Π_{12}. Black: DNS; red: SG; blue: GI.

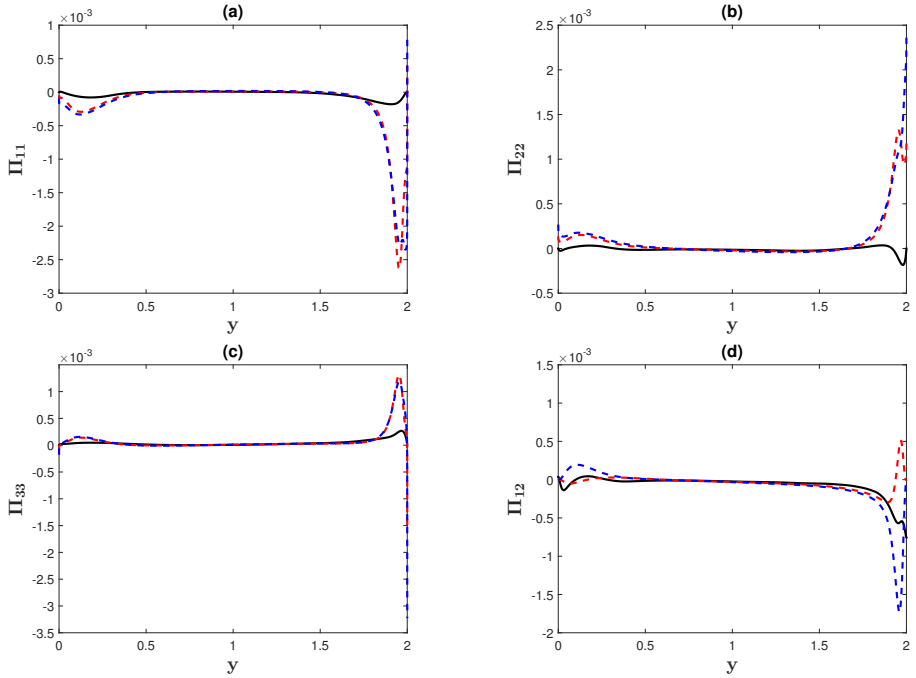

Figure 4.7: Modeled pressure-strain budget term profiles for case B ($Ro_b = 0.2$). (a) Π_{11}; (b) Π_{22}; (c) Π_{33}; (d) Π_{12}. Black: DNS; red: SG; blue: GI.

Reynolds stress distributions in figures 4.2 and 4.3.

4.1.5 Summary

For spanwise-rotating turbulent channel flow, the Reynolds stress distributions produced from a linear and nonlinear eddy viscosity model were compared to demonstrate improved accuracy for the nonlinear model over the linear model. In a comparison of four nonlinear eddy viscosity models with DNS data, EARSM were the most compatible with DNS results in modeling the Reynolds stresses for turbulent channel flow subject to spanwise rotation. The Speziale-Gatski (SG) model was shown to be the most compatible for zero and low rotation numbers but displayed significant deviations near the pressure wall at high rotation numbers. The Grundestam-Wallin-Johansson (GWJ) model showed the best agreement with the DNS data at high rotation numbers.

The pressure-strain models of two EARSM (Girimaji, SG) were shown to have significant disagreements with the DNS data in the near-wall regions. The errors in the modeled contributions from these terms resulted in degeneration of the predictive capabilities of their respective closure models. These errors contributed to inaccurate Reynolds stress amplitudes in the near-wall regions. Present results indicate correct characterization of pressure fluctuations is a crucial factor in EARSM design for spanwise-rotating turbulent channel flow.

4.2 Heat Transfer Models

4.2.1 Introduction

Due to significantly reduced computational costs compared to DNS, turbulent heat flux models are also highly desirable if they can accurately parameterize thermal transport in rotational turbulence. In the present work, we employ DNS to integrate the Navier-Stokes and energy equations and utilize this database to assess two algebraic heat flux models proposed by (a) Younis et al. (2012) and (b) Abe and Suga (2000). In addition, the pressure-temperature-gradient functions proposed in the two models are investigated for their influence on the modeled turbulent heat flux

distributions.

4.2.2 Heat Transfer Model Overview

Heat transfer models parameterize turbulent heat fluxes which are correlations between velocity and temperature fluctuations. The following two heat flux models that we consider in the present work are used frequently in engineering calculations (Li et al., 2014). The YWL heat flux model proposed by Younis et al. (2012) is an Explicit Algebraic Heat Flux Model (EAHFM). For EAHFM, the transport equation for $\overline{u_i'\theta'}$ may be written as

$$\frac{D\overline{u_i'\theta'}}{Dt} = D_{i\theta} + P_{i\theta} + G_{i\theta} + \Pi_{i\theta} + \varepsilon_{i\theta} \tag{4.12}$$

The terms $D_{i\theta}$, $P_{i\theta}$, $G_{i\theta}$, $\Pi_{i\theta}$ and $\varepsilon_{i\theta}$ represent heat flux diffusion, production of heat flux through shear forces, production of heat flux through rotational forces, pressure-temperature-gradient correlations and viscous dissipation, respectively.

The $\overline{u_i'\theta'}$ expression obtained from the YWL model is given in equation 4.13 below. Here, the coefficients C_{2t}, C_{3t} and C_{4t} are absolute constants while C_{1t} is a wall function dependent on invariants of the anisotropic stress tensor; Ω is the angular rotation rate vector.

$$\begin{aligned} -\overline{u_i'\theta'} = C_{1t}\frac{k^2}{\varepsilon}\frac{\partial\overline{\theta}}{\partial x_i} + \frac{\partial\overline{\theta}}{\partial x_j}\left[C_{2t}\frac{k}{\varepsilon}\overline{u_i'u_j'} + C_{3t}\frac{k^3}{\varepsilon^2}\left(\frac{\partial\overline{U_i}}{\partial x_j} + \epsilon_{mji}\Omega_m\right)\right] \\ + C_{4t}\frac{k^2}{\varepsilon^2}\frac{\partial\overline{\theta}}{\partial x_j}\left[\overline{u_i'u_k'}\left(\frac{\partial\overline{U_j}}{\partial x_k} + \epsilon_{jmk}\Omega_m\right) + \overline{u_j'u_k'}\left(\frac{\partial\overline{U_i}}{\partial x_k} + \epsilon_{imk}\Omega_m\right)\right] \end{aligned} \tag{4.13}$$

The heat flux model proposed by Abe and Suga (2000) (hereafter referred to as the SA model) is also an EAHFM but unlike the YWL model, the SA model incorporates nonlinear Reynolds stress terms in its model expressions given in equation 4.14. The terms C_θ and τ represent a wall function and time scale (k/ε), respectively. The expressions for tensors α_{ij} and σ_{ij} are shown in equations 4.15 and 4.16, respectively. Ω_{ij} is the mean rotation tensor and the coefficients $c_{\alpha 0}$, $c_{\alpha 1}$, $c_{\sigma 0}$, $c_{\sigma 1}$ and $c_{\sigma 2}$ are composed of weight functions and the normalized second invariant of the mean strain rate tensor.

$$\overline{u_i'\theta'} = -C_\theta k\tau(\sigma_{ij} + \alpha_{ij})\frac{\partial\overline{\theta}}{\partial x_j} \tag{4.14}$$

$$\alpha_{ij} = c_{\alpha 0}\tau\Omega_{ij} + c_{\alpha 1}\tau(\Omega_{il}\overline{u_1'u_j'}/k + \Omega_{il}\overline{u_1'u_j'}/k) \tag{4.15}$$

$$\sigma_{ij} = c_{\sigma 0}\delta_{ij} + c_{\sigma 1}\overline{u_i'u_j'}/k + c_{\sigma 2}\overline{u_i'u_1'}\,\overline{u_1'u_j'}/k^2 \tag{4.16}$$

4.2.3 Heat Transfer Model Results

Similar to previous RANS model testing, the YWL and SA modeled turbulent heat flux distributions are directly compared to DNS results for simulation cases *A*-*D*. In figures 4.8(a) and (b), the DNS and model distributions of the streamwise and wall-normal turbulent heat fluxes, $\overline{u_1'\theta'}^+$ and $\overline{u_2'\theta'}^+$, respectively, are shown for the no-rotation case *A* ($Ro_b = 0$). Good agreement is displayed with the DNS results for both $\overline{u_1'\theta'}^+$ and $\overline{u_2'\theta'}^+$. In figures 4.8(c) and (d), inconsistencies develop in the YWL and SA modeled heat flux distributions for case *B* ($Ro_b = 0.2$). Both models show good agreement with the DNS for $\overline{u_1'\theta'}^+$ in the suction region but overestimate the peak amplitudes near the pressure wall ($y = 2$). In addition, neither model approximates the linear distribution of $\overline{u_2'\theta'}^+$ at the channel centre shown in the DNS results.

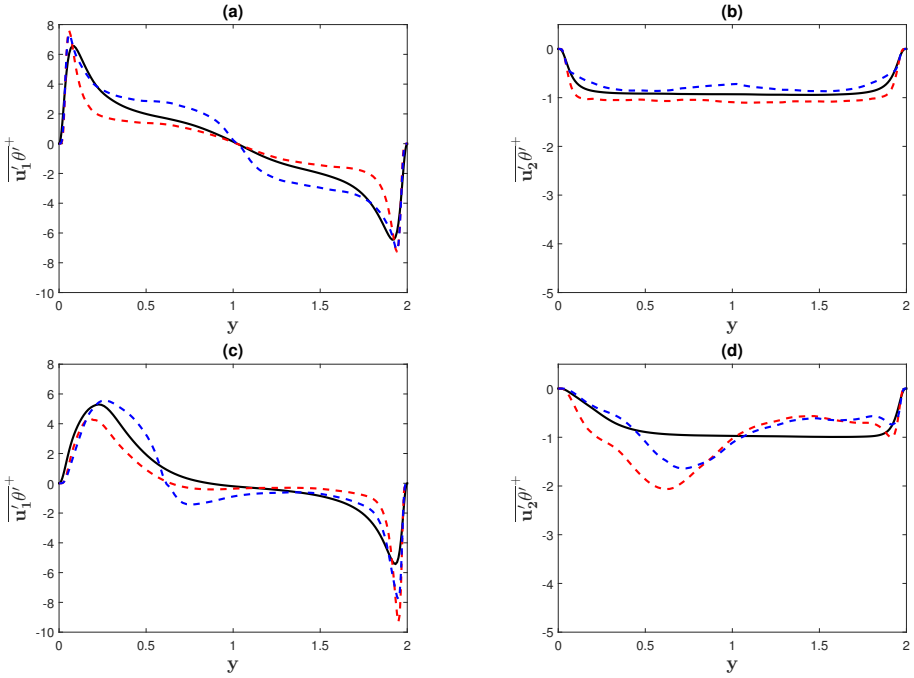

Figure 4.8: Modeled turbulent heat flux profiles for cases *A* ($Ro_b = 0$) and *B* ($Ro_b = 0.2$). (a) $\overline{u_1'\theta'}^+$ (case *A*); (b) $\overline{u_2'\theta'}^+$ (case *A*); (c) $\overline{u_1'\theta'}^+$ (case *B*); (d) $\overline{u_2'\theta'}^+$ (case *B*). Black: DNS; red: YWL; blue: SA.

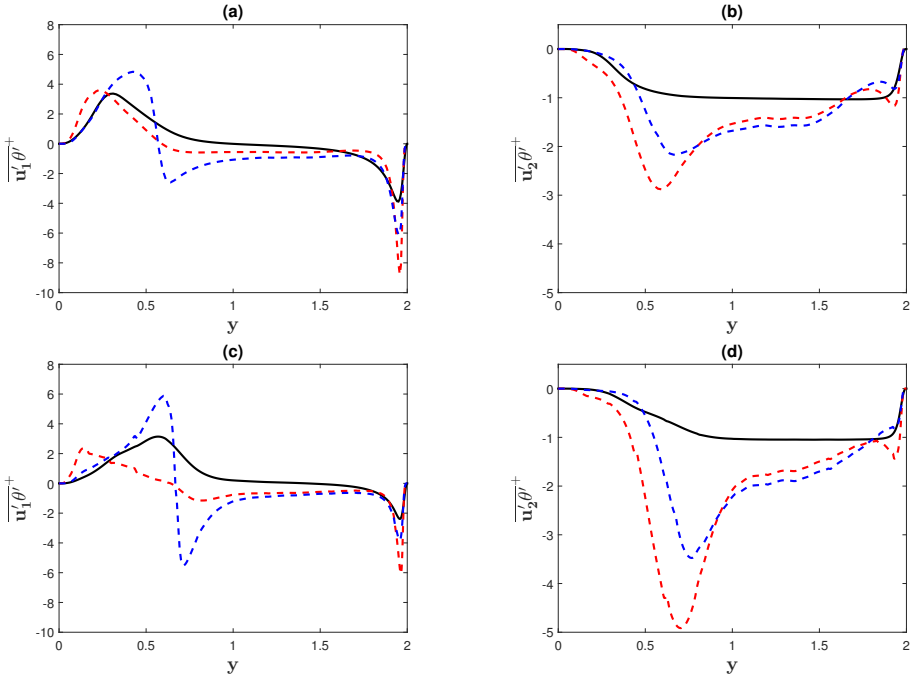

Figure 4.9: Modeled turbulent heat flux profiles for cases C ($Ro_b = 0.5$) and D ($Ro_b = 0.9$). (a) $\overline{u_1'\theta'}^+$ (case C); (b) $\overline{u_2'\theta'}^+$ (case C); (c) $\overline{u_1'\theta'}^+$ (case D); (d) $\overline{u_2'\theta'}^+$ (case D). Black: DNS; red: YWL; blue: SA.

In figure 4.9, the modeled heat flux distributions from the YWL and SA models are shown and compared with the DNS results for cases C ($Ro_b = 0.5$) and D ($Ro_b = 0.9$). In figure 4.9(a), a non-physical dropoff in $\overline{u_1'\theta'}^+$ distributions from both the SA and YWL models is observed for case C near $y = 0.6$. In figure 4.9(c), this discrepancy worsens at a higher rotation number in case D ($Ro_b = 0.9$). Increasing departure from DNS data was also observed for increasing rotation number in the modeled distributions of $\overline{u_2'\theta'}^+$. With an increase in Rossby number, the DNS amplitudes of $\overline{u_2'\theta'}^+$ are shown to become more suppressed in the suction region but the modeled distributions instead display significant amplitude increases of $\overline{u_2'\theta'}^+$ throughout the channel. Through comparison of turbulent heat flux distributions with DNS results for system rotation, both heat transfer models displayed significant deviations that increased with increasing rotation number. As pressure-strain correlations were shown to influence EARSM accuracy, it is instructive to examine the parameterization used for the pressure-temperature-gradient correlations in EAHFM.

4.2.4 EAHFM: Pressure-Temperature-Gradient Correlation Modeling

In the present work, EAHFM modeling of the pressure-temperature-gradient correlation term,

$$\Pi_{i\theta} = \overline{p'\partial\theta'/\partial x_i} \tag{4.17}$$

in the transport equation for the turbulent heat fluxes (equation 4.12) is investigated for error contributions to the corresponding modeled profiles of $\overline{u_i'\theta'}$. In the previous section, correlations of pressure fluctuations were demonstrated to produce significant contributions to turbulence dynamics and Liu and Lun (2007) noted $Pi_{2\theta}$ was a major source term to $\overline{u_2'\theta'}$. The SA model uses the pressure-scalar correlation model proposed in Launder (1975)

$$\Pi_{i\theta} = -C_{1\theta}\frac{\varepsilon}{k}\overline{u_i'\theta} - C_{2\theta}\overline{u_k'\theta}\frac{\partial\overline{U_i}}{\partial x_k} \tag{4.18}$$

where $(C_{1\theta}, C_{2\theta}) = (3, 0.4)$. The YWL model uses the same pressure-scalar correlation model with additional corrective terms,

$$\Pi_{i\theta} = -C_{1\theta}\frac{\varepsilon}{k}\overline{u_i'\theta'} - C_{2\theta}\overline{u_k'\theta'}\frac{\partial\overline{U_i}}{\partial x_k} - C_{1\theta}^{w}P_{i\theta} - C_{2\theta}^{w}C_{2\theta}P_{i\theta}n_i n_k f \tag{4.19}$$

where $(C_{1\theta}, C_{2\theta}, C_{1\theta}^{w}, C_{2\theta}^{w}) = (3, 0.5, 0.5, 0.5)$ and $P_{i\theta}$ represents the production rate of heat flux through mean velocity and temperature gradients,

$$P_{i\theta} = -\left(\overline{u_k'\theta'}\frac{\partial\overline{U_i}}{\partial x_k} + \overline{u_k'u_i'}\frac{\partial\overline{\theta}}{\partial x_k}\right) \tag{4.20}$$

n and f denote a unit vector and wall-damping function, respectively.

In figure 4.10, the modeled pressure-temperature-gradient distributions from the YWL and SA models are compared to DNS results for selected cases A ($Ro_b = 0$) and B ($Ro_b = 0.2$). For case A, $\Pi_{1\theta}$ and $\Pi_{2\theta}$ are gain terms for the corresponding turbulent heat fluxes, in agreement with Liu and Lun (2007). In figures 4.10(a) and (b), both models demonstrate significant overestimations of $\Pi_{1\theta}$ in the near-wall regions, similar to the tested pressure-strain models. There is significantly better agreement between the modeled and DNS distributions for $\Pi_{2\theta}$ and the SA model shows exceptional accuracy.

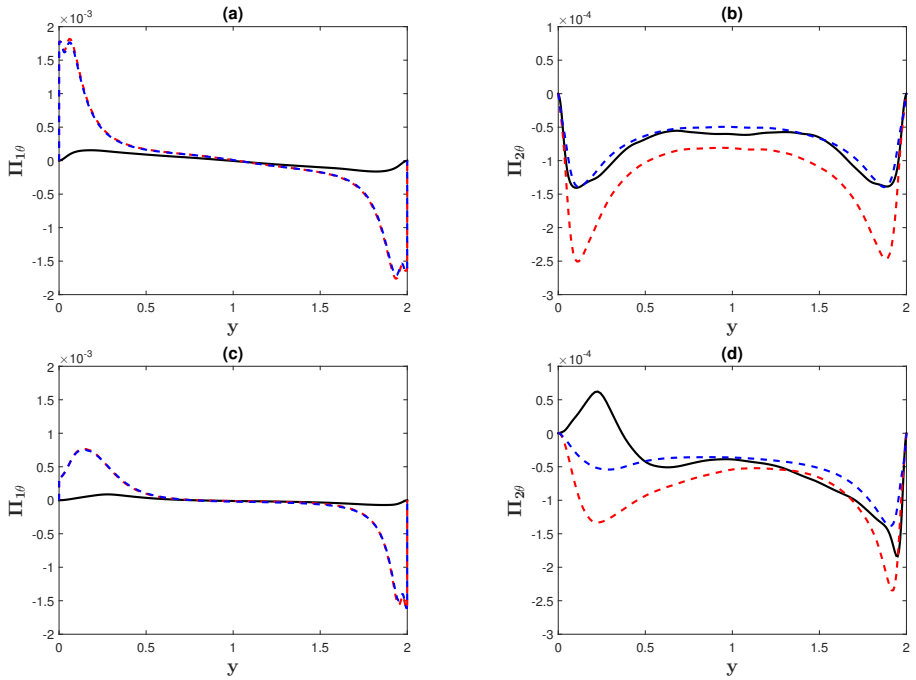

Figure 4.10: Modeled pressure-temperature-gradient profiles for cases A ($Ro_b = 0$) and B ($Ro_b = 0.2$). (a) $\Pi_{1\theta}$ (case A); (b) $\Pi_{2\theta}$ (case A); (c) $\Pi_{1\theta}$ (case B); (d) $\Pi_{2\theta}$ (case B). Black: DNS; red: YWL; blue: SA.

For case B, $\Pi_{1\theta}$ continues to be a source term for $\overline{u_1'\theta'}^+$ but $\Pi_{2\theta}$ changes to become a loss term for $\overline{u_2'\theta'}^+$ in the suction region. This feature is not captured by the YWL and SA models, resulting in significant model disparity from DNS results in the suction region. This major error in the pressure-temperature-gradient correlation term is shown to contribute to inaccuracies in the corresponding modeled heat flux distributions in figure 4.8(d). $\Pi_{2\theta}$ is incorrectly characterized by both models as a gain term for case B, resulting in significant overestimations of modeled $\overline{u_2'\theta'}^+$ in the suction region. The examination of error contributions from Π_{ij} and $\Pi_{i\theta}$ functions to their corresponding models demonstrated the profound effects of pressure correlations on turbulent transport in non-rotating and rotating turbulent channel flow.

4.2.5 Summary

For spanwise-rotating turbulent channel flow, the turbulent heat flux models were in good agreement with DNS data for the no-rotation case but with system rotation, the models deviated

from the DNS, increasing at higher rotation rates. The pressure-temperature-gradient models of two EAHFM (YWL, SA) demonstrated inaccurate characterization of the suction region with system rotation. The errors in the modeled contributions from these terms resulted in degeneration of the predictive capabilities of their respective closure models. These errors contributed to an inaccurate modeled distribution shape for EAHFM and present results indicate correct characterization of pressure-temperature-gradient correlations is a crucial factor in EAHFM design for spanwise-rotating turbulent channel flow.

4.3 High-Order Closures

4.3.1 Introduction

Two closure models used for predicting high-order moments as a function of lower-order terms will be evaluated here. These models rely on the empirical coefficients that have been selected to fit experimental observations. Using data obtained from the DNS, the two models, originally developed for application to the neutral and unstable turbulent Ekman layer (Gryanik and Hartmann, 2002, Mole and Clarke, 1995), are applied to rotating turbulent channel flow. New coefficients are recommended for highest compatibility with the DNS results and are evaluated with respect to the empirical model coefficients.

4.3.2 Kurtosis Model

The higher-order moments of skewness and kurtosis computed from the DNS data base are used to test the quadratic skewness-kurtosis model proposed by Mole and Clarke (1995)

$$K_{u_i} = \alpha \left(S_{u_i}^2 + 1 \right) \tag{4.21}$$

The DNS plots of kurtosis vs. skewness are shown for case A ($Ro_b = 0$) in figures 4.11 – 4.13 with modeled distributions using selected α coefficients.

From Fig. 4.11, it is demonstrated the near-wall regions ($S_u > -0.5$) are well approximated by the $\alpha = 2.1$ curve. However, in the channel center ($S_u < -0.5$), the modeled distribution be-

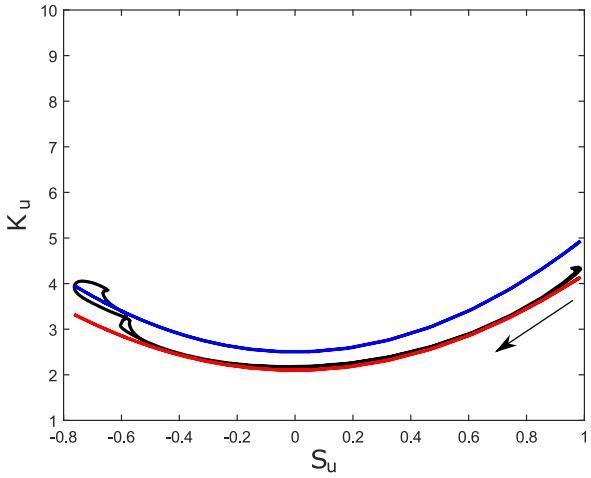

Figure 4.11: Skewness vs. kurtosis distributions for the streamwise velocity component for simulation case A ($Ro_b = 0$). Black line: DNS; Red line, $\alpha = 2.1$; Blue line, $\alpha = 2.5$. Arrow indicates increasing y.

comes inaccurate and $\alpha = 2.5$ is shown to better approximate this region. The recommendation of $\alpha = 2.3$ by Tampieri et al. (2000) fits well with these observations. For the wall-normal and spanwise skewness-kurtosis diagrams in figures 4.12 and 4.13, respectively, the quadratic model is incapable of modeling the near-wall region where large increases of kurtosis occur for small changes in skewness. For selected ranges of α, the model does approximate the centre channel region accurately for these quantities. The coefficient ranges are$\alpha = 3.0 - 3.7$ in figure 4.12 and $\alpha = 3.2 - 3.6$ in figure 4.13.

The selected α values for case A ($Ro_b = 0$) differ significantly from the best-fit coefficients for the neutral Ekman layer which found the proposed coefficients of Alberghi et al. (2002) provided the closest approximation. Instead the coefficients proposed by Tampieri et al. (2000), $\alpha = 2.3$ and 3.3 respectively for the streamwise and wall-normal kurtosis, are shown to be more accurate for non-rotating turbulent channel flow. The quadratic approximation for kurtosis as a function of skewness is effective with exception of the near-wall region for the spanwise and wall-normal velocity components as the model is unable to capture the significant near-wall increases of kurtosis.

The quadratic model of Mole and Clarke (1995) is tested for rotational case B ($Ro_b = 0.2$) and

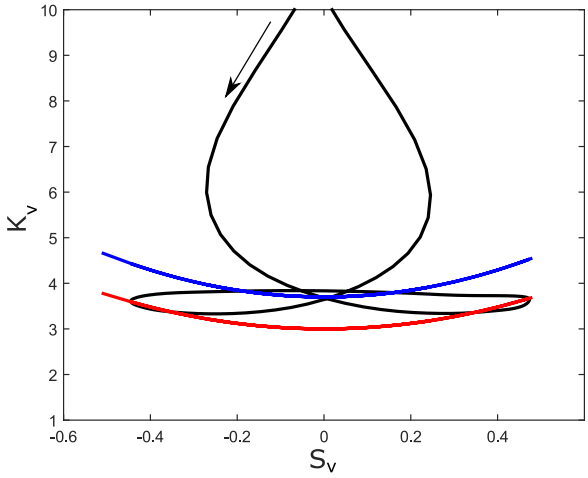

Figure 4.12: Skewness vs. kurtosis distributions for the wall-normal velocity component for simulation case A ($Ro_b = 0$). Black line: DNS; Red line, $\alpha = 3.0$; Blue line, $\alpha = 3.7$. Arrow indicates increasing y.

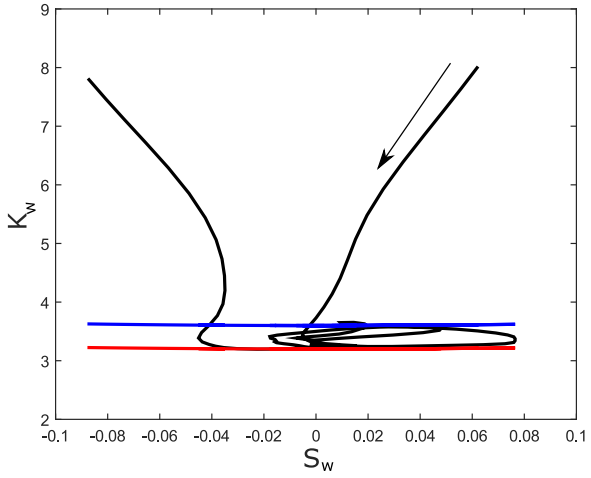

Figure 4.13: Skewness vs. kurtosis distributions for the spanwise velocity component for simulation case A ($Ro_b = 0$). Black line: DNS; Red line, $\alpha = 3.2$; Blue line, $\alpha = 3.6$. Arrow indicates increasing y.

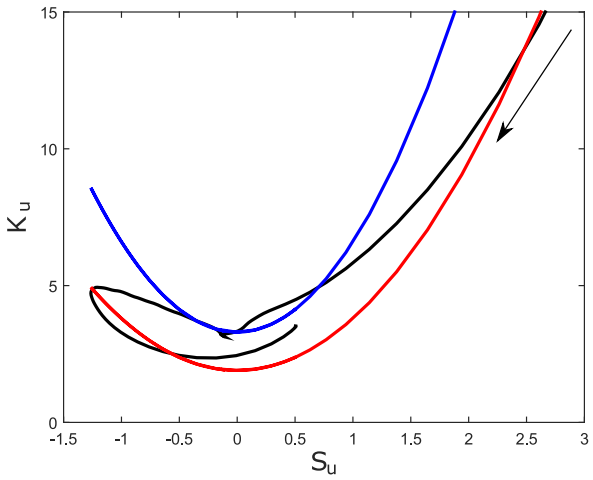

Figure 4.14: Skewness vs. kurtosis distributions for the streamwise velocity component for simulation case B ($Ro_b = 0.2$). Black line: DNS; Red line, $\alpha = 1.9$; Blue line, $\alpha = 3.3$. Arrow indicates increasing y.

plots of skewness vs. kurtosis are shown in figures 4.14 - 4.16 with selected modeled distributions. For the streamwise velocity component in Fig. 4.14, the $\alpha = 1.9$ curve is shown to match areas corresponding to the suction wall ($y = 0$) and portions of the pressure region while the $\alpha = 3.3$ curve more closely matches the suction side. The large magnitude difference between the two α values is not ideal and significant portions of the DNS curve are not represented by either modeled distribution.

In the skewness-kurtosis diagram for the wall-normal velocity (Fig. 4.15), it is demonstrated that the modeled distributions have very poor correlation with the DNS curve and only a portion of the pressure side ($K_v > 5$) is represented by the range covered by $\alpha = 2.2 - 3.3$. For Fig. 4.16, the quadratic model well approximates the pressure region using the coefficient range of $\alpha = 3.0 - 3.7$ but cannot accurately model the near-wall region on the suction side ($K_w > 4$). Similar to case A ($Ro_b = 0$), the near-wall event of large spanwise kurtosis increases coupled with minor skewness changes causes significant modeling inaccuracies.

The selected values for case B ($Ro_b = 0.2$) deviate significantly from the idealized coefficients for case A ($Ro_b = 0$) and coefficients sets proposed by Alberghi et al. (2002) and Tampieri et al.

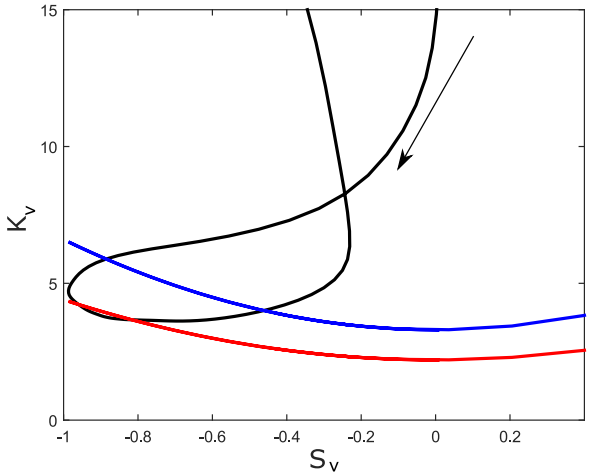

Figure 4.15: Skewness vs. kurtosis distributions for the wall-normal velocity component for simulation case B ($Ro_b = 0.2$). Black line: DNS; Red line, $\alpha = 2.2$; Blue line, $\alpha = 3.3$. Arrow indicates increasing y.

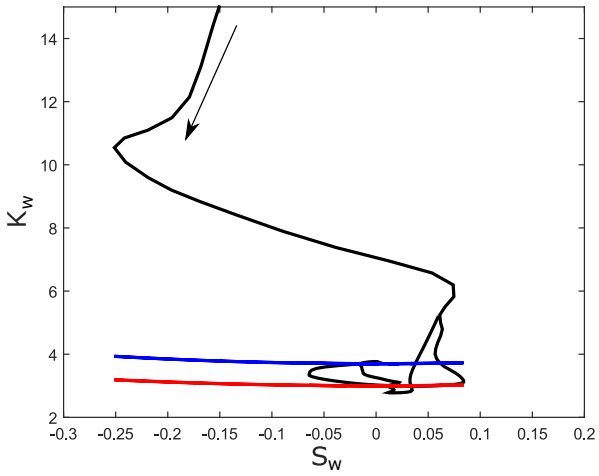

Figure 4.16: Skewness vs. kurtosis distributions for the spanwise velocity component for simulation case B ($Ro_b = 0.2$). Black line: DNS; Red line, $\alpha = 3.0$; Blue line, $\alpha = 3.7$. Arrow indicates increasing y.

(2000). Despite α coefficients being selected for skewness-kurtosis curves which displayed best agreement with the DNS, the modeled distributions showed major inaccuracies most prominently near the suction wall. The near-wall increases of kurtosis in the suction region, resulting from decreased Reynolds stress amplitudes used for higher-order moment normalization, causes the quadratic approximation of kurtosis as a function of skewness to fail in the presence of rotational effects.

4.3.3 Generalized Higher-Order Model

Here the DNS data will be used to evaluate a closure which parameterizes the third and fourth-order moments as functions of the heat flux ($\overline{v'\theta'}$), vertical velocity variance ($\sigma_v^2 = \overline{v'v'}$), temperature variance ($\sigma_\theta^2 = \overline{\theta'\theta'}$), and the velocity and temperature skewness (S_v and S_θ). A simple set of third and fourth-order closures is given by (Gryanik and Hartmann, 2002, Zilitinkevich et al., 1999)

$$\overline{v'^2\theta'} = a_1 S_v \sigma_v \overline{v'\theta'} - K_1 \frac{\partial \overline{v'\theta'}}{\partial y} \tag{4.22a}$$

$$\overline{v'\theta'^2} = a_2 S_\theta \sigma_\theta \overline{v'\theta'} - K_2 \frac{\partial \overline{\theta'^2}}{\partial y} \tag{4.22b}$$

$$\overline{v'^4} = a_3 \left(1 + d_3 S_v^2\right) \sigma_v^4 \tag{4.22c}$$

$$\overline{\theta'^4} = a_4 \left(1 + d_4 S_\theta^2\right) \sigma_\theta^4 \tag{4.22d}$$

$$\overline{v'^3\theta'} = a_5 \left(1 + d_5 S_v^2\right) \sigma_v^2 \overline{v'\theta'} \tag{4.22e}$$

$$\overline{v'\theta'^3} = a_6 \left(1 + d_6 S_\theta^2\right) \sigma_\theta^2 \overline{v'\theta'} \tag{4.22f}$$

The third-order moments include a form of down-gradient diffusion of second-order moments. Zilitinkevich et al. (1999) proposed

$$a_1 = 1 \tag{4.23a}$$

$$a_2 = 1 \tag{4.23b}$$

$$K_1 = C_k K_{v\theta} \tag{4.23c}$$

$$K_2 = 0 \tag{4.23d}$$

where $C_k = 0.1$ and $K_{v\theta} = 0.2\tau_Z\sigma_v^2$. The characteristic time τ_Z was parameterized as $\tau_Z = k/\varepsilon$. Gryanik and Hartmann (2002) instead related the diffusivities to the kinetic energy by

$$K_i = d_i\sqrt{k}y_i \tag{4.24}$$

for $i = 1,2$ (note that y_i refers to the inversion height).

Gryanik and Hartmann (2002) argue that, in the limit that skewness goes to zero, the fourth-order statistics should approach Gaussian behavior. This implies $a_i = 3$ for $i = 3-6$. For turbulence with large skewness, the coefficient $a_i d_i$ should approach 1. So, $d_i = 1/3$ for all fourth-order moments.

To assess the ability of the above closures to correctly parameterize high-order moments, Gryanik and Hartmann (2002) use the explained variance to quantify the difference between the modeled moment and the actual moment:

$$\sigma_f^2 = 1 - \frac{\overline{(y_i - f(x_i))^2}}{\overline{(y_i - \overline{y})^2}} \tag{4.25}$$

Actual measurements are given by y_i while the parameterization is given by $f(x_i)$. The overbar denotes an averaged quantity. To account for the clustering of mesh points in the near-wall region, the explained variance is redefined for this work as an integral over the channel:

$$\sigma_f^2 \equiv 1 - \frac{\int_0^{L_y} (y_i - f(x_i))^2 \, \mathrm{d}y}{\int_0^{L_y} (y_i - \overline{y})^2 \, \mathrm{d}y} \tag{4.26}$$

where y_i are values from the DNS and $f(x_i)$ are, once again, the corresponding model predictions. The mean $\overline{y}$ is computed by

$$\overline{y} = \frac{1}{L_y} \int_0^{L_y} y_i \, \mathrm{d}y \tag{4.27}$$

The definition in Eq. 4.26 eliminates the bias associated with the clustering of meshpoints at the boundaries. Explained variance was used to find optimal modeled coefficient values of a_i and d_i associated with the largest explained variance.

It must be noted that for coefficients K_1 and K_2 proposed by Gryanik and Hartmann (2002) in equation 4.24, the inversion height (y_i) for the turbulent Ekman layer is defined as the wall-normal coordinate where the wall-normal turbulent heat flux ($\overline{v'\theta'}$) distribution reaches a minimum value. However the turbulent wall-normal heat flux associated with turbulent channel flow does not display this property as its distribution instead maintains a minimal value over a large section of the channel. Rotational dynamics do not alter this aspect of the heat flux distribution. Consequently for model testing, y_i was first varied to find an optimum value associated with the largest explained variance for cases *A*-*D*. The optimized y_i values were 0.15 for case *A* ($Ro_\mathrm{b} = 0$), 0.01 for case *B* ($Ro_\mathrm{b} = 0.2$) and 0 for cases *C* ($Ro_\mathrm{b} = 0.5$) and *D* ($Ro_\mathrm{b} = 0.9$).

For case *A* ($Ro_\mathrm{b} = 0$), the contour plots in Fig. 4.17(a) and (b) show the explained variance for $\overline{v'^2\theta'}$ and $\overline{v'\theta'^2}$, respectively. The black circles correspond to values of a_i and d_i which maximize the explained variance in relation to the DNS data; the red circles give values proposed by Gryanik and Hartmann (2002) and the blue circles correspond to coefficients recommended by Zilitinkevich et al. (1999). For a_1 and d_1, the values which match the DNS are respectively larger and smaller than both recommended values. The ranges of optimal values for a_2 and d_2 in Fig. 4.17(b) are demonstrated to be significantly smaller than the range in Fig. 4.17(a) and differ significantly from the coefficient sets of Gryanik and Hartmann (2002) and Zilitinkevich et al. (1999) with respect to a_2. The maximum explained variances associated with $\overline{v'^2\theta'}$ and $\overline{v'\theta'^2}$ are 0.8362 and 0.3295, respectively, which demonstrate poor model fit with the DNS data.

The contour plots for fourth-order moments are shown in Fig. 4.18 with optimal coefficients

plotted alongside the recommended coefficients of Gryanik and Hartmann (2002) and Zilitinkevich et al. (1999). Obtained optimum values of a_i and d_i show significant differences from the recommended coefficients although no outstanding trends are observed. Disparity in the a_i coefficients appears to be more common than for d_i. The diagram of Fig. 4.18(c) for $\overline{v'^3\theta'}$ shows the worst model performance among the fourth-order moments with a maximum explained variance of 0.8958. Although this value is not ideal, model agreement with fourth-order moments is significantly greater than demonstrated for third-order moments.

For case A ($Ro_\mathrm{b} = 0$), the DNS data vs. modeled predictions is plotted with unity for third-order order moments $\overline{v'^2\theta'}$ and $\overline{v'\theta'^2}$ in Fig. 4.19(a) and (b), respectively. The friction velocity (v_*) and temperature (θ_*) were used to scale the high-order moments. The optimum coefficients a_i and d_i found in Fig. 4.17 are demonstrated to do a poor job at modeling DNS results. The optimized modeled distributions are also plotted against DNS and modeled profiles using coefficients proposed by Gryanik and Hartmann (2002) and Zilitinkevich et al. (1999) in Fig. 4.20. The big "sine"-like difference between unity and case A ($Ro_\mathrm{b} = 0$) data in Fig. 4.19(a) is demonstrated to be a result of incorrect model approximations of the maximum peak locations in the log-law regions. The smaller "eight"-shaped deviation from unity in Fig. 4.19(a) results from additional inaccuracy in the viscous sublayer region near both walls. As expected from Fig. 4.19(b), the modeled distributions are shown to have poor accuracy throughout the entire channel.

For case A ($Ro_\mathrm{b} = 0$), the DNS data vs. modeled predictions for fourth-order order moments are displayed in Fig. 4.21 and modeled distributions are shown with predictions by Gryanik and Hartmann (2002) and Zilitinkevich et al. (1999) in Fig. 4.22. The generalized model performs well in figures 4.21(a), (b) and (d). Some deviation is shown for $\overline{v'^3\theta'}$ in Fig. 4.21(c), which is demonstrated in Fig. 4.22(c) to stem from slight over-predictions of the twin peak amplitudes and under-prediction of centre channel region amplitudes. The relative inaccuracy of the generalized closure model in approximating third-order moments compared to fourth-order moments may be attributed to specialized coefficient tuning for third-order moments.

Similar analysis to case A ($Ro_\mathrm{b} = 0$) is performed for cases B-D. Contours of sampled a_i and

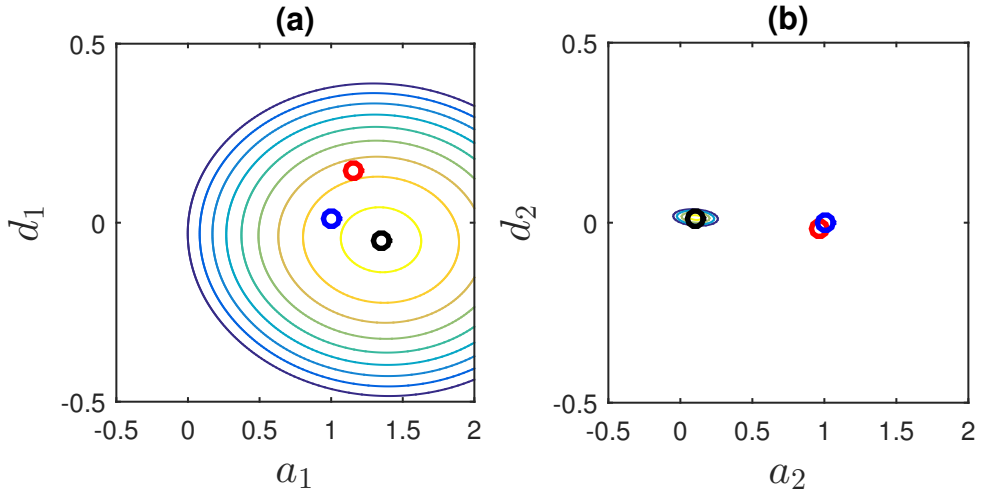

Figure 4.17: Calculation of empirical constants for third-order distributions. a) $\overline{v'^2\theta'}$; b) $\overline{v'\theta'^2}$. Contours give explained variance as calculated by Eq. 4.26. Contour interval is $\Delta = 0.1$ for the contours (minimum of $\sigma_f^2 = 0.1$) Black circles: Case A ($Ro_b = 0$); Red circles: Gryanik and Hartmann (2002); Blue circles: Zilitinkevich et al. (1999).

Table 4.1: Coefficients for third and fourth-order moment closures with corresponding maximum explained variance: Best-fit for rotating turbulent channel flow cases A-D.

a_i, d_i	A	B	C	D	$\sigma_f^2\big\|_A$	$\sigma_f^2\big\|_B$	$\sigma_f^2\big\|_C$	$\sigma_f^2\big\|_D$
a_1	1.347	1.221	1.397	1.681	0.8362	0.6010	0.6515	0.6999
d_1	-0.04774	-0.304	-0.098	0.00251				
a_2	0.103	0.5427	0.4673	0.4322	0.3295	0.1759	0.4765	0.6516
d_2	0.01256	-0.06784	0.00251	0.00251				
a_3	3.487	2.794	2.432	2.538	0.9859	0.9945	0.9979	0.9991
d_3	0.00503	0.146	1.06	1.161				
a_4	2.492	2.251	2.613	3.095	0.9309	0.9992	0.9957	0.9958
d_4	1.186	0.809	1.01	0.7085				
a_5	3.095	3.503	2.749	2.643	0.8958	0.9639	0.9746	0.9838
d_5	0.2563	0.00503	0.3568	0.5578				
a_6	2.734	2.327	3.126	3.623	0.9880	0.8501	0.8456	0.9769
d_6	0.4322	0.8501	0.1558	0.00503				

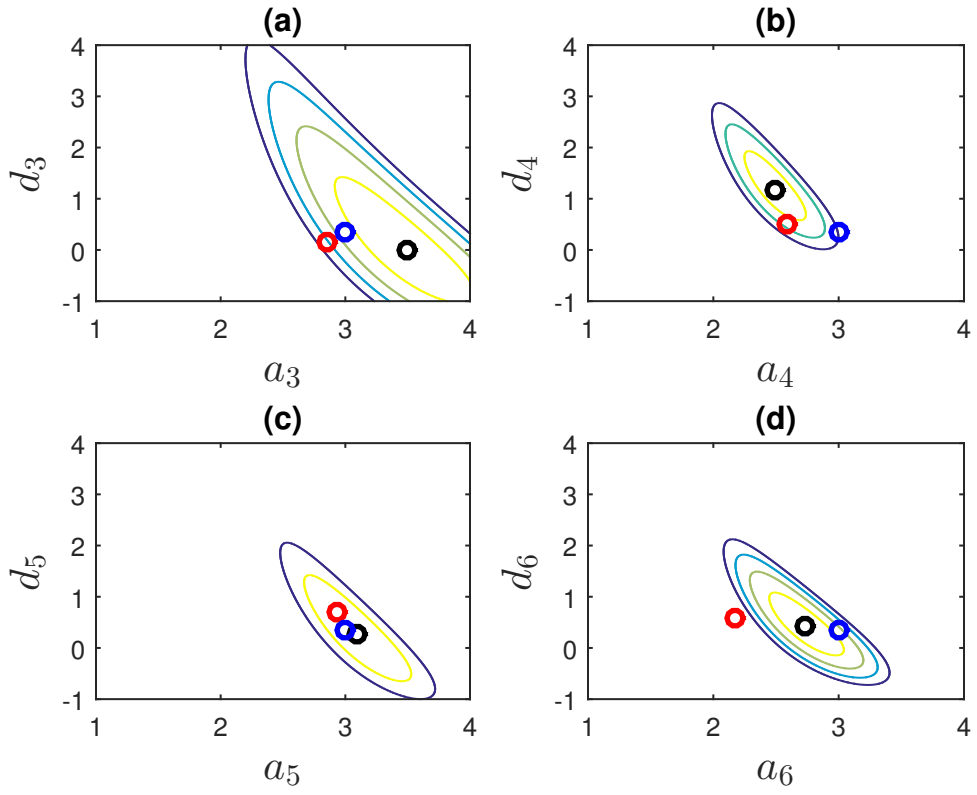

Figure 4.18: Calculation of empirical constants for fourth-order distributions. a) $\overline{v'^4}$; b) $\overline{\theta'^4}$; c) $\overline{v'^3\theta'}$; d) $\overline{v'\theta'^3}$. Contours give explained variance as calculated by Eq. 4.26. Contour interval is $\Delta = 0.05$ for the contours (minimum of $\sigma_f^2 = 0.8$). Black circles: Case A ($Ro_b = 0$); Red circles: Gryanik and Hartmann (2002); Blue circles: Zilitinkevich et al. (1999).

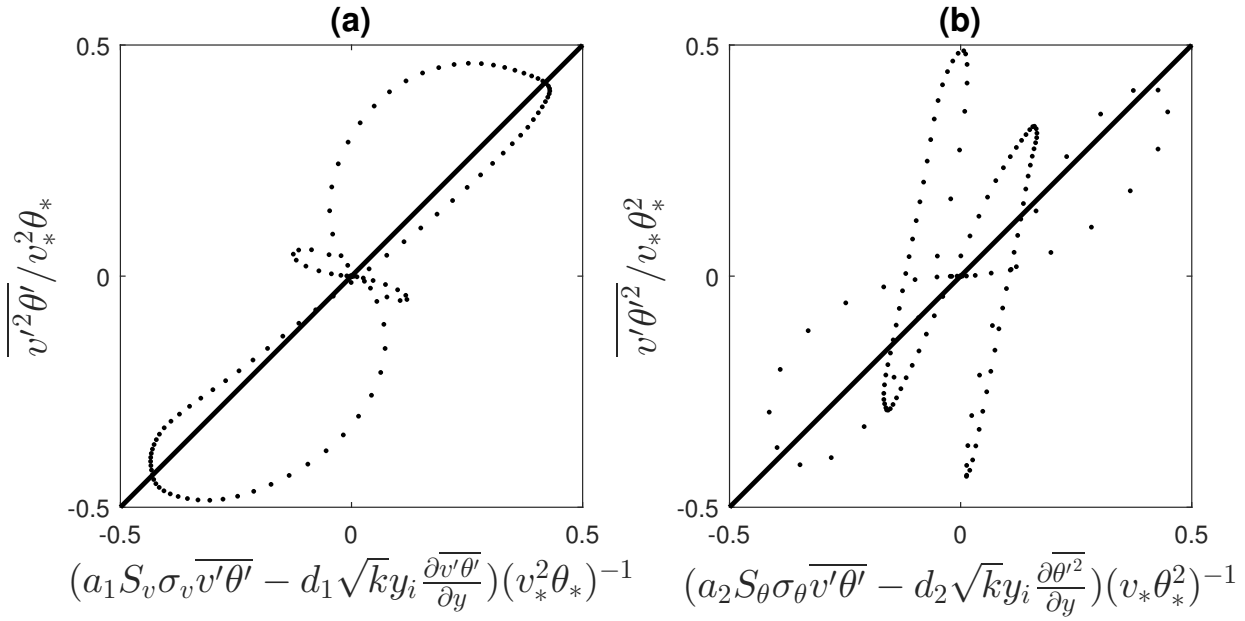

Figure 4.19: Third-order moment: (a) $\overline{v'^2\theta'}$, $a_1 = 1.347$, $d_1 = -0.04774$, $\sigma_f^2 = 0.8362$; (b) $\overline{v'\theta'^2}$, $a_2 = 0.103$, $d_2 = 0.01256$, $\sigma_f^2 = 0.3295$. Dots are Case A ($Ro_\mathrm{b} = 0$) data and the line is unity.

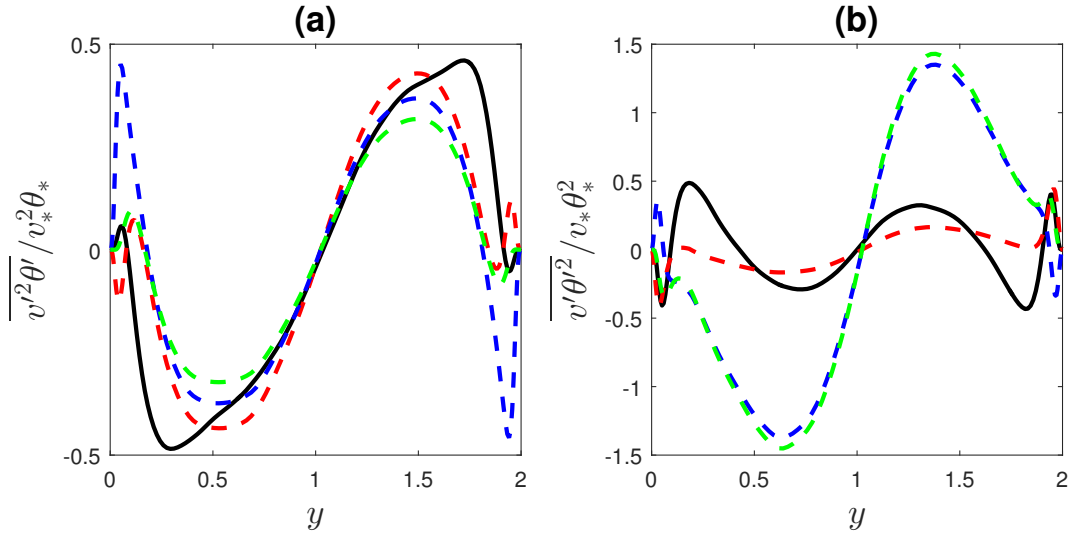

Figure 4.20: Modeled third-order distributions with DNS for Case A ($Ro_\mathrm{b} = 0$). a) $\overline{v'^2\theta'}$; b) $\overline{v'\theta'^2}$. Black: Case A ($Ro_\mathrm{b} = 0$); Red: Optimal coefficients; Blue: Gryanik and Hartmann (2002); Green: Zilitinkevich (1999).

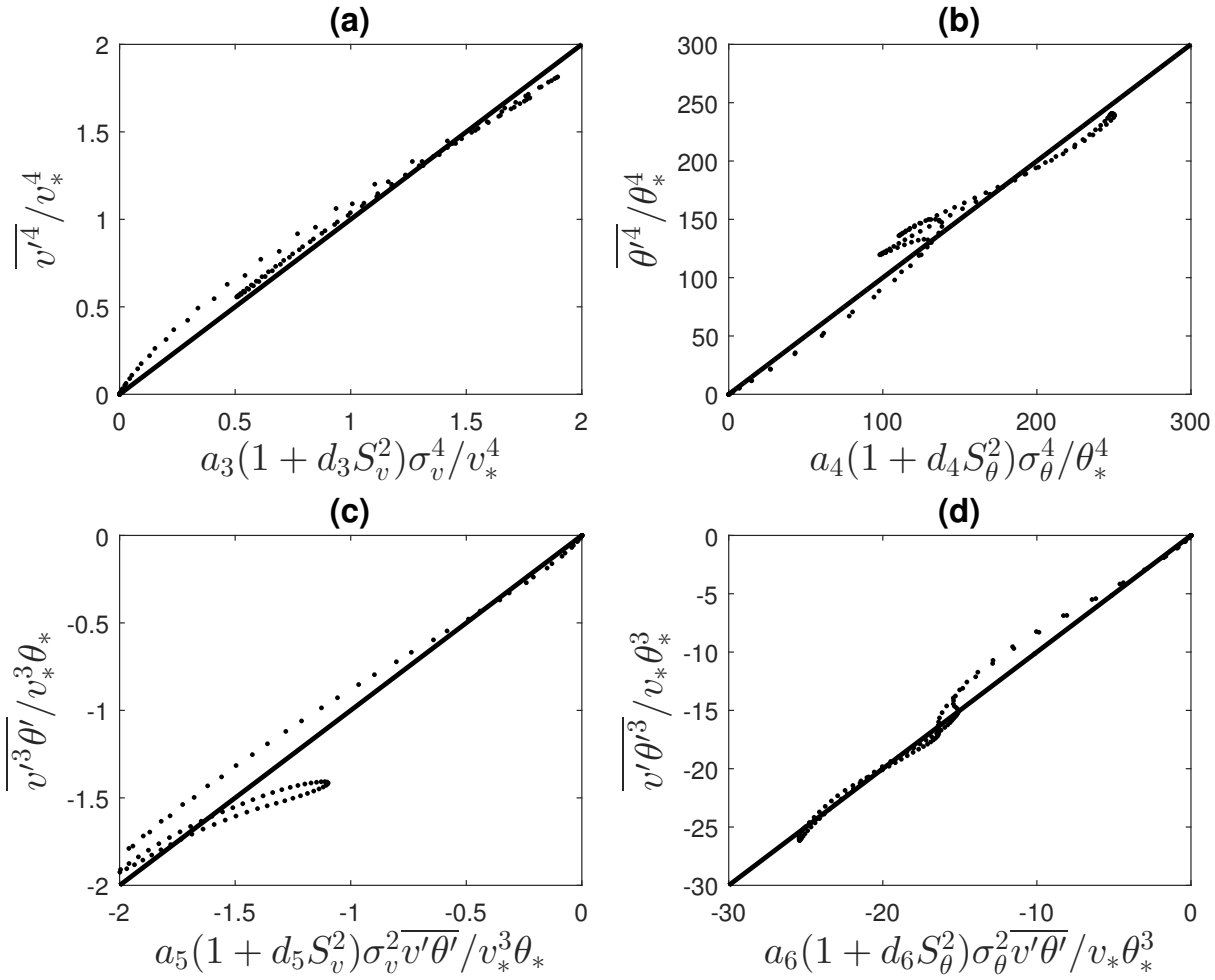

Figure 4.21: Fourth-order moments: (a) $\overline{v'^4}$, $a_3 = 3.487$, $d_3 = 5.03 \times 10^{-3}$, $\sigma_f^2 = 0.9859$; (b) $\overline{\theta'^4}$ $a_4 = 2.492$, $d_4 = 1.186$, $\sigma_f^2 = 0.9309$; (c) $\overline{v'^3\theta'}$, $a_5 = 3.095$, $d_5 = 0.2563$, $\sigma_f^2 = 0.8958$; (d) $\overline{v'\theta'^3}$, $a_6 = 2.734$, $d_6 = 0.4322$, $\sigma_f^2 = 0.9880$. Dots are Case A ($Ro_b = 0$) data and the line is unity.

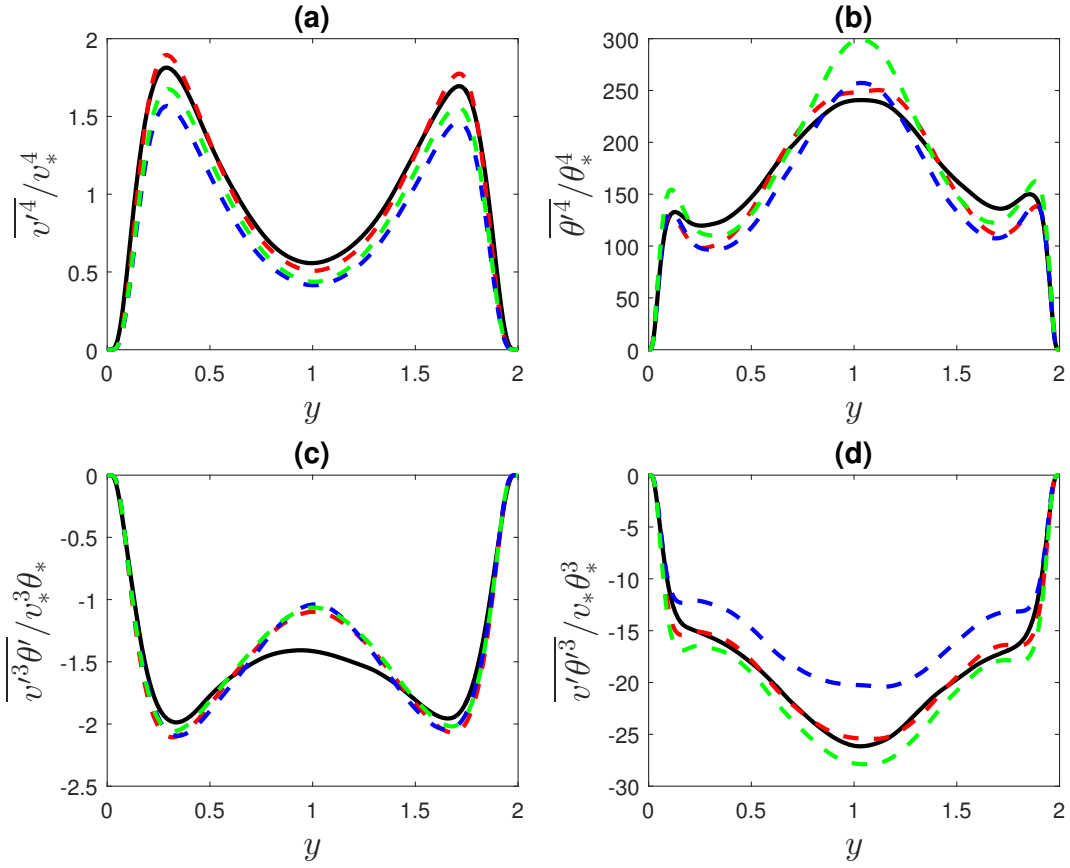

Figure 4.22: Modeled fourth-order distributions with DNS for Case A ($Ro_\mathrm{b} = 0$). a) $\overline{v'^4}$; b) $\overline{\theta'^4}$; c) $\overline{v'^3\theta'}$; d) $\overline{v'\theta'^3}$. Black: Case A ($Ro_\mathrm{b} = 0$); Red: Optimal coefficients; Blue: Gryanik and Hartmann (2002); Green: Zilitinkevich (1999).

d_i were computed for large ranges of values and optimal coefficients corresponding to maximum explained variance were selected, the resulting modeled distributions were then compared to the DNS data. The recommended coefficients of a_i and d_i along with the maximum explained variance are summarized for the six higher-order moments in table 4.1 for all rotating turbulent channel flow cases.

Rotation is demonstrated in table 4.1 to have significant effects on the optimal model coefficients and maximum explained variance for both third and fourth-order moments. The model produces a poorer approximation for $\overline{v'^2\theta'}$ in the rotational cases compared to case A ($Ro_b = 0$). For the rotational cases, the best-fit a_1 values are observed to steadily increase as a function of rotation number and the best-fit d_1 coefficients also display this trend. The optimal a_2 coefficient is shown to decrease for increasing rotation number. Although the model showed significant σ_f^2 increases as the rotation rate increased, the model showed poor performance for $\overline{v'\theta'^2}$ and demonstrated large inaccuracies for third-order moments in regards to spanwise-rotating turbulent channel flow.

In table 4.1 for rotational cases B-D, it is observed that the generalized model holds significantly greater accuracy for fourth-order moments than third-order moments. Rotational effects resulted in better modeled approximations of $\overline{v'^4}$ and $\overline{\theta'^4}$ ($\sigma_f^2 > 0.99$). Observation of coefficient trends showed increases of a_4 and d_3 with higher rotation number. For $\overline{v'^3\theta'}$, the model was also demonstrated to have better performance for higher rotation number although its maximum explained variance reached 0.9838 in case D ($Ro_b = 0.9$). In contrast, modeled approximations for $\overline{v'\theta'^3}$ displayed decreased accuracy for the rotational cases in comparison to case A ($Ro_b = 0$). A higher rotation number was shown to increase the maximum explained variance similar to model approximations of $\overline{v'\theta'^2}$ and the model displayed reasonable accuracy for $\overline{v'\theta'^3}$ in case D ($Ro_b = 0.9$).

The effectiveness of the generalized model in approximating tested fourth-order moments for spanwise-rotating turbulent channel flow demonstrates possible universal relevance for the model beyond its development for the turbulent Ekman layer. Similar to the basic turbulent quantities of mean velocity and Reynolds stresses, asymmetry is observed in the distributions

of higher-order moments as a consequence from rotational effects. The shift of peak amplitudes for v'_{rms} to the pressure region and T'_{rms} to the suction region has been well-documented in the direct numerical simulation studies of Grundestam et al. (2008) and Liu and Lun (2007), respectively. Correspondingly, moments dominated by v' and θ' are demonstrated to shift towards the pressure and suction walls, respectively. The generalized closure model displayed great accuracy in modeling these rotational effects on fourth-order moments, even showing increased accuracy for most high-order moments compared to the non-rotational case.

4.3.4 Summary

Higher-order moments for turbulent channel flow subject to spanwise rotation were assessed for two closure models. The kurtosis closure model proposed by Mole and Clarke (1995) and the generalized higher-order moment model proposed by Gryanik and Hartmann (2002), Zilitinkevich et al. (1999) were evaluated using DNS data for effectiveness in modeling rotation. It was demonstrated that the kurtosis model using selected best-fit coefficients, similar to those proposed by Tampieri et al. (2000), produced accurate distributions with exception of the near-wall region for spanwise and wall-normal velocity. In the case of rotation, the model failed to generate good approximations for any set of coefficients and the quadratic approximation of kurtosis as a function of skewness was a poor-fit. Parametric studies using explained variance were conducted to obtain optimal coefficients for the generalized closure model. For non-rotation, it was demonstrated that the model was highly inaccurate for tested third-order moments but generally accurate for tested fourth-order moments. Rotation was shown to decrease the accuracy of third-order moments but enhance the accuracy of most fourth-order moments.

Chapter 5

Control of Turbulent Flows

5.1 Overview

The present work considers passive flow control methods using phononic subsurfaces which are dynamic material systems composed of components with spatially varying material or geometric properties. Phononic subsurfaces exhibit frequency-dependent dynamic properties and the development of phononic crystals for control of vibrational waves relies on the attenuation or propagation of specific frequencies, which commit either destructive or constructive interference on the transmitted waves (Hussein et al., 2015). The terms ”stop band” and ”pass band” refer to attenuating and propagating specific frequency ranges, respectively. Subsequently, a phononic crystal structure can be designed such that a range of excitation frequencies would not be allowed to propagate through the structure. In our computational models for flow control, a phononic subsurface replaces a portion of the bottom wall in the channel flow as shown in figure 5.1 in order to interact with the flow field.

Within the bounds of the phononic structure at the lower channel wall, a fluid/structure interaction problem is solved at every time step of the flow control simulations. To couple the fluid and solid systems, the stresses and velocities are required to match at the interface. A conventional serial staggered (CSS) procedure is used at the interface where the pressure acts on the structure as a force and the resulting wall-normal displacements are imposed as flow field boundary conditions at the interface.

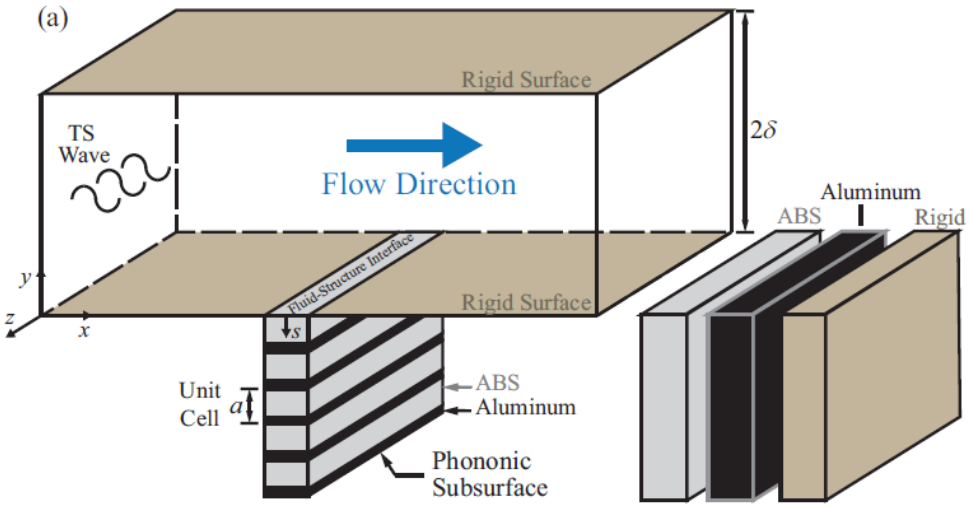

Figure 5.1: Schematic of plane channel flow with a phononic subsuface covering a segment (Hussein et al., 2015).

5.2 Fluid-Structure Interaction (FSI) Simulation Model

The resolution of the control simulations in Hussein et al. (2015) was $200 \times 97 \times 128$ in the streamwise, wall-normal and spanwise directions, respectively. In the coupled model, a portion of the bottom wall of the channel was replaced by the phononic subsurface structure covering a streamwise distance spanning from x_s to x_e. In the current simulations, x_s and x_e were 3.0927δ and 4.6706δ, respectively. The streamwise size and location of the phononic subsurface structure was kept constant from previous flow control simulations for two-dimensional disturbances as it corresponded to a one-quarter wavelength of the primary Tollmien-Schlicting disturbance wave (Kucala and Biringen, 2014). The buffer domain length was 50 percent of the total channel length to prevent reflections at the outflow boundary.

The materials composing the phononic subsurface unit cells were as in Hussein et al. (2015), aluminium and ABS polymer. The density (ρ) and Young's modulus (E) for aluminium are $\rho_{Al} = 2700\frac{kg}{m^3}$ and $E_{Al} = 68.8$ GPa; the respective quantities for ABS polymer are $\rho_{ABS} = 1040\frac{kg}{m^3}$ and $E_{ABS} = 2.4$ GPa. The phononic subsurface structure as a whole consisted of ten unit cells with a total length of $l = 4$ meters.

At each iteration for the control simulations, the dimensional wall pressure (equation 5.1) was calculated on the streamwise midpoint on the fluid-structure interface

$$p_w = p\rho_f U_c^2 \tag{5.1}$$

where p and ρ_f are the dimensional pressure and fluid density, respectively. The pressure acts on the subsurface structure as a force, resulting in a displacement ($\eta(0,t)$) and velocity ($\dot{\eta}(0,t)$). The flow-field boundary conditions were then set using the following equations

$$u(x_s \leq x \leq x_e, y = 0, z, t) = -\eta(0,t)\frac{\partial u_b}{\partial y} \tag{5.2}$$

$$v(x_s \leq x \leq x_e, y = 0, z, t) = \dot{\eta}(0,t) \tag{5.3}$$

In previous work (Hussein et al., 2015), phononics structure designs have been successfully implemented to significantly suppress the amplification of Tollmien-Schlicting (TS) waves in transitional turbulence. When the frequency of the TS instability wave was greater than the truncation frequency of the phononic subsurface structure within the stop band limits, the wave was shown to stabilize with a significant loss of total energy compared to an un-controlled wave. A similar approach was applied to investigate the effectiveness of phononic subsurface control on fully-developed turbulent channel flow. However, the current structures are one-dimensional and are limited in their ability to mitigate waves across a broad frequency spectrum; hence turbulent kinetic energy was not expected to be significantly mitigated due to the wide range of scales and frequencies operating within fully developed turbulence. Future designs exhibiting a broader design space are more applicable for flow control of turbulence. Higher-dimensional phononic structures will be of special use due to the added ability to target a wider frequency range which would ultimately affect a spanwise wavenumber range (k_3) which corresponds to the propagating plane waves proposed by Sirovich et al. (1990). However, some promising results were discovered concerning the reduction of energy using the current one-dimensional phononic subsurface configurations despite the structural limitations.

5.3 Control Simulation Results and Analysis

Flow control simulations using two phononic subsurface designs were conducted. The first control simulation $S1$ used a unit cell which consisted of a layer of ABS polymer (90 percent volume fraction) and a layer of aluminium (10 percent volume fraction). The second control simulation $S2$ used a unit cell which consisted of a single layer of ABS polymer (100 percent volume fraction). Based on the tenets of phononic subsurface theory (Hussein et al., 2015), design $S2$ was tuned to exhibit more favorable phase and amplitude properties for the reduction of energy in a turbulent flow field than design $S1$. The details of the phononic subsurface control designs are beyond the scope of this dissertation but are under further current investigation by researchers at the Hussein Group at CU-Boulder.

Results from the control simulations are shown in figure 5.2 which displays the streamwise spatial distributions in the $y^+ = 0.06$ plane of the normalized percentage differences of turbulent kinetic energy between each control design and the rigid-wall case: $100 \times \frac{KE_{control} - KE_{rigid}}{KE_{rigid}}$. Hence positive and negative values denote flow de-stabilization and stabilization, respectively.

In figure 5.2, the presence of the phononic subsurface within the slot marked by dashed lines is expressively demonstrated through the immediate decline in turbulent kinetic energy upon nearing the slot for both passive control designs; significant downstream effects were also observed as maximum flow stabilization was located in the region following the slot. The application of control design $S2$ was observed to result in a stronger reduction in energy than the application of control design $S1$, demonstrating remarkable adherence to phononic subsurface theory. One caveat of these results is the small amplitudes of the turbulent kinetic energy reductions (a maximum reduction of 0.6 percent was observed for case $S1$) but is a consequence of the one-dimensionality of the phononic subsurface unit cell which is limited in its performance. In the future, multi-dimensional phononic designs will circumvent this problem and will likely show much more significant turbulent kinetic energy reductions, which would lead to the suppression of multiple k_3 wavenumbers.

In order to analyze how the phononic subsurface structures are affecting the physics of the turbulent flow field, a quadrant analysis was completed to examine the control structure effects on the second and fourth quadrant event contributions which relate to the powerful turbulence generation cycle. In figures 5.3(a)-(d), the streamwise spatial distributions of the normalized percentage differences between the control designs and the rigid wall case (similar to figure 5.2) are shown in the $y^+ = 0.06$ plane for the four different quadrants $Q1$-$Q4$. In figures 5.3(b) and (d), the second and fourth quadrant distributions generally follow the same trends as the overall turbulent kinetic energy distributions shown in figure 5.2, demonstrating that the phononic subsurface structures are suppressing the ejection and sweep events which compose the turbulence generation cycle. Conversely, the first and third quadrant distributions in figures 5.3(a) and (c) generally demonstrated flow de-stabilization.

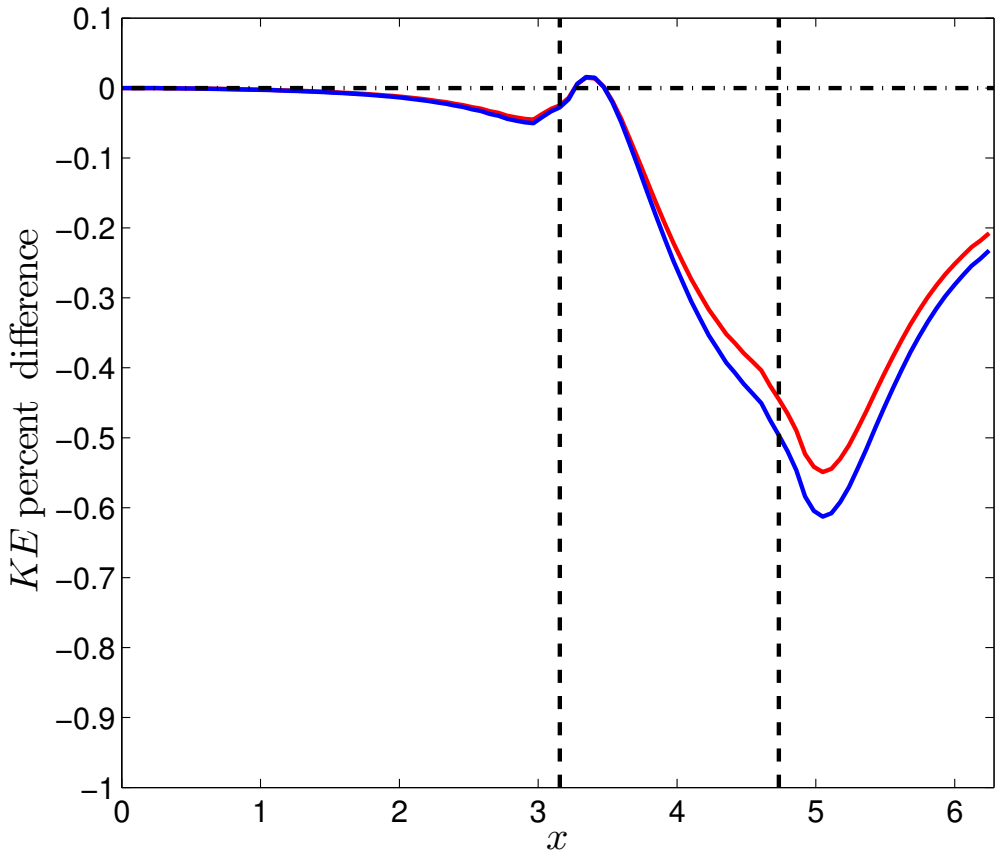

Figure 5.2: Spatial streamwise distributions of the percentage change in kinetic energy for the control simulations cases *S*1 and *S*2 as compared to the rigid wall simulation case *S* at the $y^+ = 0.06$ plane. Red: case *S*1; blue: case *S*2. The dashed black lines denote the location of the slot.

However, the first and third quadrant contributions did display reductions of turbulent kinetic energy in the regions downstream and slightly upstream of the slot despite the slot showing flow de-stabilization for both control cases. Similarly, the second and fourth quadrant contributions showed some initial flow de-stabilization in the region near the front edge of the slot, demonstrating that edge effects for the phononic subsurfaces are very significant and produce different flow dynamics along the streamwise direction. It should be noted that due to the second and fourth quadrant contributions to turbulent kinetic energy being an order of magnitude greater than the first and third quadrant contributions, reduction of overall turbulent kinetic energy is observed consistently throughout the channel. The location of maximum flow stabilization in figure 5.2 is a consequence of all quadrant contributions showing energy reductions in that region.

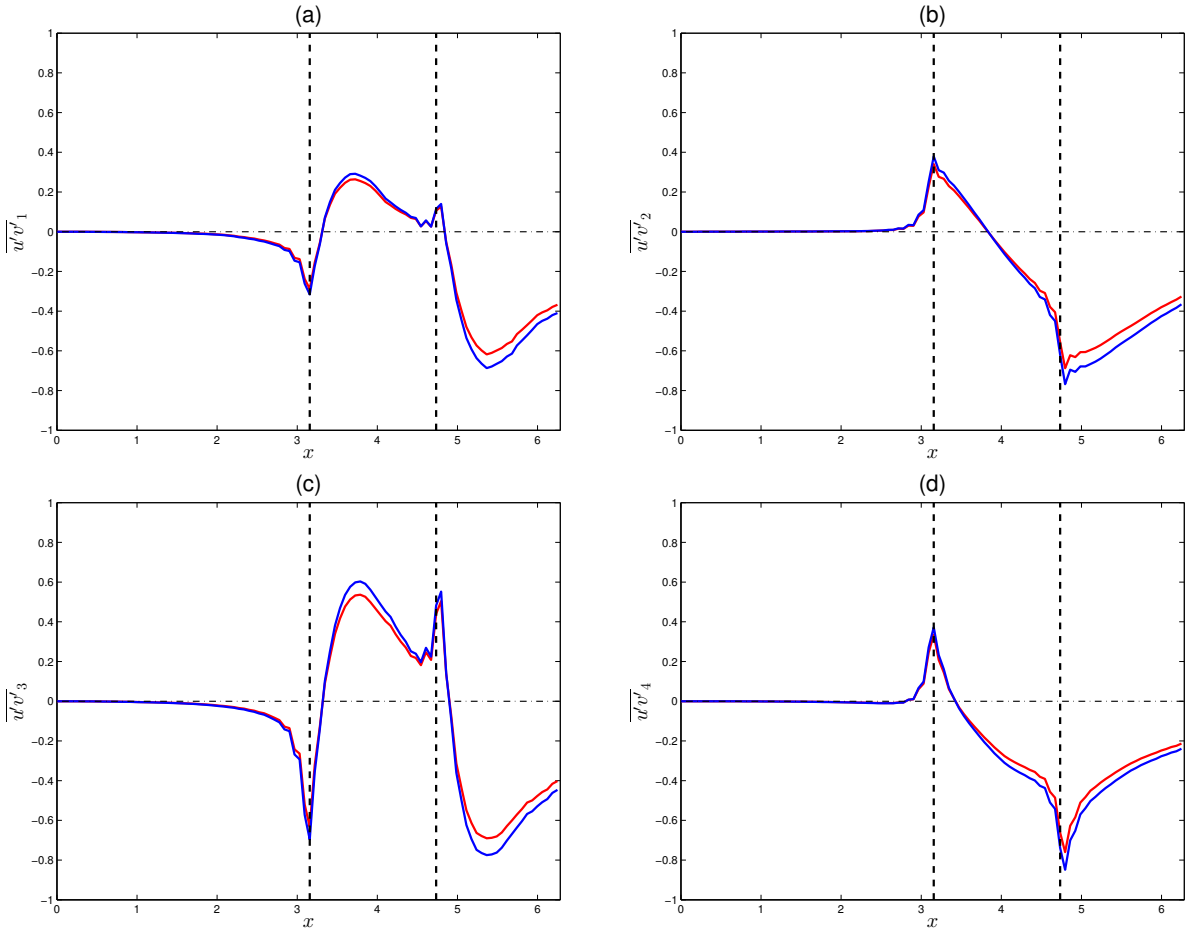

Figure 5.3: Spatial streamwise distributions of the percentage change in kinetic energy contribution from various quadrants for the control simulations cases $S1$ and $S2$ as compared to the rigid wall simulation case S at the $y^+ = 0.06$ plane. a) Q1; b) Q2; c) Q3; d) Q4. Red: case $S1$; blue: case $S2$. The dashed black lines denote the location of the slot.

Chapter 6

Conclusion

6.1 Overview

The focus of this thesis was to investigate in detail the dynamics of turbulence in simple and complex turbulent flows, primarily with regards to understanding the contributions of coherent structures to the turbulence generation cycle and the ability of closure models to accurately approximate turbulence. In ascertaining the interactions and roles of energetical structures as well as their relationships with intercomponent energy transfer and overall turbulent kinetic energy, the underlying complex mechanisms behind turbulence are better understood and can be applied towards flow control of turbulence. The examination of turbulence and heat transfer closures also assists this goal as in addition to attaining significant reductions of computational costs, the understanding of intercomponent energy transfer and turbulence production is crucial within model design and improvement. With the results of these investigations, this collective knowledge of turbulence has been applied towards passive flow control techniques using phononic structures for the reduction of turbulent kinetic energy.

6.2 Contributions

Research from the present work has been presented in the following scientific conferences and journals.

Conference Presentations:

- Hsieh, A., Biringen, S. and Kucala, A. "Use of DNS Data to Evaluate Closure Models for Spanwise-Rotating Turbulent Channel Flow." Bulletin of the American Physical Society - DFD13-2013-000875. Pittsburgh, Pennsylvania, 2013.

- Hsieh, A., Biringen, S. and Kucala, A. "Evaluation of Turbulence Closure Models for Rotating Turbulent Channel Flow." International Conference on Computational Heat and Mass Transfer. Istanbul, Turkey, 2015.

- Hsieh, A. "The Minimal Flow Unit in Rotating Wall-Bounded Turbulence." Boulder Fluids Seminar. University of Colorado-Boulder, 2015.

- Hsieh, A. "DNS of Rotational Turbulence: Structures and MFU Design." Sandia Conference. University of Colorado-Boulder, 2015.

Journal Manuscripts:

- Hsieh, A., Biringen, S., and Kucala, A. "Simulation of rotating channel flow with heat transfer: evaluation of closure models." J. Turbomach. 138:111009. pp. 1-15. 2016.

- Waggy, S.B., Hsieh, A. and Biringen, S. "Modeling high-order statistics in the turbulent Ekman layer." Geophysical and Astrophysical Fluid Dynamics. 5:391-408. 2016.

- Hsieh, A. and Biringen, S. "The minimal flow unit in complex turbulent flows." Phys. Fluids. 28:125102. pp. 1-18. 2016.

- Hsieh, A. and Biringen, S. "Effects of Rotation on Turbulence Production" J. Fluid Mech. pp. 1-38. 2017. (Submitted)

- Hsieh, A. and Biringen, S. "Modeling high-order statistics in spanwise-rotating turbulent channel flow." J. Turbomach. 2017. (In preparation)

Contributions:

- Demonstrated the validity of the theoretical models proposed by Landahl (1990) and Lengani and Simoni (2015) using turbulent channel flow visualizations obtained from direct numerical simulation. The visualizations confirmed the theoretical model predictions made for the formation and structure of sublayer streaks and three-dimensional hairpin vortices in the turbulence generation cycle.

- Developed a specific, new extension of the principal orthogonal decomposition (POD) method to demonstrate the existence of propagating plane waves in a spatial channel model. Despite the targeting of these structures in previous flow control studies by Handler et al. (1993) and Murakami et al. (1992), propagating plane waves have only been previously demonstrated by Sirovich et al. (1990, 1991) using periodic channel models. With a lack of streamwise wavenumber in the spatial model, a new version of the POD method was constructed using a nondimensional frequency for the streamwise number and the creation of a spectral density tensor in both space and time. A conversion for this nondimensional frequency to a spatial-like streamwise wavenumber was conducted for the successful demonstration of these coherent structures in the spatial model. This contribution also resolved concerns from Sirovich et al. (1990) that the streamwise component of these traveling waves were a possible result of insufficient mesh resolution of the periodic model and subsequent mode truncation.

- Discovered the presence of a phase shift between the fluctuating streamwise and wall-normal velocities in the suction region for spanwise-rotating turbulent channel at a low rotation number. Using quadrant analyses, DNS data was examined to find a large-amplitude, quasi-periodic energy contribution from all four quadrants in the suction region of spanwise-rotating turbulent channel flow which replaced the consistent contributions in nonrotational turbulence. The strong velocity correlations related to this quasi-periodic event manifested as a significant phase shift in the analysis of the spectral components from these signals.

- Developed a new minimal flow unit model for rotational turbulence ($Ro_b \leq 0.5$). The minimal flow unit is a desirable computational model which significantly reduces computational costs and has been previously designed for only simple turbulent flows. By performing a similar analysis to the study by Jimenez and Moin (1991) which demonstrated the necessary box size for non-rotating turbulent channel flow was related to sublayer streak width in the near-wall turbulence cycle, a corresponding investigation of rotational turbulence demonstrated the necessity of a minimum box width ($L_z = \pi$) for capturing at least one full pair of Taylor-Gortler vortices (roll cells) to achieve an accurate MFU model. In addition, a unique examination of the MFU model's capability to produce accurate higher-order statistics was conducted and the model demonstrated accurate results in the pressure region but not the suction region. A significant dependence on Reynolds number for MFU accuracy was also discovered.

- Tested a large number of RANS and turbulent heat flux models at high rotation number limits and proposed reasons for the subsequent failure of these models at high rotation rates. An unique investigation into the pressure-strain and pressure-temperature-gradient correlation functions of several explicit algebraic Reynolds stress models (EARSM) and explicit algebraic heat flux models (EAHFM) was conducted which revealed strong need to revise and improve these budget functions.

- Tested two higher-order closure models initially proposed for the turbulent Ekman layer for rotating turbulent channel flow. The kurtosis model completely failed in the presence of rotation but the generalized velocity-temperature model demonstrated strong accuracy for fourth-order moments even at high rotation rates. Optimized coefficients were proposed for non-rotation and rotational cases.

- **Developed a comprehensive strategy for researching the effectiveness of phononic subsurface structures on the stabilization of fully-developed spatially-evolving channel turbulence. Fluid-structure interaction (FSI) simulations using a spatial channel DNS**

code demonstrated that the application of these structures to the bottom channel wall reduced turbulent kinetic energy in turbulent channel flow; the respective reductions between two control designs also demonstrated remarkable adherence to phononic subsurface theory. Post-processing routines were also created to examine the physical changes to the turbulent flow field by the phononic structures, such as quadrant analyses to examine changes to burst and sweep events.

6.3 Ongoing Work

- Demonstrate significant reduction of turbulent kinetic energy within fully turbulent channel flow using new phononic structure designs. These designs will aim to suppress a significantly greater number of energetic modes as opposed to the current designs which are unable to reduce turbulent kinetic energy by large amounts.

- Simulate thermal transport using the spatial channel model and film cooling methods to enhance heat transfer in the near-wall channel regions for turbulent channel flow. High heat transfer coefficients are desirable near the walls for efficient mixing of coolant materials in rotating turbomachinery applications. These simulations will aim to examine the effects of different blowing ratios on local heat transfer coefficients.

Bibliography

K. Abe and K. Suga. Towards the development of a Reynolds-averaged algebraic turbulent scalar-flux model. Int. J. Heat and Fluid Flow, 22:19–29, 2000.

S. Acharya, E. Sethuraman, and S. Nikotopoulos. Mass and heat transfer in rotating, smooth, high aspect ratio coolant channels with curved walls. J. Turbomachinery, 131:1–8, 2012.

R. Adrian. Hairpin vortex organization in wall turbulence. Phys. Fluids, 19:1–16, 2007.

S. Alberghi, A. Maurizi, and F. Tampieri. Relationship between the Vertical Velocity Skewness and Kurtosis Observed during Sea-Breeze Convection. J. of Applied Meteorology, 4:885–889, 2002.

P. Alfredsson and A. Johansson. Turbulence experiments - instrumentation and processing of data. Advances in Turbulence, 2:230–243, 1988.

P. Alfredsson, A. Johansson, and J. Kim. Turbulence production near walls: the role of flow structures with spanwise asymmetry. Center for Turbulence Research Proceedings, 2:131–141, 1988.

R. Barlow and J. Johnston. Structure of turbulent boundary layers on a concave surface. J. Fluid Mech., 65:439–459, 1985.

J. Bayly, S. Orszag, and T. Herbert. Instability mechanisms in shear-flow transition. Annu. Rev. Fluid Mech., 20:359–391, 1988.

G. Berkooz, P. Holmes, and J. Lumley. The proper orthogonal decomposition in the analysis of turbulent flows. Annu. Rev. Fluid Mech., 25:539–575, 1993.

S. Biringen. Three-dimensional vortical structures of transition in plane channel flow. Phys. Fluids, 30:3359–3368, 1987.

S. Biringen and L. Maestrello. Development of spot-like turbulence in plane channel flow. Phys. Fluids, 27:318–321, 1984.

R. Blackwelder and R. Kaplan. On the wall structure of the turbulent boundary layer. J. Fluid Mech., 76:89–112, 1976.

D. Bogard and W. Tiederman. Burst Detection with Single-point Velocity Measurements. J. Fluid Mech., 162:389–413, 1986.

G. Brethouwer, L. Wei, P. Schlatter, and A. Johansson, editors. Turbulence and cyclic bursts in rotating channel flow, number 14 in European Turbulence Conference, Lyon, sept 2013.

D. Bushnell, J. Hefner, and R. Ash. Effect of compliant wall motion on turbulent boundary layers. Phys. Fluids, 20:S31–S48, 1977.

F. Chambers and A. Thomas. Turbulent spots, wave packets and growth. Phys. Fluids, 26:1160–1162, 1983.

Y. Chung and H. Sung. Comparative Study of Inflow Conditions for Spatially Evolving Simulation. AIAA Journal, 35:269–274, 1997.

G. Comte-Bellot, J. Sabot, and I. Saleh. Detection of Intermittent Events Maintaining Reynolds Stress. Proceedings of the Dynamic Flow Conference, 1:213–230, 1978.

L. DeCarlo. On the meaning and use of kurtosis. Psychological Methods, 2:292–307, 1997.

H. Eckelmann. The structure viscous sublayer and adjacent wall region in a turbulent channel flow. J. Fluid Mech., 65:439–459, 1974.

M. Gad-el Hak and H. Tsai. Transition and Turbulence Control. World Scientific, 2006.

S. Girimaji. Fully explicit and self-consistent Reynolds stress model. Theo. Comp. Fluid Mech., 8: 387–402, 1996.

O. Grundestam, S. Wallin, and A. Johansson. An explicit algebraic Reynolds stress model based on a nonlinear pressure strain rate model. Int. J. Heat and Fluid Flow, 26:732–745, 2005.

O. Grundestam, S. Wallin, and A. Johansson. Direct numerical simulations of rotating turbulent channel flow. J. Fluid Mech., 598:177–199, 2008.

V. M. Gryanik and J. Hartmann. A Turbulence Closure for the Convective Boundary Layer Based on a Two-Scale Mass-Flux Approach. J. of Atm. Sci., 59:2729–2744, 2002.

R. Handler, E. Levich, and L. Sirovich. Drag reduction in turbulent channel flow by phase randomization. Phys. Fluids A, 5:686–694, 1993.

T. Herbert. Secondary instability of boundary layers. Annu. Rev. Fluid Mech., 20:487–526, 1988.

M. I. Hussein, K. Hamza, G. Hulbert, and K. Saitou. Optimal synthesis of 2d phononic crystals for broadband frequency isolation. Waves in Random and Complex Media, 17(4) (special issue): 491–510, 2007.

M. I. Hussein, S. Biringen, O. R. Bilal, and A. Kucala. Flow stabilization by subsurface phonons. Proc. R. Soc. A, 471:20140928, 2015.

J. Jimenez and P. Moin. The minimal flow unit in near-wall turbulence. J. Fluid Mech., 225:213–240, 1991.

Y. Kang and K. Choi. Direct intervention of hairpin structures for turbulent boundary-layer control. Phys. Fluids, 20:101517, 2008.

N. Kasagi and K. Nishino. Probing turbulence with three-dimensional particle-tracking velocimetry. Exp Thermal Fluid Sci., 4:601–612, 1991.

H. Kim, S. Kline, and W. Reynolds. The production of turbulence near a smooth wall in a turbulent boundary layer. J. Fluid Mech., 50:133–160, 1971.

J. Kim and P. Spalart. Scaling of the bursting frequency in turbulent boundary layers at low Reynolds numbers. Phys. Fluids, 30:3326–3328, 1987.

J. Kim, P. Moin, and R. Moser. Turbulence statistics in fully developed channel flow at low reynolds number. J. Fluid Mech., 177:133–166, 1987.

S. Kline, W. Reynolds, F. Schraub, and P. Runstadler. The structure of turbulent boundary layers. J. Fluid Mech., 30:741–773, 1967.

M. Kramer. Boundary-layer stabilization by distributed damping. J. Aeronaut. Sci., 24:459–460, 1957.

H. Kreplin and M. Eckelmann. Behavior of the three fluctuating velocity components in the wall region of a turbulent channel flow. Phys. Fluids, 22:1233–1239, 1979.

R. Kristofferson and H. Andersson. Direct simulations of low reynolds number turbulent flow in a rotating channel. J. Fluid Mech., 253:163–197, 1993.

A. Kucala. Control of Transitional and Turbulent Flows Using Direct Numerical Simulation. PhD thesis, University of Colorado, Boulder, 2015.

A. Kucala and S. Biringen. Spatial simulation of channel flow instability and control. J. Fluid Mech., 738:105–123, 2014.

M. Landahl. Wave mechanics of breakdown. J. Fluid Mech., 56:775–802, 1972.

M. Landahl. A note on an algebraic instability of inviscid parallel shear flows. J. Fluid Mech., 98: 243–251, 1980.

M. Landahl. On sublayer streaks. J. Fluid Mech., 212:593–614, 1990.

B. Launder. On the effects of a gravitational field on the turbulent transport of heat and momentum. J. Fluid Mech., 67:569–581, 1975.

B. Launder and B. Shama. Application of the energy-dissipation model of turbulence to the calculation of flow near a spinning disc. Letters in Heat and Mass Transfer, 1:131–138, 1974.

B. Launder, G. Reece, and W. Rodi. Progress in the development of a reynolds stress turbulent closure. J. Fluid Mech., 68:537–566, 1975.

D. Lengani and D. Simoni. Recognition of coherent structures in the boundary layer of a low pressure-turbine blade for different free-stream turbulence intensity levels. Int. J. Heat Fluid Flow, 54:1–13, 2015.

X. Li, J. Ren, and H. Jiang. Film cooling modeling of turbine blades using algebraic anisotropic turbulence models. J. Turbomachinery, 136:1–9, 2014.

N. Liu and X. Lun. Direct numerical simulation of spanwise rotating turbulent channel flow with heat transfer. Int. J. Num. Meth. Fluids, 53:1689–1706, 2007.

D. Lockerby, P. Carpenter, and C. Davies. Control of sublayer streaks using microjet actuators. AIAA Journal, 43:1878–1886, 2005.

A. Lozano-Duran and J. Jimenez. Effect of the computational domain on direct numerical simulations of turbulent channels up to $Re_\tau = 4200$. Phys. Fluids, 26:1–7, 2014.

J. Lumley. Toward a turbulent constitutive relation. J. Fluid Mech., 41:413–434, 1970.

A. Mishra and S. Girimaji. Intercomponent energy transfer in incompressible homogeneous turbulence: multi-point physics and amenability to one-point closures. J. Fluid Mech., 731:639–681, 2013.

Y. Miyake and T. Kajishima. Numerical simulation of the effects of Coriolis force on the structure of turbulence. Global effects. Bull. JSME, 29:3341–3346, 1986.

P. Moin and R. Moser. Characteristic-eddy decomposition of turbulence in a channel. J. Fluid Mech., 200:471–509, 1989.

N. Mole and E. D. Clarke. Relationships Between Higher Moments of Concentration and of Dose in Turbulent Dispersion. Bound. Layer Meteor., 73:35–52, 1995.

R. Moser, J. Kim, and N. Mansour. Direct numerical simulation of turbulent channel flow up to $Re\tau = 590$. Phys. Fluids, 11:943–945, 1999.

Y. Murakami, L. Shtilman, and E. Levich. Reducing turbulence by phase juggling. Phys. Fluids A, 4:1776–1781, 1992.

R. Reichert, F. Hatay, S. Biringen, and A. Huser. Proper orthogonal decomposition applied to turbulent flow in a square duct. Phys. Fluids, 6:3086–3092, 1994.

B. P. Reif, P. Durbin, and A. Ooi. Modeling rotational effects in eddy-viscosity closure. Int. J. Heat Fluid Flow, 20:563–573, 1999.

W. Reynolds. Computation of turbulent flows. Ann. Rev. Fluid Mech., 8:183–208, 1976.

D. Rizzetta and M. Visbal. Numerical study of active flow control for a transitional highly loaded low-pressure turbine. J. Fluids Engineering, 128:956–967, 2006.

T. Rung and F. Thiele. On the realizability of nonlinear stress-strain relationships for Reynolds stress closures. Flow. Turbulence and Combustion, 60:333–359, 1999.

W. Schoppa and F. Hussein. Coherent structure generation in near-wall turbulence. J. Fluid Mech., 453:57–108, 2002.

U. Schumann. Realizability of Reynolds-stress turbulence models. Phys. Fluids, 20:721–725, 1977.

L. Sirovich, K. Ball, and L. Keefe. Plane waves and structures in turbulent channel flow. Phys. Fluids A, 2:2217–2226, 1990.

L. Sirovich, K. Ball, and R. Handler. Propagating Structures in Wall-Bounded Turbulent Flows. Theoret. Comput. Fluid Dynamics, 2:307–317, 1991.

C. Smith and S. Metzler. The characteristics of low-speed streaks in the near wall region of a turbulent boundary layer. J. Fluid Mech., 129:27–54, 1983.

C. Speziale and T. Gatski. On explicit algebraic stress models for complex turbulent flows. J. Fluid Mech., 254:59–78, 1993.

C. Speziale, S. Sarkar, and T. Gatski. Modeling the pressure-strain correlation of turbulence: an invariant dynamical system approach. J. Fluid Mech., 227:245–272, 1991.

F. Tampieri, A. Maurizi, and S. Alberghi. Lagrangian models of turbulent dispersion in the atmospheric boundary layer. In G. Solari, L. C. Pagnini, , and G. Piccardo, editors, Ingegneria del Vento in Italia 2000, pages 37–50. S.G.E., 2000.

S. B. Waggy. Turbulent Transport in the Atmospheric Boundary Layer with Application to Wind Farm Dynamics. PhD thesis, University of Colorado, Boulder, 2012.

S. B. Waggy, S. Marlatt, and S. Biringen. Direct Numerical Simulation of the Turbulent Ekman Layer: Instantaneous Flow Structures. J. of Thermophysics and Heat Transfer, 25:309–318, 2011.

S. B. Waggy, S. Biringen, and P. P. Sullivan. Direct numerical simulation of top-down and bottom-up diffusion in the convective boundary layer. J. Fluid Mech., 724:581–606, 2013.

S. B. Waggy, A. Kucala, and S. Biringen. Parallel implementation of a Navier-Stokes solver: Turbulent Ekman layer direct simulation. Int. J. Comp. Methods, 11:443–460, 2014.

S. B. Waggy, S. Biringen, and A. Kucala. Wake effects on turbulent transport in the convective boundary layer. Geophysical and Astrophysical Fluid Dynamics, 109:465–479, 2015.

J. Wallace, R. Brodkey, and H. Ecklemann. Pattern-recognized structures in bounded turbulent flows. J. Fluid Mech., 83:673–693, 1977.

S. Xu, D. Rempfer, and J. Lumley. Turbulence over a compliant surface: numerical simulation and analysis. J. Fluid Mech., 478:11–34, 2003.

B. Younis, B. Weigand, and A. Laqua. Prediction of turbulent heat transfer in rotating and nonrotating channels with wall suction and blowing. J. Heat Transfer, 134:1–9, 2012.

S. S. Zilitinkevich, V. M. Gryanik, V. N. Lykossov, and D. V. Mironov. Third-Order Transport and Nonlocal Turbulence Closures for Convective Boundary Layers. J. of Atm. Sci., 56:3463–3477, 1999.

Appendix A

Details of Coding Numerical Structure

A.1 Overview

This appendix section will discuss the numerical structure and details of the two main codes (spatial and periodic models for channel flow) used for thesis research. As there are extensive similarities between the two codes, code details will be given in generalities and specific differences between the codes will be addressed where they exist.

A.2 Overall Code Structure and Routines

The code is written in the Fortran language and hence the main code files possess the extension ".F" which corresponds with the FORTRAN 77 fixed format. For MATLAB users, there are two primary differences (and innumerable lesser ones) between the coding structure of the MATLAB and Fortran languages. Unlike MATLAB, Fortran requires that for each subroutine, all variables used within the subroutine must have their variable class (i.e. integer, double precision, real, etc.) declared before being used in the subroutine. Also, unlike MATLAB, Fortran subroutines do not separate input and output variables during the subroutine calls. Hence the order of the variable listings during the subroutine call and definition must be exactly the same.

The main file and routine of the code is named 'main.F'. This routine contains the main structure of the code and all major subroutines are called by the main program. The other major files of the code include 'initialize.F', 'comp_setup.F', 'analysis.F', 'change_grids.F', 'create_mats.F',

'explicit_terms.F', 'grid_stuff.F', 'phi_RHS.F' and 'update_velocity.F'. There may be numerous subroutines located within each of these major Fortran files and further details on these subroutines are discussed later on in this section. In addition, there are also the supplementary files 'makefile' and 'petsc_include.inc', as well as the infile program which is located in the subfolder 'include_files' within the main code directory. Within the designated destination folder, there needs to be two subfolders 'Analysis' and 'FieldSaves' for the output files to be placed.

It must be noted that contrary to the directional notation used in the main portion of the thesis, the code treats the spanwise and wall-normal directions as the y- and z-directions, respectively; hence the velocities in the spanwise and wall-normal directions are respectively v and w. The 'petsc_include.inc' file contains the commands to link to the necessary PETSc include files required for code parallelization as these numerical algorithms were programmed using the Portable, Extensible Toolkit for Scientific Computation (PETSc) libraries. These routines were specifically designed for solving large systems using massively parallel algorithms. PETSc also gives the user the option to specify tolerances, the choice of the linear solution procedure, and other computation parameters directly from the command line, which allows a level of versatility for quickly tuning simulations.

The 'makefile' program contains the commands necessary for code compilation. The program links the compilation to the appropriate PETSc library using the aforementioned PETSc include file and then compiles the main Fortran files of the code to produce an executable program which can be run either on a local machine or remote supercomputer. A flowchart for the code is provided in Fig. A.1 (Waggy, 2012). The shaded boxes indicate portions of the code where each individual process can work relatively independent. A white box indicates an action which has extensive interprocess communication. The lower half of the flowchart (below the dashed line) represents the time integration sequence. One complete cycle will advance the velocity and temperature from time step n to $n+1$.

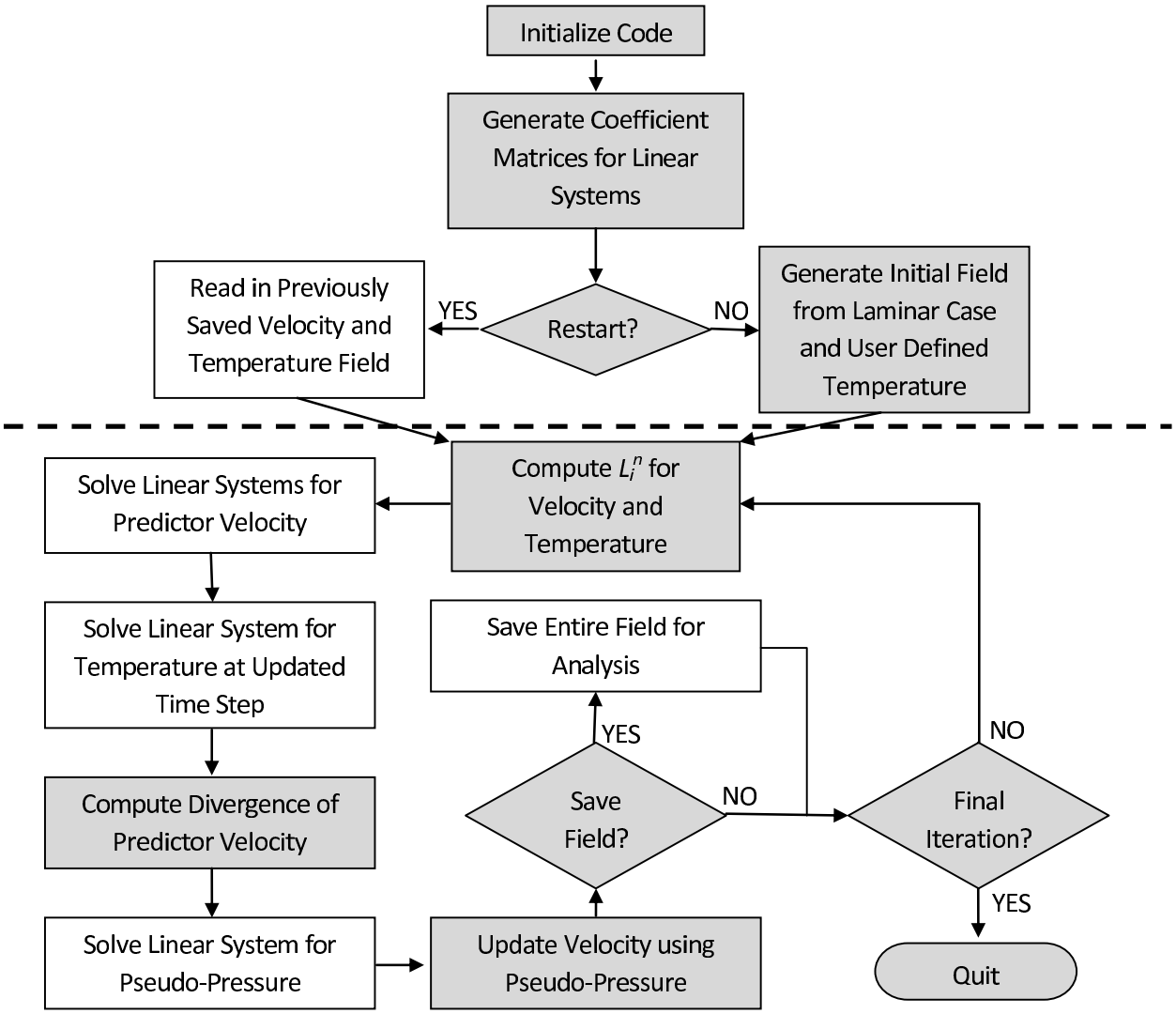

Figure A.1: Direct Numerical Simulation Flowchart: Shaded box, each process works independent; White box, global communication. Dashed line separates startup and time integration sequences (Waggy, 2012).

A.3 Initialization

The majority of the code parameters used for the direct numerical simulations are specified within an infile program located within the subfolder 'include_files' inside the main code directory. More than one infile program can be created within the subfolder; the desired infile program is specified within the 'initialize' subroutine which reads the data from the infile. Within the infile program, important computational details such as the simulation case name (casen) and path (caspath), starting (itstrt) and ending (itend) iterations, boundary conditions, relevant nondimensional quantities such as the Reynolds (Re), Rossby (Ro), Prandtl (Pr) and Richardson (Ri) numbers, as well as the computational box lengths in the streamwise (xlngth), spanwise (ylngth) and wall-normal (zmax) directions, are set by the user. A number of coding flags are also set in the infile program including 'restart' which can be set to true or false for a simulation which continues from a previous field save or a simulation which begins anew from a user-specified flow state, respectively. A full listing and corresponding descriptions of the parameters set in the infile program may be viewed in the 'initialize.F' subroutine in the main folder. The code is robust and offers a numerous array of optional variables relevant to testing linear stability theory and flow control. There is also support for variable grid spacing.

In the main program 'main.F', the resolution of the simulations is first specified for the streamwise (nx), spanwise (ny) and wall-normal (nz) directions. The main code then calls forth the initialized variables from the 'initialize.F' subroutine and file. Subsequently, the code generates the computational mesh and obtains the finite difference and Lagrangian interpolation coefficients from the 'gridgen' and 'coefcomp' subroutines located within the 'grid_stuff.F' file. The Lagrangian interpolation coefficients are used to interpolate flow variables from the cell-wall mesh (zw) to the cell-centered mesh (zc) in the wall-normal direction. The initialization routine of the code also allocates storage according to the resolution of the simulations. Flow variables are stored on all processors in a PETSc vector structure. In total, 25 vectors are declared (as outlined in Table A.1) leading to a large amount of storage due to the allocation of each right-hand-side (RHS)

Table A.1: Vector Storage (Waggy, 2012).

# of Vectors	Description
3	Full-step velocity
1	Temperature
3	Velocity on staggered mesh
1	Temperature on staggered mesh
1	Pseudo-pressure
6	L_i^n and L_i^{n-1} for velocity
2	L_θ^n and L_θ^{n-1} for temperature
3	RHS of velocity predictor equation
1	RHS of temperature equation
1	RHS of pseudo-pressure equation
3	Fractional velocities

individually (including staggered velocities).

The code initialization concludes by computing the user specified base velocity and temperature profiles within the 'get_base_profiles' subroutine in the 'comp_setup.F' file. The base profiles will also adhere to the user-specified boundary conditions for the velocity and temperature that were delineated in the infile program. However, these base profiles are not necessary if the case is a restarted simulation or there are available input files to be read. In the case of the spatial channel model, the flow profiles for the inflow planes are also specified here. For turbulent simulations using the spatial model, turbulent inflow planes are read using the available turbulence flags set within the code.

A.4 Generate Linear Operators

Linear solvers are required to advance the velocity in the predictor step and to compute the pseudo-pressure due to the use of the Crank-Nicolson scheme to integrate the vertical diffusion terms in the Navier-Stokes and energy equations. For the model equation

$$\frac{\partial u_i}{\partial t} \approx \frac{1}{\mathrm{Re}} \frac{\partial^2 u_i}{\partial x_3^2} \tag{A.1}$$

the Crank-Nicolson scheme can be written as

$$\frac{\hat{u}_i - u_i^n}{\Delta t} \approx \frac{1}{2\mathrm{Re}} \frac{\partial^2 \hat{u}_i}{\partial x_3^2} + \frac{1}{2\mathrm{Re}} \frac{\partial^2 u_i^n}{\partial x_3^2} + \mathcal{O}\left(\Delta t^2\right) \tag{A.2}$$

where $\mathcal{O}\left(\Delta t^2\right)$ implies that the solution is second-order accurate in time. The predicted velocity $\hat{u}_i$ is obtained from the solution of the linear system

$$\left(1 - \frac{\Delta t}{2\mathrm{Re}} \frac{\partial^2}{\partial x_3^2}\right) \hat{u}_i \approx u_i^n + \frac{\Delta t}{2} M_i^n \tag{A.3}$$

where

$$M_i^n = \frac{1}{\mathrm{Re}} \frac{\partial^2 u_i^n}{\partial x_3^2} \tag{A.4}$$

For the temperature equation, advancement of θ^n to θ^{n+1} is accomplished by substituting (Re) with $(\mathrm{Re\ Pr})$, u_i^n with θ^n, and $\hat{u}_i$ with θ^{n+1} in Eq. A.3 and A.4.

These velocity and temperature operators are computed within the 'make_uv_operator', 'make_w_operator' and 'make_T_operator' subroutines located within the 'create_mats.F' file. All solutions are obtained using the Krylov subspace methods of the PETSc library, specifically using the BCGS (Biconjugate gradient method) iterative algorithm to solve the linear system $Ax = b$. However, PETSc allows for multiple solution algorithms to be employed and also possesses options to set the relative tolerance error and a maximum iteration count for the iterative solver.

Solution of the Navier-Stokes and energy equations using the fractional step method results in $N^2 \times N^2$ systems of equations where $N = N_1 N_2 N_3$. A row in the coefficient matrix A for the system $Ax = b$ is locally owned by the processor which stores the flow variables for the row's corresponding gridpoint. The coefficient matrices for the linear systems are stored in parallel in the same manner as velocity and temperature vectors. For large systems, storage savings are obtained by preallocating non-zeros in the banded matrix. Boundary conditions, either Dirchlet or Neumann, are imposed directly through the A matrix. No 'folding-in' occurs as this operation would require allocating a smaller matrix to store coefficients.

A.5 Generate Initial Conditions

The initial conditions are created by either reading a previously saved velocity and temperature field or generating an initial condition (in the 'get_base_profiles' subroutine). These finalized initial conditions for velocity and temperature are respectively set in the 'set_init_velocity' and 'set_init_temp' subroutines located in the 'comp_setup.F' file. These conditions will also factor in user-prescribed perturbations such as random noise, which will eventually transition into turbulence through the growth of primary and secondary instabilities, or user-defined functions depicting an unstable solution of the linearized equations. Once the initial conditions have been properly generated, the main time integration loop for the Navier-Stokes solution is entered.

A.6 Compute L_i^n and Solve for Fractional Velocity and Temperature

The advection, horizontal diffusion, Coriolis, and mean pressure gradient terms in the Navier-Stokes equation are advanced using the fully explicit Adams-Bashforth method, which utilizes a two-level integration technique:

$$\frac{\hat{u}_i - u_i^n}{\Delta t} \approx \frac{3}{2} L_i^n - \frac{1}{2} L_i^{n-1} + \mathcal{O}\left(\Delta t^2\right) \tag{A.5}$$

where

$$L_i^n = -\frac{\partial u_i^n u_j^n}{\partial x_j} - \frac{1}{\mathrm{Ro}} u_j^n \varepsilon_{ji3} - \frac{\partial P}{\partial x_i} + \frac{1}{\mathrm{Re}} \left(\frac{\partial^2 u_i^n}{\partial x_1^2} + \frac{\partial^2 u_i^n}{\partial x_2^2} \right) \tag{A.6}$$

Combining Eq. A.3, A.4, A.5, and A.6 yields the following linear system of equations for the predictor velocity:

$$\left(1 - \frac{\Delta t}{2\mathrm{Re}} \frac{\partial^2}{\partial x_3^2}\right) \hat{u}_i = u_i^n + \Delta t \left(\frac{1}{2} M_i^n + \frac{3}{2} L_i^n - \frac{1}{2} L_i^{n-1} \right) \tag{A.7}$$

where L_i^n and M_i^n are given by Eq. A.6 and A.4 respectively. A similar time advancement is used for the conservation of energy equation

$$\left(1 - \frac{\Delta t}{2\mathrm{Re}\,\mathrm{Pr}} \frac{\partial^2}{\partial x_3^2}\right) \theta^{n+1} = \theta^n + \Delta t \left(\frac{1}{2} M_\theta^n + \frac{3}{2} L_\theta^n - \frac{1}{2} L_\theta^{n-1} \right) \tag{A.8}$$

where the explicit terms are given by

$$M_\theta^n = \frac{1}{\text{Re Pr}} \frac{\partial^2 \theta^n}{\partial x_3^2} \tag{A.9}$$

and

$$L_\theta^n = -\frac{\partial u_j^n \theta^n}{\partial x_j} + \frac{1}{\text{Re Pr}} \left(\frac{\partial^2 \theta^n}{\partial x_1^2} + \frac{\partial^2 \theta^n}{\partial x_2^2} \right) \tag{A.10}$$

The explicit terms for the velocity and temperature given by L_i^n and L_θ^n are first computed in the subroutine and file 'explicit_terms'. In order for the terms to be computed, a grid transform using fourth-order Lagrangian polynomials is performed within the subroutine and file 'change_grids' for each variable to allow products such as $u_1 u_3$ to be computed on either the vertical wall (z_w) or centered (z_c) grids. The RHS of the u_3 and θ linear system must be on the z_w mesh, and consequently, the advective terms are also defined on the z_w mesh by interpolating u_1 and u_2 onto z_w. On the other hand, u_1 and u_2 explicit terms require the RHS to be on the z_c mesh; hence variables u_3 and θ are interpolated from z_w to z_c.

The fractional velocity $\hat{u}_i$ and updated temperature θ^{n+1} are then solved using the linear operators previously defined and the newly computed RHS from the 'explicit_terms' subroutine. For this purpose, the 'KSPSolve' PETSc subroutine is employed.

A.7 Solve for Pseudo-Pressure / Updating Velocity

While the energy equation will have been integrated successfully using the above methods, a zero divergence for the velocity field needs to be enforced. The velocity field at the advanced time step $(n+1)$ is obtained by a pressure corrector step to the predicted velocity field.

$$\frac{u_i^{n+1} - \hat{u}_i}{\Delta t} = -\frac{\partial \phi}{\partial x_i} \tag{A.11}$$

The variable ϕ acts as a pseudopressure to account for small fluctuations in the turbulent field that are not accounted for when applying a mean pressure gradient. Taking the divergence of Eq. A.11 yields

$$\frac{1}{\Delta t} \left(\frac{\partial u_i^{n+1}}{\partial x_i} - \frac{\partial \hat{u}_i}{\partial x_i} \right) = -\frac{\partial^2 \phi}{\partial x_i \partial x_i}.$$

Continuity is enforced by stipulating that the advanced field be divergence free (i.e. $\partial u_i^{n+1}/\partial x_i = 0$). This results in the following linear system for ϕ based only on the fraction step velocity $\hat{u}_i$:

$$-\Delta t \frac{\partial^2 \phi}{\partial x_i \partial x_i} = \frac{\partial \hat{u}_i}{\partial x_i} \tag{A.12}$$

The updated velocity is then found using a rearranged form of Eq. A.11.

$$u_i^{n+1} = \hat{u}_i - \Delta t \frac{\partial \phi}{\partial x_i} \tag{A.13}$$

The divergence of the predictor velocity, $\partial \hat{u}_i/\partial x_i$, is a simple operation which requires updating boundary points of each processor in a similar manner as discussed for the explicit terms. Since the pseudo-pressure ϕ is defined on the z_c mesh, u_3 is interpolated from its original z_w grid onto z_c. Upon interpolating and updating boundary points for each processor, the RHS of Eq. A.12 is computed within the 'get_phi_rhs' subroutine and file. The solution of Eq. A.12 is obtained using the same algorithm used for the velocity and temperature equations. The linear operator for ϕ was obtained in the 'get_phi_operator' subroutine within the 'create_mats.F' file, which was computed prior to the time integration process. Neumann conditions ($\partial \phi/\partial x_3 = 0$) are imposed at both the lower and upper boundaries. This system is ill-conditioned since a null-space exists in the solution but PETSc provides an easily implemented function which removes the null-space by setting the mean of the pressure field to 0.

Once the pseudo-pressure is calculated, the velocity field at the advanced timestep, u_i^{n+1}, is computed via Eq. A.13 within the 'update_velocity' subroutine and file. In summary, advancing from the time level n to level $n+1$ requires solving 3 linear systems for the fractional velocity components ($\hat{u}$, $\hat{v}$, and $\hat{w}$), 1 linear system for the updated temperature (θ) field and 1 linear system for the pseudo pressure (ϕ).

A.8 Numerical Stability

When using numerical methods to solve a system of equations, there are generally two conditions for numerical stability which must be continuously fulfilled during the time integration

process. The first condition is that the velocity field must be divergence free ($\frac{\partial u_i}{\partial x_i} = 0$). The second condition is that the Courant number

$$CN_{max} = \frac{|u_i|_{max}\Delta t}{\Delta x_i} \tag{A.14}$$

must be below a certain threshold depending on the governing equations and the numerical scheme. For the current simulations, it was found that keeping $CN_{max} < 0.5$ was required to ensure stability. These computations are performed within the 'check_divergence' and 'get_courant' subroutines located in the 'analysis.F' file.

A.9 Field Saves

Field saves are conducted at a frequency defined by the user and consist of the full statistical fields ($nx \times ny \times nz + 1$) for the streamwise ($u$), spanwise ($v$), and wall-normal ($w$) velocity, temperature (t), pressure (p) and an accompanying data file (dat) for a given case name and iteration. The data file contains relevant information such as the iteration count, simulation time, grid resolution and nondimensional quantities (Reynolds number, Prandtl number, etc.). These computations are performed within the 'save_field' subroutine and file. If statistical turbulent averages are of interest, a field is typically saved every hundred or thousand iterations. If time varying analysis is to be completed, the frequency would increase to every few iterations.

The data files can become quite large and memory is an issue for high-resolution simulations. For example, a $256 \times 256 \times 129$ mesh requires approximately 320 MB per field save for the velocity, temperature, and pressure files. After saving the field, the code checks to determine if the last iteration has been reached. If so, all parallel vectors and matrices are deallocated and the computation concludes. If not, the code begins computing the explicit terms for the next time step.

A.10 Linear Stability Theory Testing

Both the periodic and spatial channel models offer extensive support for testing temporal and spatial linear stability theory, respectively. For the periodic model, the Reynolds number

and streamwise wavenumber (α) are specified to solve for a temporal frequency (ω). For the spatial model, the Reynolds number and frequency (ω) are specified to solve for a real streamwise wavenumber (α). Furthermore, both channel models can investigate three-dimensional stability theory through the additional specification of the spanwise wavenumber (β).

In addition to specifying the aforementioned quantities within the infile program, the two-dimensional (eig2Dfil) and three-dimensional (eig3Dfil) eigenfunction files must be specified along with the maximum amplitude of the two-dimensional (amp2d) and three-dimensional (amp3d) perturbations (assuming the maximum amplitude of the eigenfunctions in the corresponding files have been normalized to 1). The eigenfunction files should have the length of the wall-normal direction ($nz + 1$) and contain six columns for the real and imaginary component values for the streamwise (first and second columns), spanwise (third and fourth columns) and wall-normal (fifth and sixth columns) perturbation velocities, although only the real components are read by the code. The eigenfunctions are added to the flow variables first in the initialization process ('set_init_velocity') and then during the explicit terms ('explicit_terms') and velocity update ('update_velocity') computations.

A.11 Flow Control Options (Spatial Model)

The spatial channel model also possesses support for flow control, specifically regarding a control subsurface consisting of a phononic structure. The coding of the phononic subsurface unit cell was done by members of Prof. Mahmoud Hussein's research group at CU-Boulder and the code file was supplied as a '.cpp' extension file written in the $C++$ language. These structure code files are placed in the main code folder and called by the makefile program; hence switching between different versions of the structure code will require editing the name of the structure file in the makefile program.

In order to be read properly by the main code, the structure file requires linking to the location of the Template Numerical Toolkit (TNT) library. The structure code may also be edited to change the layers and composition of the unit cell. This is accomplished by editing the 'ratios'

variable to reflect the elemental composition of the unit cell (100 elements) and creating an equivalent number of node variables (first_nodes, second_nodes, etc.) to match the number of layers within the unit cell.

In the infile program, flow control is enacted by setting the 'wall2D', 'dbot' and 'FEM' flags to 'true', in which case the phononic subsurface is activated on the bottom channel wall. The material properties of the unit cell are set using the 'c1', 'c2', 'rho1' and 'rho2' variables; the length of the unit cell in meters is set using the 'unit_length' variable. The number of phononic subsurface slots and its resolution is set using the 'n_slot', 'n_pts_slotx' and 'n_pts_sloty' variables; the starting and ending locations of the slot (in terms of the grid points) is set using the 'stxv' and 'styv', and 'exv' and 'eyv' variables, respectively. It should be noted that turning on flow control will result in additional structure files ('FEM.') being created and saved in the FieldSaves subfolder.

The fluid-structure interaction portion of the code is located within the 'FSIcalc' subroutine in the 'FSI.F' file. In order to calculate the streamwise and wall-normal velocities at the fluid-structure interface, the code first calculates the force and displacement occurring at the interface using the dimensional wall pressure and mean velocity gradient. These force and displacement values are then passed into the structure code which outputs the corresponding velocities (u_FEM and w_FEM) at the interface. The dimensional wall pressure and mean velocity gradient are first computed within the 'get_pressure' and 'calc_grad' subroutines and files, respectively.

A.12 Buffer Region (Spatial Model)

The spatial channel model also includes a buffer region in order to prevent reflections at the outflow boundary by convecting the perturbations by the base flow out of the computational domain. The buffer domain technique sets the convective terms of the streamwise perturbation equations to zero using a coefficient function

$$c(x) = \frac{1}{2} tanh[s(L_h - x)] + \frac{1}{2} \tag{A.15}$$

where L_h is half the length of the buffer domain and s is a stretching parameter controlling the gradient of the coefficient function. s corresponds to the variable 'cbf' located in the infile program and the 'xbuff' variable sets the start of the buffer domain in the streamwise direction. The buffer region is computed in the 'get_buffer' subroutine located in the 'grid_stuff' file. The coefficient function is also written to a file named 'buff.' in the Analysis subfolder. It is ideal for the coefficient to fall gradually (not in a vertical or steep manner) from one to zero once the buffer region is encountered.